



Effect of Geometry on Packing and Parking of Colloidal Spheres

Citation

Tanjeem, Nabila. 2020. Effect of Geometry on Packing and Parking of Colloidal Spheres. Doctoral dissertation, Harvard University, Graduate School of Arts & Sciences.

Permanent link

<https://nrs.harvard.edu/URN-3:HUL.INSTREPOS:37365124>

Terms of Use

This article was downloaded from Harvard University's DASH repository, and is made available under the terms and conditions applicable to Other Posted Material, as set forth at <http://nrs.harvard.edu/urn-3:HUL.InstRepos:dash.current.terms-of-use#LAA>

Share Your Story

The Harvard community has made this article openly available.
Please share how this access benefits you. [Submit a story](#).

[Accessibility](#)

Effect of Geometry on Packing and Parking of Colloidal Spheres

A dissertation presented

by

Nabila Tanjeem

to

Harvard John A. Paulson School of Engineering and Applied Sciences

in partial fulfillment of the requirements

for the Degree of

Doctor of Philosophy

in the subject of

Applied Physics

Harvard University

Cambridge, Massachusetts

December 2019

©2019 - Nabila Tanjeem

All rights reserved.

Effect of Geometry on Packing and Parking of Colloidal Spheres

Abstract

Colloidal microspheres, sometimes referred to as ‘model atoms,’ are commonly used to elucidate self-assembly mechanisms of different materials. One of the important yet relatively unexplored parameters that affects self-assembly is the geometry of the substrate on which self-assembly takes place. In this thesis, I examine how substrate geometry affects self-assembled structures and self-assembly dynamics and demonstrate how this knowledge can be used to design precisely controlled nanostructures.

Colloidal self-assembly can be designed in various ways – weak attractive interactions between colloidal microspheres give rise to colloidal crystallization, whereas strong attractive interactions result in random sequential adsorption. I show a number of methods to tune colloidal interactions to achieve crystallization (packing) and random sequential adsorption (parking) on the surface of a cylinder. A cylinder has a zero Gaussian curvature, but a non-zero mean curvature and a finite circumference. Using experiment and theory, we demonstrate that the finite circumference and mean curvature of a cylindrical substrate affect both crystallization and random parking of colloidal spheres.

A crystal that completely wraps around a cylindrical surface must contend with closure. We find that the closure constraint gives rise to unique structural features, such as chirality, line-slip defects, and kinked line-slip defects with fractional vacancies. We show that the morphology of these structures arises from the crystallization

dynamics. When colloidal spheres randomly adsorb on a cylindrical substrate, we find that the surface coverage fraction becomes a function of the curvature of the cylinder and deviates significantly from the surface coverage fraction on a flat substrate. Both of these findings provide a pathway to realize self-assembly mechanisms of natural and artificial tubular structures.

Finally, we show that sphere packing on a spherical substrate can be used to synthesize patchy colloidal structures. We turn the patchy structures into octahedral plasmonic nanoclusters using a multi-step synthesis approach. We find that these nanoclusters have identical optical properties, which indicates robust and precise control over their geometry. This result shows that what we learn from colloidal self-assembly and geometry can be applied to design materials with complex structures and functionality.

Contents

Title Page	i
Abstract	iii
Table of Contents	v
List of Figures	vii
Prior Publications	xvii
Acknowledgments	xviii
1 Introduction	1
1.1 Self-assembly of colloidal spheres	2
1.2 Self-assembly on a cylindrical substrate	7
1.3 Overview of thesis	8
2 Crystal morphology and growth dynamics on a cylinder	11
2.1 Introduction	11
2.2 Crystal formation on a cylinder	13
2.3 Chiral crystals and chiral defects	15
2.4 Line-slip defects with kinks	18
2.5 Mechanism of kink formation	22
2.6 Effect of crystal growth anisotropy on morphology	23
2.7 Conclusion and outlook	27
2.8 Materials and methods	30
2.9 Calculation of equilibrium length of line-slip defect	35
2.10 Supplementary results	43
3 Structure of colloidal polycrystals on a cylinder	50
3.1 Introduction	50
3.2 Methods	51
3.3 Results	54
3.4 Discussions and outlook	57

4	Random parking of colloidal spheres on a cylinder	61
4.1	Introduction	61
4.2	Theory	64
4.3	Experiments	68
4.4	Discussions	71
4.5	Conclusion	76
4.6	Materials and methods	77
5	Polyhedral plasmonic nanoclusters through multi-step colloidal chemistry	81
5.1	Introduction	81
5.2	Multi-step synthesis of plasmonic nanoclusters	82
5.3	Characterization of plasmonic nanoclusters	85
5.4	Conclusion	93
5.5	Materials and methods	95
6	Conclusion and outlook	109
6.1	Future directions for self-assembly on a cylinder	110
6.2	Self-assembly in different geometry	113
6.3	Final remarks	116
	Bibliography	117

List of Figures

1.1	Mechanism of depletion interaction in a binary mixture of large spheres (radius R_L) and small spheres (radius R_S). The light-blue region around each large sphere shows the ‘depletion zone’ where the center of the small spheres cannot enter. The dark-blue region in between the large spheres is the overlap volume of the depletion zones.	3
1.2	(a) A positively charged surface. Some negative counter-ions accumulate very close to the surface, creating the ‘Stern layer’. Other negative counter-ions diffuse nearby, forming the ‘diffuse layer’. Both of these layers determine the shape of the interaction potential which is a function of distance r from the charged surface. Away from the surface, the charge distribution is uniform and hence the potential is zero. (b) When two oppositely charged bodies come close to one another, their double layers as well as the interaction potential curves overlap, resulting in an attractive force.	4
1.3	(a) Diagram of depletion interaction between colloidal spheres and a flat surface, showing the overlap in excluded volume (blue). (b) Image taken with a confocal microscope showing colloidal spheres (average diameter 710 nm) packing on a flat glass surface. The depth of the interaction potential is small enough that the particles can find their maximum packing configuration. (c) DNA hybridization between colloidal spheres and a flat surface coated with DNA strands with complementary sequences. (d) Image taken with a bright-field microscope showing colloidal spheres (average diameter 1.3 μm) park on a flat glass surface. The depth of the interaction potential is large, as a result, particles stick irreversibly to the glass surface.	6

1.4	Close packed configurations of hard spheres inside a cylinder, examined by Pickett and coworkers. Different configurations are found as the cylinder-to-sphere diameter ratio D varies in the range of $1 < D \sim 2.155$. Six different regions are defined as denoted by I-VI; the corresponding structures in those regions are indicated by the black arrows. Figure reproduced from reference [1].	8
1.5	Phase diagram of chirality (or helicity) as a function of size ratio calculated by Wood, Santangelo, and Dinsmore [2]. When the interaction range between the spheres is short, defect structures (orange dots) are preferred over asymmetric crystal structures (blue dots). Figure reproduced from reference [2].	9
2.1	(a) Scanning electron microscopy image of a tapered optical fiber. Both thick and thin parts belong to the same fiber. The original fiber diameter is $125\text{ }\mu\text{m}$, and the smallest diameter in the tapered part is about 200 nm . (b) Setup for depletion interaction. Colloidal particles have an average diameter $D = 710\text{ nm}$. Sodium dodecyl sulfate (SDS) forms micelles with an effective diameter of 30 nm [3, 4]. These micelles induce a short-ranged depletion force between the particles. We examine crystallization where the diameter d of the cylinder is between $1.5\text{ }\mu\text{m}$ and $5.5\text{ }\mu\text{m}$. (c) Projection of a stack of confocal microscope images of colloidal crystals formed on the surface of a cylinder.	13
2.2	(a) Confocal microscope images of colloidal crystals formed on a flat 2D surface, where there is no closure constraint. Each red dotted box denotes one single crystalline grain. (b) Confocal microscope images of crystals assembled on cylinders for different cylinder-to-sphere diameter ratios $r = d/D = 4.43$ (top) and 2.46 (bottom). Inside each red dotted box, we show the front and back of a single crystal wrapped around the cylinder. The single crystals are identified by the consistent chiral angle found at both sides of the cylinder.	14
2.3	(a) Formation of a crystal without any defects requires that the cylinder circumference C be an integer linear combination of the lattice vectors \mathbf{a}_1 and \mathbf{a}_2 : $C_{m,n} = m\mathbf{a}_1 + n\mathbf{a}_2$. The chiral angle ϕ of the crystal depends on the integers m and n . For example, configurations $(9,0)$ and $(5,5)$ are achiral, whereas configuration $(7,3)$ is chiral. (b) Confocal microscope images of crystals with different chirality observed in experiment. The four crystals are observed at different parts of the same tapered cylinder. We measure the chiral angle ϕ of each crystal from the images. . . .	16

2.4	Images of line-slip defects with different chirality, along with the bond network extracted from the images. The chirality of a line-slip defect is defined by the angle θ that the slip line forms with the circumferential axis of the cylinder. The blue circles show the positions of particles that form the line-slip defect, and the red circles show the other particles in the crystal. All scale bars are $2\mu\text{m}$	17
2.5	Confocal images and bond networks of three kinked line-slip defects with different number of fractional vacancies. n_1 is the total length along the line-slip defect in units of particle center-to-center distance along the lattice direction \mathbf{v}_1 . n_2 is the length along a second lattice direction \mathbf{v}_2 . Along this line, none of the particles are in contact with another particle across the line-slip; they are instead in contact with the fractional vacancies. We define the line-slip length $l = n_1$ and the path length, including the fractional vacancies, as $L = n_1 + n_2$	19
2.6	A model used to calculate the equilibrium length l_{eq} of a line slip. The line slip is where the black and blue halves of the crystals meet. The length of the red solid line along the line slip is equal to n_1 , and the length of the red dotted line is equal to n_2 . In the limiting case of a straight line-slip defect without any kinks, $n_2 = 0$ and $L = n_1 = l$. Starting from this ground state, we calculate all the possible configurations of the defect using lattice vectors \mathbf{v}_1 , \mathbf{v}_2 , and \mathbf{v}_3 , assuming the circumference of the cylinder is larger than L	20
2.7	Plot of l as a function of L for ground states, equilibrium, and experiment. In the ground state, $L = l$. The equilibrium length l_{eq} represented by the red straight line is calculated from the model assuming $E_b = 4k_B T$. To find l from experiment, we measure n_1 and n_2 from images of 116 crystals and calculate $l = n_1$ and $L = n_1 + n_2$. The black points represent each crystal and the blue boxes show the distribution of l for each L	21
2.8	Confocal images showing the formation of a kinked line-slip defect. At $t = 0$, a line-slip defect begins to form when the crystal wraps around the cylinder. At $t = 1.76$ min, another line slip starts forming in a parallel line, leaving fractional vacancies between the two. The line slips continue to grow until $t = 10$ min, after which we observe fluctuations in the kinked shape but not in the number of fractional vacancies.	22

-
- 2.9 Images from Brownian dynamics simulations of crystal growth. In each image the crystal is shown cut and unwrapped, such that the entire circumference of the cylinder is visible. All four crystals shown here form on a cylinder with the same circumference. The line-slip defect of crystal 1 (identified by the yellow particles) has an angle of $\theta = 78.69^\circ$ with respect to the circumferential axis of the cylinder. As the crystal grows, the line-slip sometimes forms a kink (frames 3 and 5 from the left) but quickly rearranges into a straight line slip (frame 6). Crystal 2 has a line-slip defect with a smaller $\theta = 30.26^\circ$. In this case, the line slip fails to follow the crystal growth and traps a number of fractional vacancies. Crystal 2 has a larger value of δ than crystal 1 (0.67 compared to 0). Crystal 3 and crystal 4 both have line-slip angles of about $\theta = 55^\circ$, and their values of δ are also in between those for crystals 1 and 2 ($\delta = 0.11$ for crystal 3 and $\delta = 0.53$ for crystal 4). 24
- 2.10 (a) Contour plot showing probability distribution (kernel density estimate) of kinked line-slip defects as a function of δ and θ for 79 simulated crystals with fixed r . (b) Same type of plot as (a), but showing data from 116 crystals found in experiment with varying r . The plots show that the number of fractional vacancies varies with the line-slip angle in the same way, though the correlation coefficient in the experiment (-0.49) is smaller than that of simulation (-0.77), likely because the experimental data are not taken at a single size ratio. 25
- 2.11 (a) (b) Growth model of line-slip defects in two crystals with same chiral angle ϕ but different line-slip angles θ . At each time, new particles (particles with red circular borders) are added to the faces of the crystal grain. Before the crystal wraps around the cylinder (steps 1, 2, and 3), particles are equally likely to attach to any of the three faces of the crystal, resulting in isotropic growth. Once the crystal wraps around, particles can attach only to the two faces that are not aligned with the cylinder axis (step 4). In a, both of these faces make approximately the same angle with the cylinder axis. Thus, the growth rates should be approximately the same, and the line slip (yellow particles) can grow straight. In b, the crystal has wrapped around, occluding the vertical face. As a result, the growth rates on the two faces must differ, and therefore the line slip tends to incorporate more fractional vacancies. 26
- 2.12 (a) A line-slip defect in a crystal found in simulation with $\phi = 41.5^\circ$ and $\theta = 80.5^\circ$. (b) A line-slip defect in a crystal found in simulation with $\phi = 44.3^\circ$ and $\theta = 45^\circ$ 27

2.13	(a) Length of three different faces of crystal over time for the crystal in Fig. 2.12a. Face 2, which is aligned with the cylinder axis as well as the line-slip defect grows without competition from the two other faces. As a result, the line-slip defect is almost straight with negligible fractional vacancies. (b) Same plot as in a, but for the crystal in Fig. 2.12b. Here, face 3 is aligned with the line-slip defect but less aligned with the cylinder axis. It competes with face 2, which is more aligned with the cylinder axis. As a result, the line-slip defect incorporates many fractional vacancies.	28
2.14	Cylinder diameter as a function of distance from the cylinder tip. The black dotted line indicates the diameter range used in experiment.	30
2.15	Sample chamber setup on a microscope stage. Only the colloidal spheres (diameter 710 nm) are fluorescently dyed (Firefli Fluorescent Red 542/612 nm). We use a confocal microscope to observe them forming crystals on the cylinder.	33
2.16	(a) Ground state configuration of a line-slip defect with length $L = 10$. The starting point of the defect is \mathbf{v}_i and the ending point is \mathbf{v}_f . (b) One excited state with the same \mathbf{v}_i and \mathbf{v}_f as in (a). (c) Another excited state with the same \mathbf{v}_i and \mathbf{v}_f as in (a), (b). All of the excited states can be calculated from the possible configurations of n_1 , n_2 , and n_3 . (d), (e), (f) Excited states of the line-slip defect that ends at a different \mathbf{v}_f . The values for n_1 , n_2 , and n_3 are different from those in (a), (b), and (c).	36
2.17	(a) One excited state configuration for $\mathbf{v}_f = 9\mathbf{v}_1 + \mathbf{v}_2$. (b) The same excited state configuration for $\mathbf{v}_f = 9\mathbf{v}_1 - \mathbf{v}_2$. This is a mirror image of the one in (a). Since the number of configurations in this mirror setup is exactly the same, we calculate only the number of configurations for $\mathbf{v}_f = 9\mathbf{v}_1 + \mathbf{v}_2$ and multiply this by 2. (c) Image of the configuration for the first $\mathbf{v}_f = 10\mathbf{v}_1$. This is also the ground state. (d) Image of the configuration for the final $\mathbf{v}_f = 10\mathbf{v}_2$. In this configuration, the line-slip is full of fractional vacancies. This is the maximum \mathbf{v}_f that is relevant. If the cylinder circumference (indicated by the dotted black parallel lines) is larger than the line-slip length L , we must consider all values of \mathbf{v}_f starting from the one in (c) and ending in the one in (d).	39
2.18	Equilibrium line-slip length l_{eq} as a function of total line-slip length L for different values of the potential well depth.	42
2.19	A line-slip like defect found in a small crystalline grain on a flat 2D surface. It relaxes in a short time because the grain is free to translate and rotate.	43
2.20	Closure of a crystal without any line-slip defect. The grain closes within a few minutes and does not get kinetically trapped.	44

2.21	Dynamics of a kinked line-slip defect with one fractional vacancy. (a) Confocal microscope image of the kinked line-slip defect when the fractional vacancy is at position 0. (b) Confocal microscope image of the kinked line-slip defect when the fractional vacancy is at position 1. (c) Position of the kink identified from the confocal images over about 150 min. The kink mostly moves back and forth between positions 0 and 1, but it also jumps to positions 2, 4, and 5 later. However, the number of bonds stays same the throughout.	45
2.22	Dynamics of a kinked line-slip defect with many fractional vacancies. (a) Confocal microscope image of the kinked line-slip defect at different points in time. (b) Line-slip length l for the defect as a function of time. l fluctuates, but does not decrease significantly or reach its ground state value.	46
2.23	(a) Confocal microscope image of a kinked line-slip defect. Particles are color-coded based on the number of bonds. The red particles make bonds with 4 nearest neighbors and the black particles make bonds with 5 nearest neighbors. (b) Displacement of each red and each black particle in (a) as a function of time.	48
2.24	(a) A line-slip defect with a single fractional vacancy. (b) Over time, the vacancy from (a) moves out of the crystal boundary. (c) A line-slip defect with a full vacancy on the slip-line. (d) Over time, part of the vacancy moves out of the crystal boundary creating a fractional vacancy in a kinked line-slip defect.	49
3.1	(a) Confocal image of polycrystals on a cylinder. The red dotted lines show the position of grain boundaries between each single crystal wrapped around the cylinder. (b) Model of a cylindrical crystal. . .	52
3.2	(a) Confocal image of polycrystals on a flat 2D surface. To calculate the average grain length, we draw 9 straight lines at different angles throughout the image. (b) Line 1 and its surroundings. We find four grain boundaries shown by the red dotted lines. Therefore, $N_{gb} = 4$. We repeat this procedure to find values of N_{gb} for all nine lines in (a) . . .	54
3.3	Grain length L measured for various cylinder-to-sphere size ratios D_C . Each blue point corresponds to one crystalline grain on a cylinder. The blue solid line represents a linear fit while the shaded region around it shows the span of one standard deviation. The red horizontal line shows L_{av} on a flat 2D surface.	55
3.4	Grain area S for different cylinder-to-sphere size ratios D_C . The blue solid line represents a linear fit while the shaded region around it shows the span of one standard deviation.	56

3.5	(a) Grain anisotropy A measured for various cylinder-to-sphere size ratios D_C . The blue solid line represents a linear fit while the shaded region around it shows the span of one standard deviation. The red dotted horizontal line corresponds to a grain of isotropic shape, with its length equal to its circumference, such that $L = \pi D_C$ and $A = 1.0$.	57
3.6	Confocal images of crystals growing on a cylinder, as viewed from the front and back sides of the cylinder. Grains 1, 3, 5, and 7 form about 20 minutes earlier than grains 2, 4, and 6. The chiral angle θ of the seven grains are $\theta_1 = 40.91^\circ$, $\theta_2 = 36.87^\circ$, $\theta_3 = 35.32^\circ$, $\theta_4 = 39.69^\circ$, $\theta_5 = 4.93^\circ$, $\theta_6 = 7.35^\circ$, and $\theta_7 = 33.69^\circ$.	59
4.1	Spheres-on-cylinder morphologies in (a) dental plaque “corncob” formations [5], (b) sea grapes, (c) peppercorn drupes, and (d) winterberries.	63
4.2	(a) Cartoon of spheres adsorbed on a wire. A sectioning plane indicated through the shade change is shown below, with r indicating the cylinder radius and R the particle radius, ρ indicating the radius of a particular cross-section through the particle, and $\Delta\phi$ indicating the angle subtended by the particle cross-section at the center of the wire. (b) Two-dimensional representation in the $\phi - z$ plane of spheres of radius $R = 1$ adsorbing on a cylinder of radius $r = 1$ and length $L = 20$.	65
4.3	Longtime coverage $\rho_\infty^{(3D)}$ versus scaled wire size $\tilde{r} = r/R$ (Eq. (4.3)) from effective 2D simulations of spheres parking on a cylinder. The dashed black line indicates the longtime coverage for random sequential adsorption of spheres on a plane, $\lim_{\tilde{r} \rightarrow \infty} \rho_\infty^{(3D)} = (2/3) \lim_{\tilde{r} \rightarrow \infty} \rho_\infty^{(2D)} \approx 0.3647$, where $\lim_{\tilde{r} \rightarrow \infty} \rho_\infty^{(2D)} \approx 0.5471$ is the asymptotic coverage of discs on a plane [6].	66
4.4	(a) Schematic (left) and optical micrograph (right) of negatively charged particles binding irreversibly to a positively charged nanowire (b) Schematic (left) and optical micrograph (right) of DNA-coated particles binding to nanowire coated with complementary DNA strands.	68
4.5	(a) Linear particle density λ versus scaled wire size $\tilde{r} = r/R$ and (b) 3D asymptotic density $\rho_\infty^{(3D)}$ versus scaled wire size $\tilde{r} = r/R$ from simulations (black crosses), and experiments using either electrostatic attraction (red squares, yellow circles, and green triangles show results from three different experiment samples) or DNA hybridization (blue diamonds). The dashed black line indicates, as in Fig. 4.3, the longtime coverage for random sequential adsorption of spheres on a plane, $\lim_{\tilde{r} \rightarrow \infty} \rho_\infty^{(3D)} \approx 0.3647$. Shaded regions indicate an interval of two standard deviations from the mean simulation results. In order to reproduce the experimental uncertainty associated with small particles numbers, simulations were performed on short wire segments that accommodate around 50 particles.	69

4.6	Longtime (asymptotic) coverage $\rho_{\infty}^{(2D)}$ versus scaled wire size $\tilde{r} = r/R$ (Eq. (4.3)) from simulation. The dashed black line at 0.5471 indicates the longtime coverage for the random adsorption of discs on the plane (that is, in the limit $\tilde{r} \rightarrow \infty$).	72
4.7	Two-dimensional representation in the $\phi - z$ plane of spheres of radius $R = 20$ adsorbing on a cylinder of radius $r = 1$ and length $L = 1000$. To compute the angular density-density correlation function, we fix a particle (shown in red), consider a strip of width Δy along a direction θ , and count the number of particles whose centers are contained inside this strip. Repeating this procedure for all particles and then for different angles θ yields the plot in Fig. 4.8.	73
4.8	Plot of the angular density-density correlation $\langle n(\vec{r}) n(\vec{r}', \theta) \rangle$ as a function of angle θ	74
4.9	Varying $\tilde{r} = r/R$ changes the maximal density direction θ_{max} (that is, the angle for which $\langle n(\vec{r}) n(\vec{r}', \theta) \rangle$ is maximum) as $\tan \theta_{max} \approx 3\tilde{r}$	75
5.1	Our synthesis scheme for plasmonic clusters consists of seven steps: (1) We perform seeded-growth emulsion polymerization of styrene on spherical silica particles with a diameter of 86 nm. (2) We then overgrow the silica seed and (3) dissolve polystyrene, which results in structures with six concave dimples. (4) We aminate the residual polystyrene at the bottom of the dimples to complete the template. (5) We lock carboxylated silica nanospheres with a diameter of 137 nm onto the aminated dimples. (6) We convert the carboxylate groups on the silica satellites into amine groups using ethylene diamine. (7) We grow a thin gold shell on top of the spheres by the site-specific adsorption of gold nuclei and subsequent regrowth.	83
5.2	(a) TEM images of silica/gold clusters with varying gold shell thicknesses, obtained with different amounts of gold precursor: a) 5 mL; b) 10 mL; c) 20 mL; d) 25 mL and e) 35 mL. (b) Nine different clusters for the regrowth condition of 25 mL gold precursor.	86
5.3	Single-particle spectroscopy setup. (a) Setup for measuring the spectrum of light scattered from individual nanoclusters. The light source is an unpolarized halogen lamp illuminating the sample at an incidence angle of 65° (25° with respect to the horizontal axis). An objective ($50\times$, $NA = 0.5$) is placed on top of the grid to collect the scattered light. An adjustable aperture is placed in the optical path of the spectrometer to collect light from only a narrow area (a circle with a diameter of about $1\mu\text{m}$) surrounding the cluster. To make sure that clusters are well separated, we dilute the experimental sample. (b) TEM image of a target cluster (inside red circle) near marker “P” on TEM grid. (c) The same target cluster imaged with the dark-field microscope.	87

5.4	Measured spectra of nine individual octahedral clusters.	88
5.5	Diagram of experimental geometry. Our model accounts for the incidence angle, collection angle, and substrate geometry used in the experiments. To mimic an unpolarized light source, we add the scattered intensity from two orthogonal polarizations.	89
5.6	Cross-sectional view of the geometry of the octahedral cluster simulated in FDTD, showing the gold shell thickness (23 nm) and separation between the gold layers on the satellites (1.98 nm), both of which were estimated from TEM images of clusters before and after the gold plating step.	90
5.7	Finite-difference time-domain (FDTD) simulations reproduce the locations of the measured peaks. Charge density maps near 700 nm, 808.7 nm, and 892.5 nm show different resonant modes inside the cluster at those wavelengths. As we increase the separation distance between particles, all the peaks shift to shorter wavelengths.	91
5.8	STEM-EDX elemental mapping of the gold clusters: bright field TEM image (top left) and silicon, oxygen, gold and superimposed EDX maps evidencing the core-shell morphology of the six satellites.	103
5.9	(a) 3D view of the simulation setup for p -polarized light. (b) Sideview of the simulation setup for p -polarized light. (c) 3D view of the simulation setup for s -polarized light. (d) Sideview of the simulation setup for s -polarized light.	105
5.10	Map of refractive index in a cross-sectional plane of an octahedral nanocluster modeled in simulation.	106
5.11	Far-field radiation pattern of a modeled nanocluster at three different wavelengths. The incident light polarization is aligned with the x -axis. The patterns at 892.5 nm represent electric dipolar radiation and the patterns at 700 nm represent electric quadrupolar radiation, in both XY and XZ planes. At the wavelength of 808.7 nm, the quadrupolar mode shows up in the XY plane (shown by the black arrows).	107
5.12	Scattering spectra for clusters with different gaps. The total intensity is the sum of the intensity of s -polarized and p -polarized light. We find one dominant peak for each of the polarizations. For a 1.98 nm gap geometry, the peak for s -polarized light is around 770 nm and the peak for p -polarized light is around 892.5 nm. As the gap increases from 1.98 nm to 4.98 nm, both of the peaks for s -polarized and p -polarized light blue-shift. As a result, the peaks in the total scattered light spectra (shown by green plot) also blue-shift.	108

6.1	(a) Line-slip defect with small gap at the slip and large angle at the kink. The large angle enables particles at the kink to hop more often. (b) Line-slip defect with large gap at the slip line and small angle at the kink. The small angle does not enable particles at the kink to hop often.	111
6.2	(a) Crystal with a kinked line-slip defect at room temperature. (b) At high temperature (60°C), the crystal starts to sublime (bottom right corner); half of the defect disappears as the crystal starts to sublime.	112
6.3	(a) Image of a cone fabricated by pulling a glass capillary tube. The red line shows a scale bar with a length of 10 μm . (b) Confocal micrograph of colloidal particles self-assemble on the surface of a cone through depletion interactions.	114
6.4	Confocal microscope images of a colloidal crystal made of particles with two different sizes, 700 nm (green) and 800 nm (red). The top panel shows variation in structure at their number ratios (a) 90:1 (b) 9:1, and (c) 1:1. The bottom panel shows the same images in black and white. Crystals in (e) have smaller grains and more grain boundaries. They also have more second layers (the bright white spots on top of the crystals) compared to the crystals in (d). In contrast, the crystals in (f) have no long-range order and, as a result, do not form a second layer.	115

Prior Publications

This thesis is partly based on the following publication:

- Chapter 4: Edvin Memet, **Nabila Tanjeem**, Charlie Greboval, Vinothan N. Manoharan, L Mahadevan, *Europhysics Letters* **127** (3), 38004 (2019).

Other publications relating in part to work discussed in this thesis are in preparation.

Acknowledgments

To do a successful experiment, a number of parameters (samples, equipments, timing etc.) have to work well – I learned this hard truth after spending years of my training as an experimentalist. In a similar way, I realize that to complete a PhD thesis, quite a few parameters (advisors, mentors, circumstances etc.) need to work together as well.

I am grateful to my advisor, Vinny Manoharan, for all the knowledge I gained from him on approaching scientific problems, thinking about concepts, writing and presenting effectively, and attempting to make good jokes. Thank you for setting ambitious goals and holding high standards while trusting my ability to reach them. Thank you for helping me find my passion, get excited about research projects and career options. I am grateful for all the opportunities and support you have provided over the years, both explicitly and implicitly. Your mentoring and guidance have helped me grow and feel confident to step towards the next steps of my career.

It has been a great pleasure working with Professor L. Mahadevan, member of my thesis committee and collaborator. Thank you for participating in interesting and productive discussions on projects while also being kind and welcoming in person. I am grateful to Professor Chris Rycroft, member of my thesis committee and collaborator. Thank you for providing very helpful feedback on my work and being supportive throughout.

I thank Edvin Memet for being an amazing collaborator and developing theory of random parking on a cylinder. I am thankful to Henry Wilkin for his contribution in simulating cylindrical crystals and useful insights. I thank Dan Beller, who played a significant role in initiating the project on cylindrical crystals and has provided great

feedback. I am grateful to Cyril Chomette for developing the synthesis method of plasmonic nanocluster and for being a wonderful collaborator and friend during his time at Harvard.

I like to take the opportunity to thank my mentors, colleagues, and friends in Harvard. Nicholas Schade, my first mentor at Harvard, thank you for being really supportive during my first couple of years in the lab. You have taught me not to be afraid to ask any question. I see you as a role model not just in doing science, but also in honing my creative skills, such as writing songs and parodies for defense/farewell parties. I thank Jessica Sun for taking over my baby-projects on cones and negative curvature substrates. Not only did I learn a lot brainstorming and discussing ideas with you, your fresh and endlessly positive perspectives have given me the much needed positive energy during my last year of PhD. I thank Charlie Greboval and Talha Rehman, whom I had the opportunity to work with and mentor during summer. Your contribution to the project and helping me develop mentoring skills will always be precious.

A significant part of my growth during my time in Harvard did happen outside of the lab. I thank John Girash, the graduate program director of SEAS, for training and mentoring me to work as the departmental pedagogy fellow for two years. Taking his teaching practicum course in my third year was a game-changer for me; since then I have never stopped ‘putting my teaching-hat on’. Thanks for introducing me to this wonderful world of pedagogy and be a part of my happiest moments at Harvard. I am grateful to Marty Samuels for being my mentor at the Bok Center for teaching and learning; I never get tired listening to and learning from your extraordinarily

insightful and considerate perspectives on teaching.

I am grateful to my colleagues at Manoharan lab with whom I have developed friendship and collaborations. Irep Gozen, my first postdoc-friend, thanks for being unnecessarily worried about my willful and temporary disappearances both from lab and from social media. Your ‘stop complaining and just do it’ attitude will always be a good reminder for me to think of things objectively. Danai Montalvan, thanks for constantly reminding and helping me to take care of myself which I forget quite often. I admire your passion in science and perseverance skill and enjoyed collaborating with you on the liquid crystal project. LaNell Williams, thanks for being a great colleague, understanding my personal struggles, and helping me find resources for additional work opportunities on campus. I thank Guangnan Meng, whose advice while troubleshooting my experiment almost saved my life twice. I am grateful to Cheng Zeng for participating in discussions on experiments and helping me find references for paper. I thank all my other colleagues at the Manoharan lab who helped me find things around and provided useful feedback on my research and presentations. I thank my friends outside of the lab - Hemi Gandhi, Shiang Fang, Nanxi Li, Joonhee Choi, Shruti Mishra, and many others. Meeting with all of you during my first couple of years has helped my transition into grad school significantly.

Looking back, I’d not be able to pursue a PhD if I did not receive the academic background and support from my undergraduate institution - the University of Tokyo. I am grateful to my undergraduate thesis advisor Takashi Yatsui, who immediately after hearing my plans to apply for grad schools said ‘you should apply to Harvard’; I would not have the courage to do so without him saying that. I am also thankful

to Professor Motoichi Ohtsu, whose comment ‘in research, you only fail when you decide to give up’ engraved in my mind motivated me to get back to the lab next day after a failed experiment. I thank my first mentor, Mochizuki Takahiro; who told me (when I was freaking out after breaking an expensive equipment) ‘we just have to fix the problem’ – I figured it is a great way to perceive life in general. I am grateful for the wonderful support I got from my friends in Tokyo during my time there and even afterwards - Himasha Rukhshani Dharmalapala, Minh Tran Anh, Ken Ong, Susmita Saha, Shajib, Shouman, Dipto, and other members of the jpugrads community.

Finally, I like to thank my family - my sister, Nafisa Tanjeem, for being the inspiration of setting bold aims and challenging things that are perceived as ‘normal’. I thank my little sister, Najifa Tanjeem, for her amazing ability to make me happy even in difficult situations. Lessons I learned from my mother, Fatema Nasreen, to be independent and resilient since I was a child, have always encouraged me to explore new places and ideas fearlessly. I am also thankful for having a caring father, Abdus Sattar. I thank members of my extended family for being very helpful from time to time in reminding me who I am and what my goals are.

Growing up as a young girl in Bangladesh, it was not easy to dream of being a scientist, getting a PhD in Applied physics, or even living an independent life. I am grateful to all the people (some mentioned here, some are not), who paved my way so that I have dared to build my own dreams and fight against the obstacles waiting for me. I dedicate my work to students coming from a similar background, who have decided to never give up pursuing a dream that is much bigger than that of their surroundings.

Chapter 1

Introduction

Looking around in nature, we find a variety of structures with interesting geometrical features. The structure of a sunflower head, the pattern on a corn cob, and the spherical and tubular shapes of viruses have drawn the interest of scientists across multiple disciplines [7, 8, 9]. How do these structures form and why do they take their natural shape? Although there is no simple answer to these questions, a good way to approach this problem is to look for the design rules that the building blocks of these structures follow to assemble into their final shapes.

Current technology does not allow us to observe self-assembly in real time at the atomic or molecular scale. Fortunately, many aspects of the physics of self-assembly remain valid even if the building blocks are larger than atoms or molecules, such as colloidal microspheres [10]. Self-assembled colloidal microspheres have been used to realize numerous phenomena related to self-assembly, such as phase transitions [11], crystal nucleation and growth [12], melting [13], and the glass transition [14].

In this dissertation, I use colloidal microspheres to understand the effect of geometry

on self-assembly. Although this problem has gained attention in recent years, there are still many unresolved problems because of the diversity of geometric parameters. I address a few of them here and discuss how this knowledge can be used not only to understand nature but also to design functional materials inspired by nature.

1.1 Self-assembly of colloidal spheres

In our colloidal systems, solid microspheres with an average diameter in the range of 700 nm to 1300 nm are dispersed in liquid. These microspheres exhibit Brownian motion and they self-assemble in experimental timescales owing to their interactions with each other and their interactions with a surface. Below, I describe the types of interactions we use to drive self-assembly in our experimental system.

1.1.1 Colloidal interactions

Depletion interaction. Depletion is an entropic interaction that requires a binary mixture of colloids. Consider a solution with a mixture of large spheres and small spheres, where small spheres outnumber the large ones (Fig. 1.1). Each large sphere develops a depletion zone around it where the center of the small spheres cannot enter owing to their size. When the depletion zones of the large spheres overlap, the available volume of the small spheres increases, resulting in a net increase of entropy and reduction of free energy. Consequently, as the system approaches equilibrium, the large spheres form ‘bonds’ with each other through an attractive interaction. The

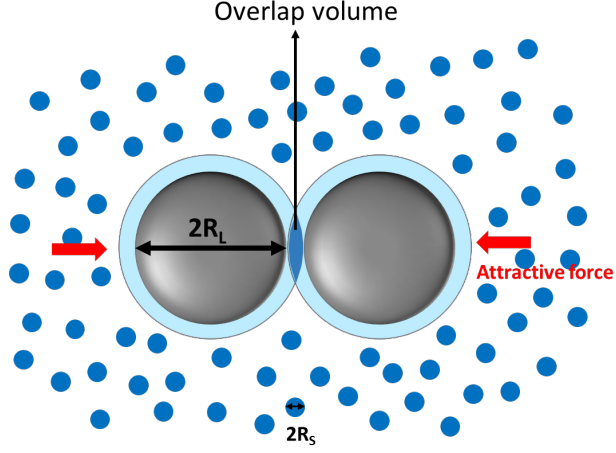


Figure 1.1: Mechanism of depletion interaction in a binary mixture of large spheres (radius R_L) and small spheres (radius R_S). The light-blue region around each large sphere shows the ‘depletion zone’ where the center of the small spheres cannot enter. The dark-blue region in between the large spheres is the overlap volume of the depletion zones.

depletion potential can be modeled using the following equations [15, 16]:

$$U(r) = \begin{cases} -k_B T N_S V_{OV} & \text{if } r < 2R_S \\ 0 & \text{if } r \geq 2R_S, \end{cases} \quad (1.1)$$

where k_B is the Boltzmann constant, T is room temperature, and V_{OV} is the volume of overlap between the large spheres. V_{OV} is a function of the particle center-to-center distance r . For two spherical particles, this volume is

$$V_{OV}(r) = \frac{\pi}{6} (2R_L + 2R_S - r)^2 (2R_L + 2R_S + \frac{r}{2}), \quad (1.2)$$

where R_L is the radius of the large spheres and R_S is the radius of the small spheres. In a system with fixed R_L and R_S , the depth of the interaction potential can be tuned by changing the number of small spheres (N_S).

Electrostatic interaction. Any neutral body dispersed in a solution can form an inhomogeneous distribution of ions. The distribution of the counter-ions, consisting of a Stern layer and a diffuse layer, determines the shape of the electrostatic potential away from the surface [17] (Fig. 1.2a). When two charged bodies come close together, their double layers overlap, resulting in an attractive or a repulsive electrostatic interaction (Fig. 1.2b).

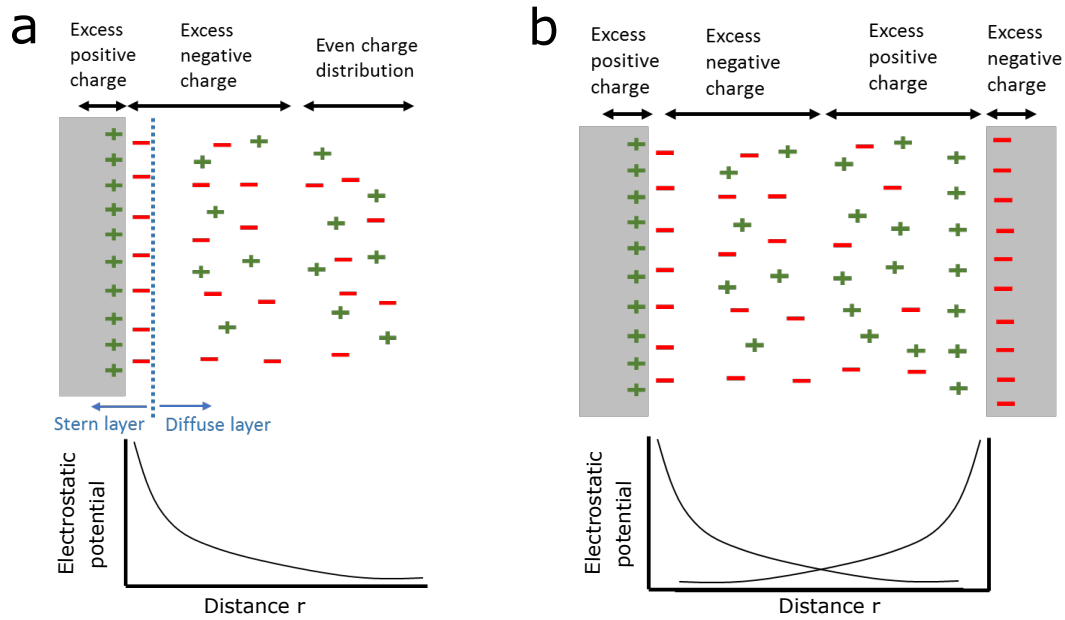


Figure 1.2: **(a)** A positively charged surface. Some negative counter-ions accumulate very close to the surface, creating the ‘Stern layer’. Other negative counter-ions diffuse nearby, forming the ‘diffuse layer’. Both of these layers determine the shape of the interaction potential which is a function of distance r from the charged surface. Away from the surface, the charge distribution is uniform and hence the potential is zero. **(b)** When two oppositely charged bodies come close to one another, their double layers as well as the interaction potential curves overlap, resulting in an attractive force.

The potential energy of electrostatic interaction between two spherical charged

bodies can be modeled as follows [18]:

$$U(r) = -k_B T Z_p^2 \lambda_B \left(\frac{e^{\kappa R_L}}{1 + \kappa R_L} \right)^2 \frac{e^{-\kappa r}}{r}, \quad (1.3)$$

where Z_p is the surface charge valence on the sphere, λ_B is the Bjerrum length, and κ^{-1} is the Debye screening length

$$\kappa^{-1} = \sqrt{\frac{k_B T \epsilon_0 \epsilon}{2 Z^2 e^2 \rho}}, \quad (1.4)$$

where ϵ_0 is the dielectric permittivity of vacuum, ϵ is the dielectric constant, Z is the valency of the ions in solution, e is the fundamental charge, and ρ is the ion concentration in solution. The depth of the electrostatic interaction potential can be tuned by changing the surface charge Z_p . The range of the potential depends on the Debye length κ^{-1} , which can be tuned by changing the ion concentration in the solution, ρ .

DNA hybridization. Another way to design colloidal interactions is to use DNA hybridization. Microspheres and surfaces that are covered with complementary DNA strands assemble owing to the effective attractive interaction shown in Fig. 1.3c. The depth of this interaction potential can be controlled by tuning the DNA hybridization enthalpy or by tuning temperature.

1.1.2 Packing and parking

By designing the appropriate interaction potential, one can cause colloidal spheres to self-assemble into a particular structure. In the case of a weak interaction with a potential energy depth of a few $k_B T$, particles do not bind irreversibly once they

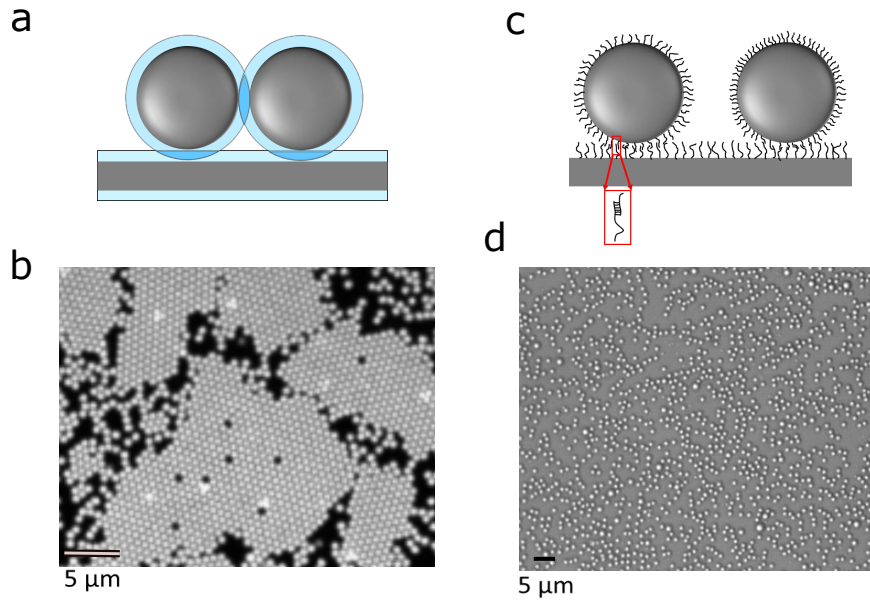


Figure 1.3: (a) Diagram of depletion interaction between colloidal spheres and a flat surface, showing the overlap in excluded volume (blue). (b) Image taken with a confocal microscope showing colloidal spheres (average diameter 710 nm) packing on a flat glass surface. The depth of the interaction potential is small enough that the particles can find their maximum packing configuration. (c) DNA hybridization between colloidal spheres and a flat surface coated with DNA strands with complementary sequences. (d) Image taken with a bright-field microscope showing colloidal spheres (average diameter 1.3 μm) park on a flat glass surface. The depth of the interaction potential is large, as a result, particles stick irreversibly to the glass surface.

come into contact with one another or with a surface. As a result, they can explore different configurations and eventually reach equilibrium. Fig. 1.3a and Fig. 1.3b shows an example of colloidal spheres packed on a flat glass surface through depletion interactions. Because of the geometry of the overlap volume, the interaction potential between a particle and a flat surface is stronger than the interaction potential between two particles (Fig. 1.3a). Once the spheres attach to the flat surface, they can slide on the surface, find other particles, bind and unbind multiple times, and eventually

find a low energy configuration in which particles pack densely (Fig. 1.3b).

In the case of a strong interaction, the particles may fail to reach equilibrium. One example of such assembly is shown in Fig. 1.3c and Fig. 1.3d, in which case, the particles and the glass surface are covered with DNA strands with complementary sequences. In this case, once the particles bind to the surface, they cannot unbind or slide. As a result, their final configuration is disordered and not densely packed. This process is often referred to as ‘random parking’ analogous to the problem of car parking [19]. A system with randomly parked colloidal spheres may never reach equilibrium; however, it may reach a jammed state in which there is no space left to add a new particle.

1.2 Self-assembly on a cylindrical substrate

When spheres are packed *inside* a thin cylinder, they can spontaneously form helical structures (Fig. 1.4). These diverse structures have been examined in theory and experiment [1, 20, 21, 22, 23]. The same types of structures have been reproduced in simulations for a system in which colloidal spheres assemble *on* the surface of a cylinder [2]. This work by Wood, Santangelo, and Dinsmore carefully examined the structures for different ratios of the cylinder circumference to the sphere diameter. The results show that for some discrete size ratios (shown by the gray circles in Fig. 1.5) a perfect crystal can be accommodated around the cylinder circumference. For other size ratios, either an asymmetric crystal (shown by blue dots) or a defect (shown by orange dots) appears. For a particular size ratio, the preference for asymmetric lattice or a defect is determined by the interaction range [2].

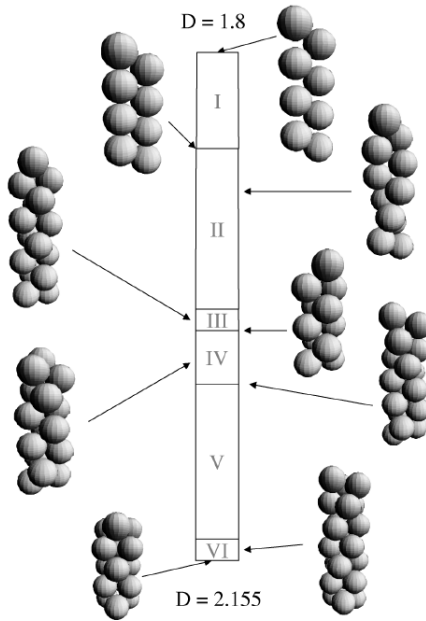


Figure 1.4: Close packed configurations of hard spheres inside a cylinder, examined by Pickett and coworkers. Different configurations are found as the cylinder-to-sphere diameter ratio D varies in the range of $1 < D \sim 2.155$. Six different regions are defined as denoted by I-VI; the corresponding structures in those regions are indicated by the black arrows. Figure reproduced from reference [1].

All of these studies focus on the maximum packing scenario. The non-equilibrium and random parking scenario have been examined theoretically for cylinders with large diameter [24]. Nevertheless, there is a lack of experimental studies that examine the self-assembled structures and assembly dynamics in both finite-temperature and non-equilibrium cases.

1.3 Overview of thesis

To bridge the gap between theory and experiment, we design experimental systems to study self-assembly on cylindrical substrates. In Chapter 2, I show the results of an

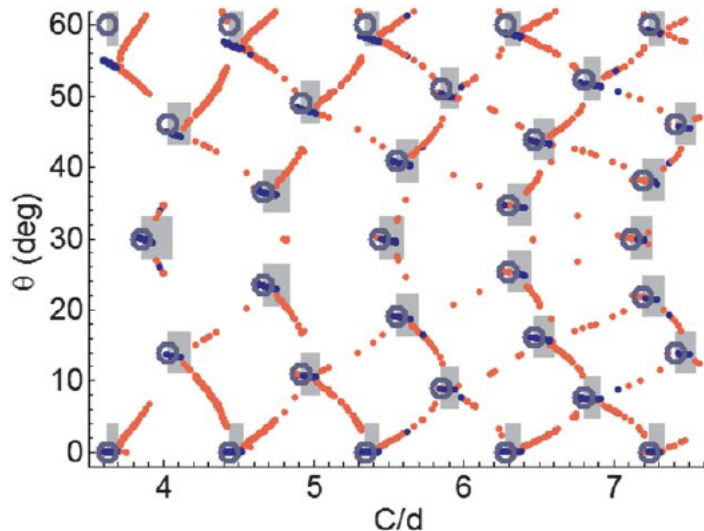


Figure 1.5: Phase diagram of chirality (or helicity) as a function of size ratio calculated by Wood, Santangelo, and Dinsmore [2]. When the interaction range between the spheres is short, defect structures (orange dots) are preferred over asymmetric crystal structures (blue dots). Figure reproduced from reference [2].

experimental study on crystallization of colloidal microspheres on a micrometer-sized cylinder through a weak depletion interaction. I observe a specific type of defect called as ‘line-slip defect’ in single crystals that wrap around the cylinder, previously predicted in theory and simulations. Surprisingly, the defects can take varying shapes that include kinks and fractional vacancies. Using theory and simulations, we and our collaborators demonstrate that these varying shapes emerge because of anisotropic crystal growth dynamics on the surface of the cylinder. In Chapter 3, I examine the size, length, and anisotropy of multiple single crystalline grains formed along the length of a cylinder. I show that the grain length along the cylinder remains consistent, with the exception of very thin cylinders, whereas the grain size and anisotropy vary as a function of cylinder size. In Chapter 4, I demonstrate an experimental system to study

non-equilibrium random parking on a cylinder with high curvature. Using theory and simulations, we and our collaborators show that the surface coverage fraction is a function of cylinder curvature and deviates from the value on a flat 2D surface. I show that our experimental observations are consistent with this theory. In Chapter 5, I demonstrate a new multi-step synthesis approach to fabricate octahedral plasmonic nanoclusters. The synthesis approach developed by our collaborators results in high yield and precisely controlled geometry. Using dark-field spectroscopy measurements and finite-difference time-domain simulations, I show that the plasmon resonance peaks of the nanoclusters are consistent from cluster to cluster, confirming our ability to control the geometry precisely. Finally, in Chapter 6, I present some new problems that are inspired by the findings of my experiments, such as defect and sublimation dynamics of the kinked line-slip structures in cylindrical crystals. Additionally, I propose and present preliminary results on two systems in which geometric frustration can be designed in different ways.

Chapter 2

Crystal morphology and growth dynamics on a cylinder

The research described in this chapter is done in collaboration with William H. Wilkin, Daniel A. Beller, and Chris H. Rycroft. The research was supported by the National Science Foundation under grant no. DMR-1420570.

2.1 Introduction

The morphology of a crystal depends on the curvature and topology of the substrate it grows on. As shown in experiments on colloidal crystals, a crystal on a surface with nonzero Gaussian curvature must incorporate topological defects [25, 26, 27] or grow anisotropically [18] when it becomes large enough. Simulations have also shown that a crystal growing on a topologically closed surface may face a ‘closure catastrophe’ in which the accumulation of defects halts the crystal growth [28, 29]. Most studies on

these constraints have focused on crystals on the surface of a sphere, in which case both Gaussian curvature and topology affect the crystallization dynamics. A cylinder, however, has zero Gaussian curvature, but also has a surface that loops back on itself. Hence, crystals grown on a cylinder provide an opportunity to study the effects of a closure constraint at zero Gaussian curvature.

One known consequence of the closure constraint is chirality. For hard spheres on a hard cylinder, theory and simulation have shown that chiral crystals are the ground states for certain values of the ratio of the cylinder diameter to sphere diameter [21]. Between these size ratios, the ground states incorporate defects known as line slips [21, 30, 2]. Chiral crystals have been observed in experiments on spherical particles confined inside a cylinder, where the cylinder is small enough that all the particles touch the surface [23, 22]. Line slips have been observed in wet foams confined to a cylinder [31]. However, all of these studies examine only the ground state.

Our study examines how the *process* of crystallization at finite temperature is affected by the cylindrical constraint. By directly observing colloidal microspheres crystallizing on a micrometer-sized cylinder, we can see how the morphology evolves with time. At long times, we observe chiral crystals and chiral line-slip defects, as expected, but we also observe some unexpected structures that arise from the growth process: kinked line slips that incorporate fractional vacancies. We show that as a crystal wraps around the cylinder, its growth becomes anisotropic, and line-slip defects that are misaligned with the growth direction form kinks rather than straight lines. This connection between morphology and growth dynamics may shed some light on the formation mechanism of many natural and artificial tubular structures.

2.2 Crystal formation on a cylinder

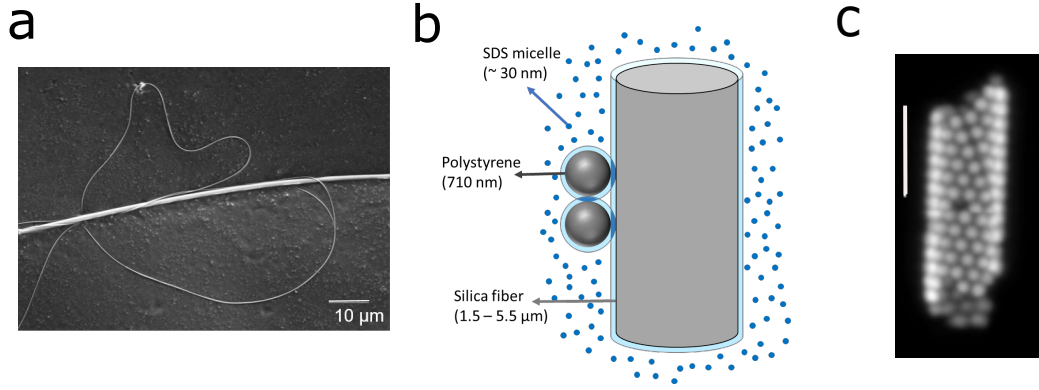


Figure 2.1: **(a)** Scanning electron microscopy image of a tapered optical fiber. Both thick and thin parts belong to the same fiber. The original fiber diameter is $125\,\mu\text{m}$, and the smallest diameter in the tapered part is about $200\,\text{nm}$. **(b)** Setup for depletion interaction. Colloidal particles have an average diameter $D = 710\,\text{nm}$. Sodium dodecyl sulfate (SDS) forms micelles with an effective diameter of $30\,\text{nm}$ [3, 4]. These micelles induce a short-ranged depletion force between the particles. We examine crystallization where the diameter d of the cylinder is between $1.5\,\mu\text{m}$ and $5.5\,\mu\text{m}$. **(c)** Projection of a stack of confocal microscope images of colloidal crystals formed on the surface of a cylinder.

In our experimental system, a quasi-two-dimensional (2D) colloidal crystal self-assembles on the surface of a cylinder, driven by a short-ranged depletion interaction between the particles and between the particles and cylinder. We fabricate a cylinder by simultaneously heating and pulling a silica optical fiber [32, 33, 34]. This method results in a tapered cylinder with a diameter d of a few micrometers and with a smooth surface for crystal growth (Fig. 2.1a). We use colloidal polystyrene particles with an average diameter of $D = 710\,\text{nm}$ as building blocks for crystallization. The interaction range is approximately the effective diameter of the depletant micelles, or about 4.2%

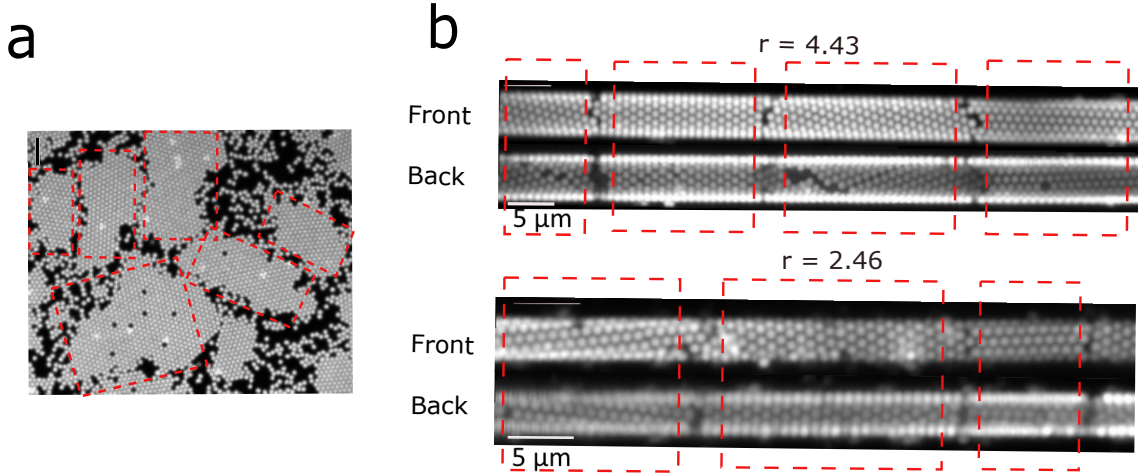


Figure 2.2: **(a)** Confocal microscope images of colloidal crystals formed on a flat 2D surface, where there is no closure constraint. Each red dotted box denotes one single crystalline grain. **(b)** Confocal microscope images of crystals assembled on cylinders for different cylinder-to-sphere diameter ratios $r = d/D = 4.43$ (top) and 2.46 (bottom). Inside each red dotted box, we show the front and back of a single crystal wrapped around the cylinder. The single crystals are identified by the consistent chiral angle found at both sides of the cylinder.

of the particle size at the SDS concentration we use (Fig. 2.1b) [3, 4]. We adjust the concentration of colloidal particles (0.25% w/v) and SDS (33.6–34 mM) to avoid formation of multiple crystal layers or large particle clusters.

After preparing the sample, we observe multiple crystals growing on the cylinder. Within 3–5 hours, the cylinder is almost entirely covered by particles. On both a flat surface (Fig. 2.2a) and cylinder (Fig. 2.2b), we observe multiple crystalline grains. Because our goal is to study the closure of individual grains, we limit our observations to $r = d/D < 10$, in which case we see single crystalline grains that wrap completely around the cylinder and multiple crystalline grains formed along the length of the cylinder (Fig. 2.2b). Because the diameter of the cylinder varies slowly along its

length, we can assess the effects of the size ratio by observing crystals on different parts of the same cylinder. However, the diameter variation of the cylinder across the length of a single crystal is small enough that we can approximate the geometry as a cylinder rather than a cone.

2.3 Chiral crystals and chiral defects

Our self-assembled cylindrical crystals have structural features that are not seen in crystals on a flat surface. One such feature is chirality. Previous work has shown that perfect chiral crystals should appear for integer values of the chiral indices m and n [21] (Fig. 2.3a). These indices determine the size ratio and chiral angle of the crystal. In our experiments, some of the crystals we observe are perfect crystals (Fig. 2.3b). For these crystals, we characterize the chiral angle, which is easier to measure than m and n . As shown in Fig. 2.3b, we observe that crystals with different chirality spontaneously assemble on different parts of the cylinder.

Another structural feature not present in flat crystals is the line-slip defect, which consists of a line of particle pairs in which each particle has only five nearest neighbors. The defect is identified from the broken triangular symmetry along a line, which leaves the symmetry of the rest of the crystal unperturbed. The chirality of a line-slip defect is related to the chirality of the crystal. We observe line-slip defects in our system, as shown in Fig. 2.4. Such defects have been observed previously in macroscopic systems [30, 31] but not, to our knowledge, in a self-assembled system.

Chirality and line-slip defects are specific to cylindrical crystals. Because both m and n are integers, a perfect crystal can form only for discrete values of the size

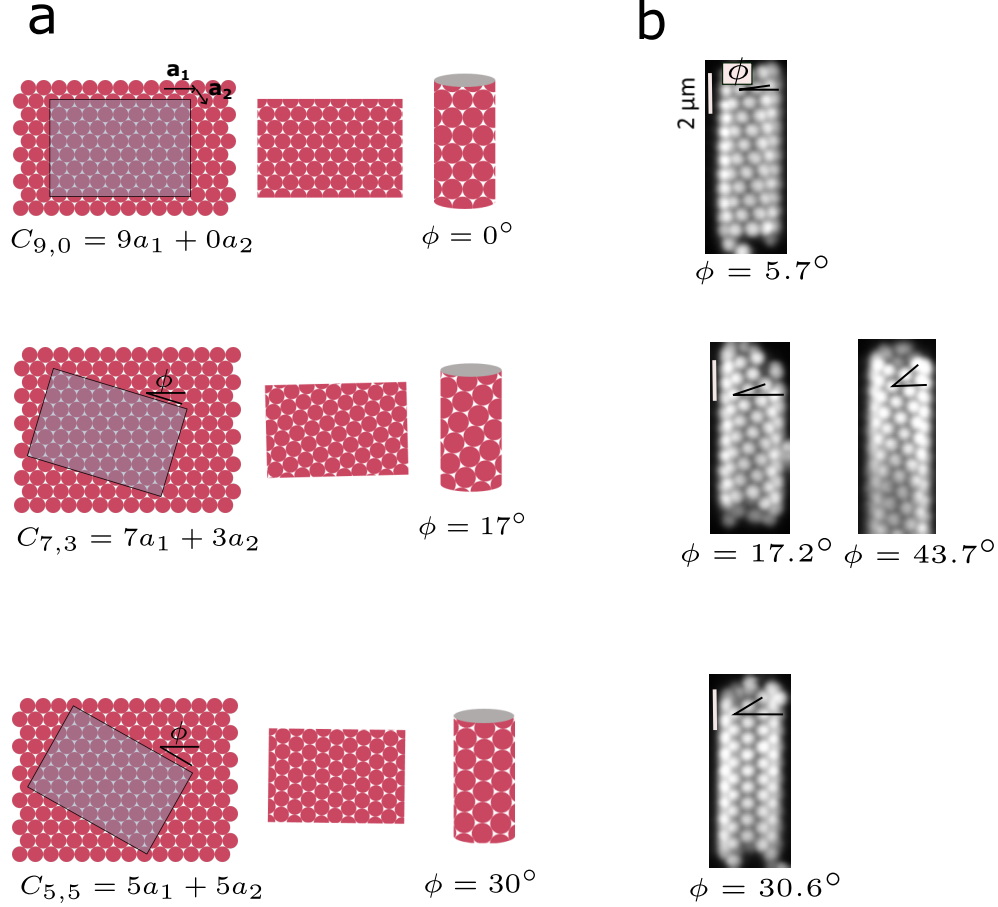


Figure 2.3: **(a)** Formation of a crystal without any defects requires that the cylinder circumference C be an integer linear combination of the lattice vectors \mathbf{a}_1 and \mathbf{a}_2 : $C_{m,n} = m\mathbf{a}_1 + n\mathbf{a}_2$. The chiral angle ϕ of the crystal depends on the integers m and n . For example, configurations (9,0) and (5,5) are achiral, whereas configuration (7,3) is chiral. **(b)** Confocal microscope images of crystals with different chirality observed in experiment. The four crystals are observed at different parts of the same tapered cylinder. We measure the chiral angle ϕ of each crystal from the images.

ratio r . Between those size ratios, the ground state must either break symmetry or incorporate a line-slip defect [21]. Previous simulations on self-assembled cylindrical crystals suggested that long-ranged interactions favor asymmetric crystals and short-ranged interactions favor line slips [2]. In our short-ranged system, line-slip defects

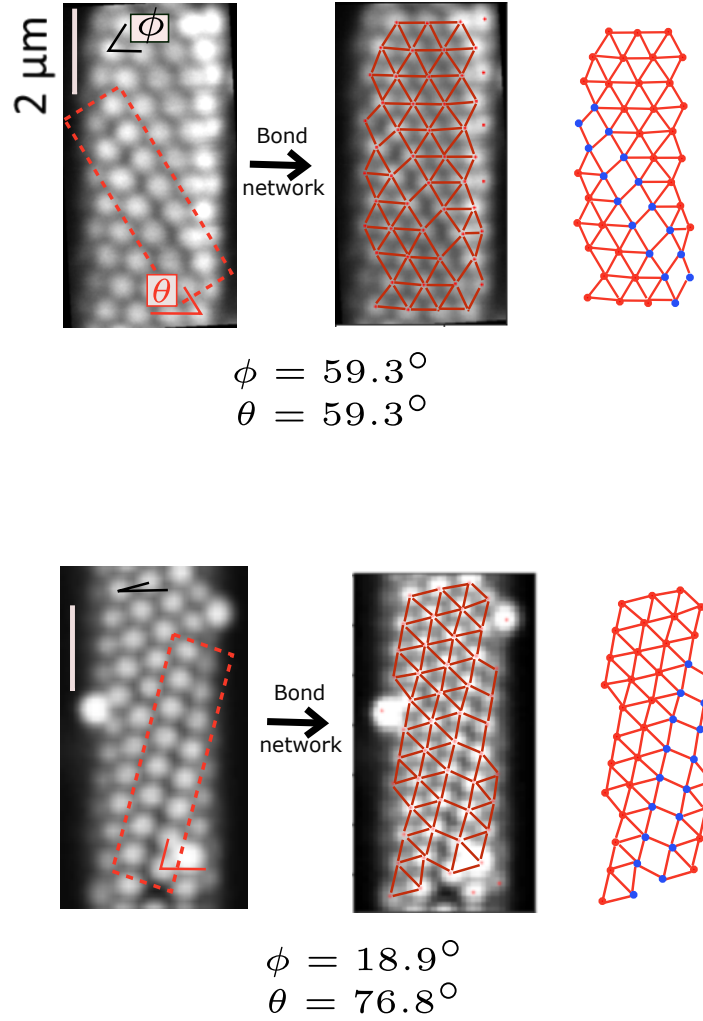


Figure 2.4: Images of line-slip defects with different chirality, along with the bond network extracted from the images. The chirality of a line-slip defect is defined by the angle θ that the slip line forms with the circumferential axis of the cylinder. The blue circles show the positions of particles that form the line-slip defect, and the red circles show the other particles in the crystal. All scale bars are $2\mu\text{m}$.

indeed appear, though at larger size ratios ($r = 2.00\text{--}8.00$) than those probed in these simulations ($r = 0.1\text{--}1.4$).

The line-slip defects we observe are stable for the duration of our experiments (up

to 18 hours), except for the formation of some vacancies. As shown in simulation and theory [21, 2], line-slip defects are ground-state defects that appear at specific size ratios r and cannot disappear unless the crystal unwraps and finds a different configuration. We sometimes see defects similar to line slips in 2D crystals on a planar surface, arising between two different crystalline grains with the same crystalline orientation. However, such defects disappear when the grains translate. In contrast, line-slip defects on the surface of the cylinder cannot relax by shear because doing so would change the circumference of the crystal.

2.4 Line-slip defects with kinks

We also observe a new class of defect not previously seen in simulation. These defects consist of two or more parallel line-slips, connected by what we call ‘kinks’ (Fig. 2.5). Gaps appear in the kinks, which we call ‘fractional vacancies’ because one full particle cannot fit inside. We find that kinked line-slip defects emerge in crystals with different chiral angles and with a variety of number of fractional vacancies, as shown in Fig. 2.5.

To understand the origin of the kinks and fractional vacancies, we first consider the possibility that they are equilibrium defects, similar to vacancies in a planar crystal. As with vacancies, we expect that some fractional vacancies should occur in equilibrium, owing to entropy. The fractional vacancies would not have appeared in previous simulations on cylindrical crystals because these simulations examined the ground states.

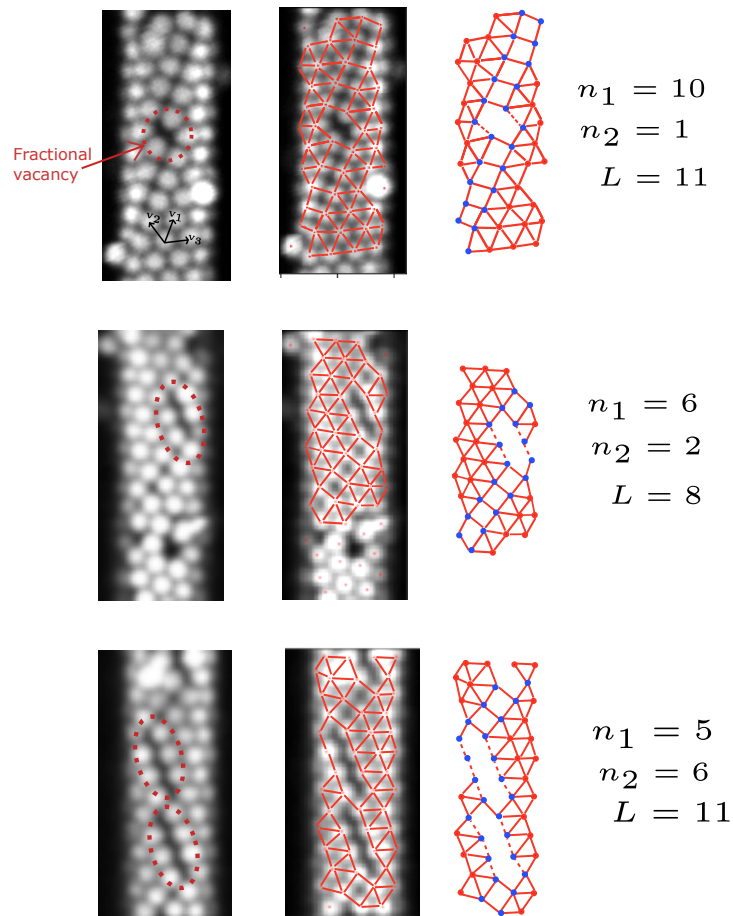


Figure 2.5: Confocal images and bond networks of three kinked line-slip defects with different number of fractional vacancies. n_1 is the total length along the line-slip defect in units of particle center-to-center distance along the lattice direction \mathbf{v}_1 . n_2 is the length along a second lattice direction \mathbf{v}_2 . Along this line, none of the particles are in contact with another particle across the line-slip; they are instead in contact with the fractional vacancies. We define the line-slip length $l = n_1$ and the path length, including the fractional vacancies, as $L = n_1 + n_2$.

We use a statistical mechanical model to calculate the equilibrium number of fractional vacancies and the equilibrium length of the kinked line slips. Two parameters characterize the geometry: the line-slip length l is the effective length of a line-slip

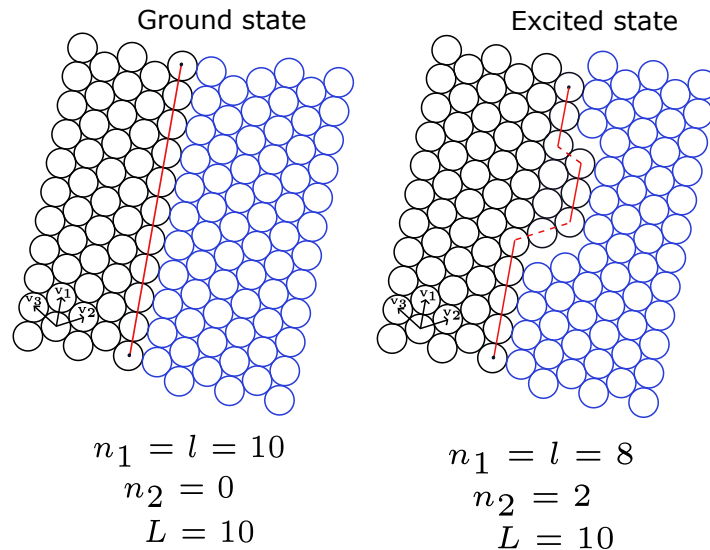


Figure 2.6: A model used to calculate the equilibrium length l_{eq} of a line slip. The line slip is where the black and blue halves of the crystals meet. The length of the red solid line along the line slip is equal to n_1 , and the length of the red dotted line is equal to n_2 . In the limiting case of a straight line-slip defect without any kinks, $n_2 = 0$ and $L = n_1 = l$. Starting from this ground state, we calculate all the possible configurations of the defect using lattice vectors \mathbf{v}_1 , \mathbf{v}_2 , and \mathbf{v}_3 , assuming the circumference of the cylinder is larger than L .

defect, excluding the fractional vacancies, and the total length L is the length including the fractional vacancies (Fig. 2.5). In the ground state, $L = l$, but in excited states, there are fractional vacancies, and the effective line-slip length becomes shorter, such that $l < L$ (Fig. 2.6). For a given total length L , we calculate all possible configurations of kinked line-slip defects, as shown in Fig. 2.6, and then we calculate the equilibrium length l_{eq} using Boltzmann statistics. The equilibrium average length l_{eq} is smaller than L , reflecting the number of fractional vacancies in equilibrium.

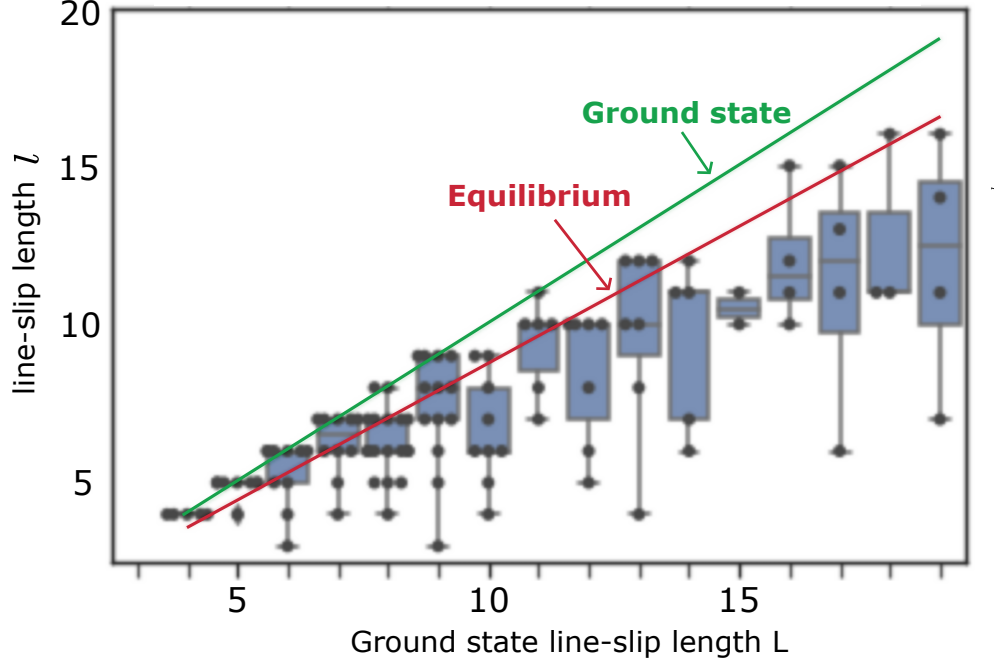


Figure 2.7: Plot of l as a function of L for ground states, equilibrium, and experiment. In the ground state, $L = l$. The equilibrium length l_{eq} represented by the red straight line is calculated from the model assuming $E_b = 4k_B T$. To find l from experiment, we measure n_1 and n_2 from images of 116 crystals and calculate $l = n_1$ and $L = n_1 + n_2$. The black points represent each crystal and the blue boxes show the distribution of l for each L .

We find that l_{eq} predicted by the model is greater than the measured l for most of the crystals when we choose $E_b > 2k_B T$ in the model (Fig. 2.7). Because stable crystal grains should not form when $E_b < 2k_B T$ [18], the experimental E_b must be greater than $2k_B T$. From this observation we realize that while the kinks and fractional vacancies may well correspond to elementary excitations in an equilibrium line-slip defect, there are many more of them than expected in equilibrium. Thus, we conclude that the kinked line-slip defects found in experiment are not in equilibrium.

2.5 Mechanism of kink formation

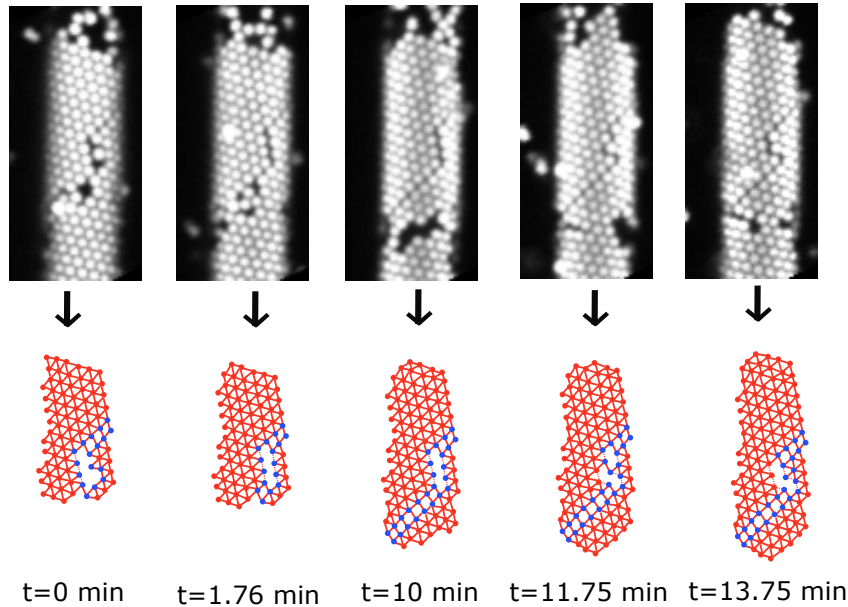


Figure 2.8: Confocal images showing the formation of a kinked line-slip defect. At $t = 0$, a line-slip defect begins to form when the crystal wraps around the cylinder. At $t = 1.76 \text{ min}$, another line slip starts forming in a parallel line, leaving fractional vacancies between the two. The line slips continue to grow until $t = 10 \text{ min}$, after which we observe fluctuations in the kinked shape but not in the number of fractional vacancies.

An alternative hypothesis for the origin of the kinks is kinetic trapping during crystal growth. To check whether kinetic trapping might be occurring, we observe the dynamics of crystal growth in experiment (Fig. 2.8). We find that kinked line slips tend to form when two parallel line slips grow, trapping fractional vacancies in between. We find that most kinked defects do not relax and turn into a straight line-slip defect on the timescale of the experiment, instead showing only thermal fluctuations near the fractional vacancies (Fig. 2.8). This result suggests that the kinked defects can indeed be kinetic traps and can result from crystal growth dynamics.

In contrast, crystals that grow without incorporating a line-slip defect close without being kinetically trapped.

To understand what dynamics give rise to the kinked morphology, we perform Brownian dynamics simulations. These simulations confirm that the kinks arise during growth and not afterward (Fig. 2.9), but they also reveal a surprising feature: the number of fractional vacancies depends on the chiral angle of the crystal, or the angle between the line slip and the circumferential axis of the cylinder. In crystals with larger chiral angles, the line slips are almost straight with very few fractional vacancies, while in crystals with smaller chiral angles, the line slip incorporates a greater number of fractional vacancies.

This correlation between the chiral angle and the number of fractional vacancies is present in both simulation and experiment. To quantify the correlation, we calculate the parameter $\delta = (L - l)/L$, which is the number of fractional vacancies per unit length of the total defect. We measure θ and δ for 79 simulated crystals and 116 crystals in experiment and find that δ decreases with increasing θ in both cases, as shown in Fig. 2.10a and 2.10b.

2.6 Effect of crystal growth anisotropy on morphology

The negative correlation between θ and δ provides an important clue about how the cylindrical geometry affects crystal growth. It suggests that the cylinder itself makes the growth anisotropic. We make sense of this result as follows. On a flat plane,

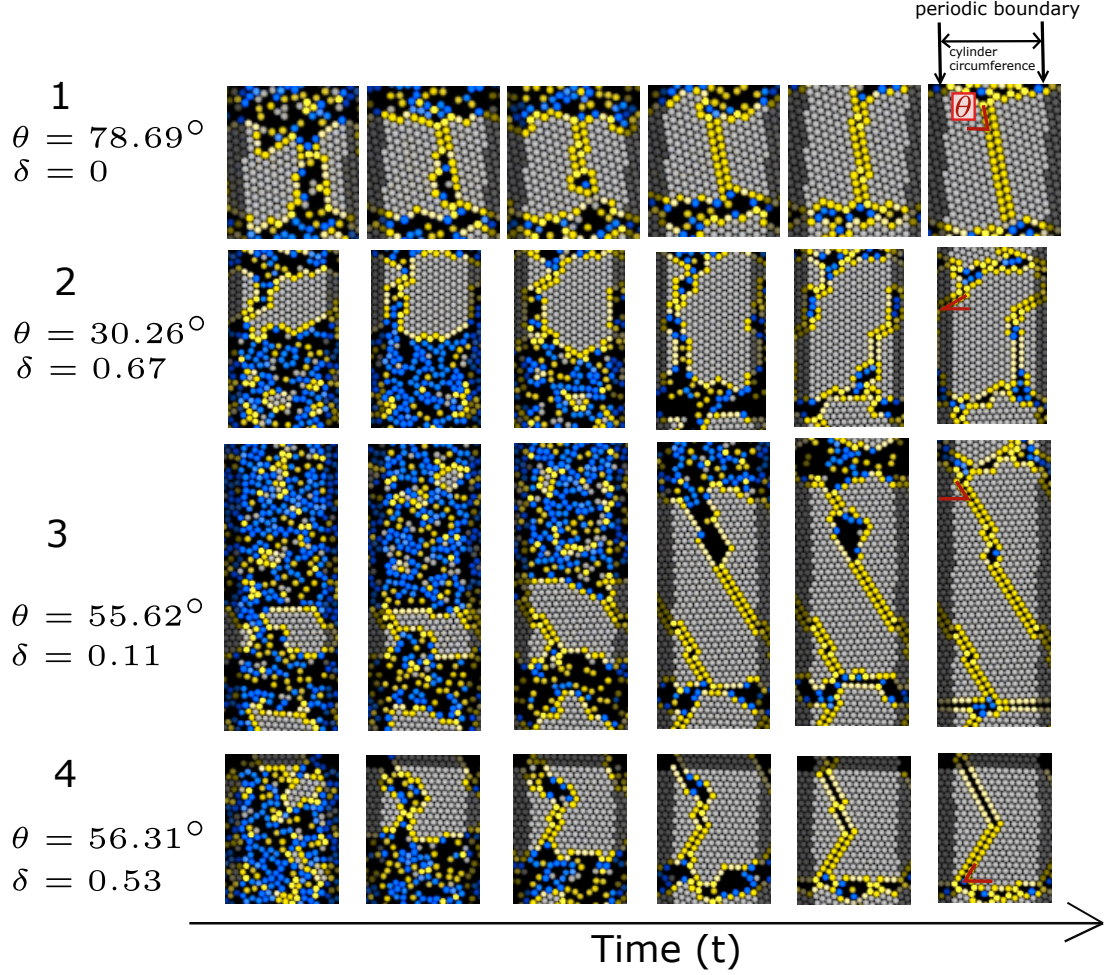


Figure 2.9: Images from Brownian dynamics simulations of crystal growth. In each image the crystal is shown cut and unwrapped, such that the entire circumference of the cylinder is visible. All four crystals shown here form on a cylinder with the same circumference. The line-slip defect of crystal 1 (identified by the yellow particles) has an angle of $\theta = 78.69^\circ$ with respect to the circumferential axis of the cylinder. As the crystal grows, the line-slip sometimes forms a kink (frames 3 and 5 from the left) but quickly rearranges into a straight line slip (frame 6). Crystal 2 has a line-slip defect with a smaller $\theta = 30.26^\circ$. In this case, the line slip fails to follow the crystal growth and traps a number of fractional vacancies. Crystal 2 has a larger value of δ than crystal 1 (0.67 compared to 0). Crystal 3 and crystal 4 both have line-slip angles of about $\theta = 55^\circ$, and their values of δ are also in between those for crystals 1 and 2 ($\delta = 0.11$ for crystal 3 and $\delta = 0.53$ for crystal 4).

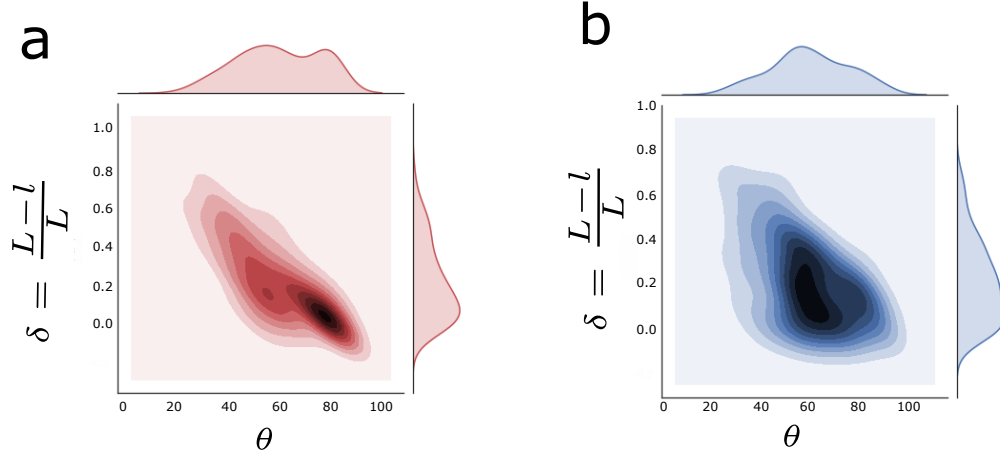


Figure 2.10: **(a)** Contour plot showing probability distribution (kernel density estimate) of kinked line-slip defects as a function of δ and θ for 79 simulated crystals with fixed r . **(b)** Same type of plot as **(a)**, but showing data from 116 crystals found in experiment with varying r . The plots show that the number of fractional vacancies varies with the line-slip angle in the same way, though the correlation coefficient in the experiment (-0.49) is smaller than that of simulation (-0.77), likely because the experimental data are not taken at a single size ratio.

near equilibrium, a crystalline grain grows isotropically. On a finite-sized cylinder, this is true until the grain wraps around the cylinder. Once the crystal touches itself, its growth along the circumferential direction of the cylinder is hindered, whereas that in the axial direction is not. Therefore, if a line-slip is aligned with the cylinder axis (Fig. 2.11a), its growth will be favored by the crystal growth, compared to a line-slip that is less aligned with the cylinder axis (Fig. 2.11b).

To validate this interpretation, we observe crystal growth at different line-slip angles in simulation and measure how the lengths of all three faces of the crystal change over time. We find that for a line-slip defect with a large chiral angle ($\theta = 80.5^\circ$), the length of the face aligned with the line slip increases with time while the lengths of other two faces remain stable (Fig. 2.12a and Fig. 2.13a). As a result, this

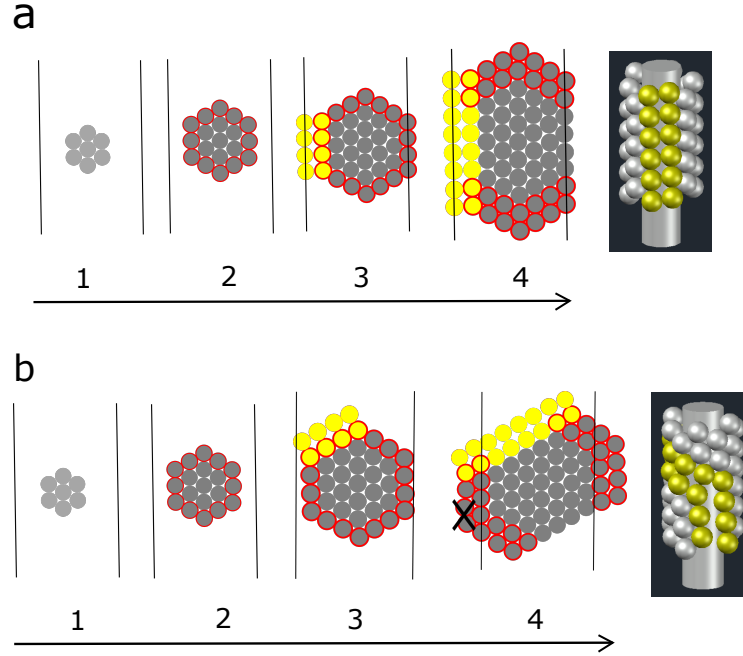


Figure 2.11: **(a)** **(b)** Growth model of line-slip defects in two crystals with same chiral angle ϕ but different line-slip angles θ . At each time, new particles (particles with red circular borders) are added to the faces of the crystal grain. Before the crystal wraps around the cylinder (steps 1, 2, and 3), particles are equally likely to attach to any of the three faces of the crystal, resulting in isotropic growth. Once the crystal wraps around, particles can attach only to the two faces that are not aligned with the cylinder axis (step 4). In **a**, both of these faces make approximately the same angle with the cylinder axis. Thus, the growth rates should be approximately the same, and the line slip (yellow particles) can grow straight. In **b**, the crystal has wrapped around, occluding the vertical face. As a result, the growth rates on the two faces must differ, and therefore the line slip tends to incorporate more fractional vacancies.

line slip incorporates few fractional vacancies, resulting in a small value of δ ($\delta = 0.087$). For a line-slip defect aligned further from the cylinder axis ($\theta = 45^\circ$), we find that the length of the face aligned with the line slip increases over time, but so does the length of one other face (Fig. 2.12b and Fig. 2.13b). In this case, face 2 is the face most aligned with the cylinder axis and face 3 is aligned with the line-slip defect, but less aligned with the cylinder axis. As a result, face 2 and face 3 compete with each

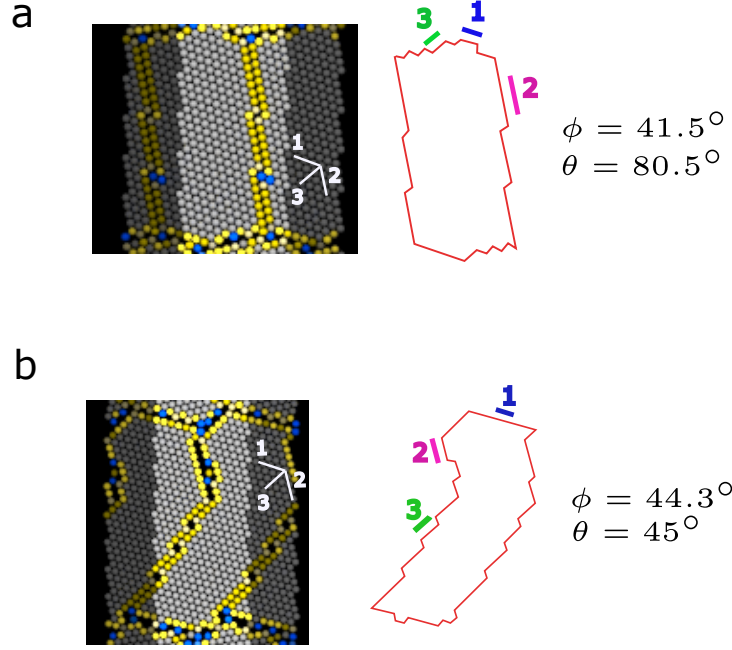


Figure 2.12: (a) A line-slip defect in a crystal found in simulation with $\phi = 41.5^\circ$ and $\theta = 80.5^\circ$. (b) A line-slip defect in a crystal found in simulation with $\phi = 44.3^\circ$ and $\theta = 45^\circ$.

other, and eventually the line-slip defect acquires a number of fractional vacancies owing to the growth of face 2. Consequently, we find a larger value of δ ($\delta = 0.379$).

2.7 Conclusion and outlook

We find that the cylindrical constraint results in three different morphologies for the crystal. The first is a chiral crystal without defects, which appears only at certain size ratios. The second is a straight line-slip defect, which occurs at size ratios where a perfect crystal cannot form. The third is the kinked line-slip defect which incorporates fractional vacancies. This third type of defect is kinetically trapped in our experimental system.

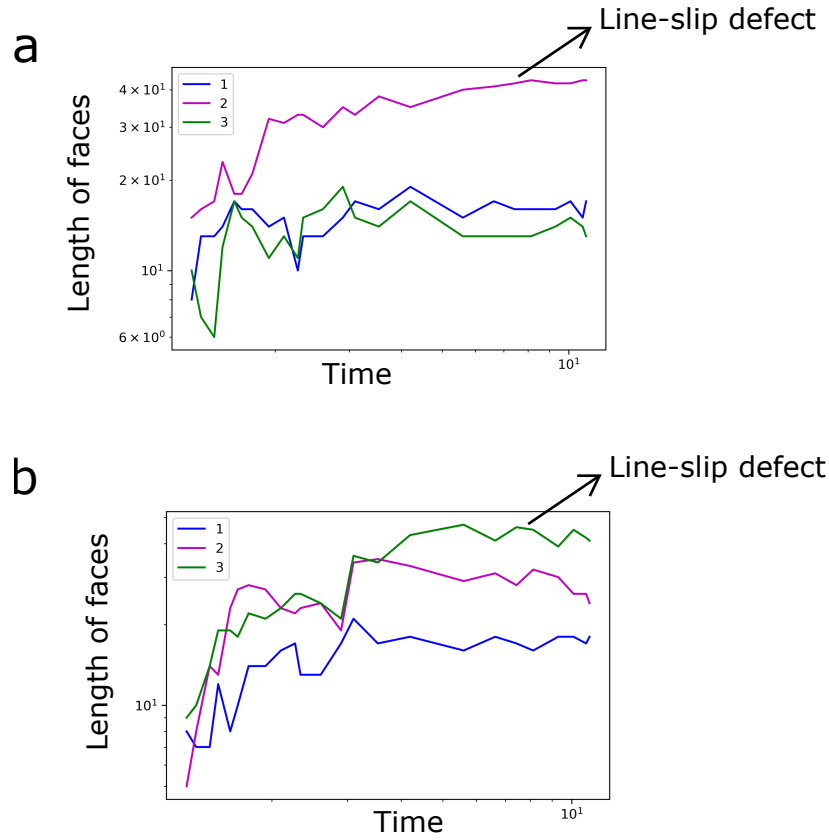


Figure 2.13: **(a)** Length of three different faces of crystal over time for the crystal in Fig. 2.12a. Face 2, which is aligned with the cylinder axis as well as the line-slip defect grows without competition from the two other faces. As a result, the line-slip defect is almost straight with negligible fractional vacancies. **(b)** Same plot as in **a**, but for the crystal in Fig. 2.12b. Here, face 3 is aligned with the line-slip defect but less aligned with the cylinder axis. It competes with face 2, which is more aligned with the cylinder axis. As a result, the line-slip defect incorporates many fractional vacancies.

These results show that a cylindrical surface frustrates the growth of a crystal that conforms to it. Previous work on colloidal crystals grown on spherical surfaces has shown that Gaussian curvature is the source of the frustration [18]. But on the cylinder, which has no Gaussian curvature, the observation of kinetically trapped

defect structures shows that a closure constraint alone can frustrate growth, similar to the ‘closure catastrophe’ identified on the sphere [28]. We have shown that the mechanism of the frustration is the anisotropy of the crystal growth dynamics.

This interplay between growth dynamics and morphology can be useful in understanding how different tubular structures form. For example, capsid proteins coat RNA strands to give rise to uniform cylindrical structures in viruses such as Tobacco Mosaic Virus (TMV) and bacteriophage T4 [9, 35]. These defectless structures must have a mechanism to avoid the frustration induced by closure. Some other tubular structures such as cytoplasmic microtubules can assemble in a cylinder with a seam line [36, 37]. How different self-assembled structures in nature respond to frustration remains an interesting question. Other relevant examples of cylindrical self-assembly include assembly of viral coat proteins on metal nanorod templates [38], closure of peptide nanotubes [39], transformation of graphene sheets to nanotubes [40], and formation of crystalline bacterial S-layers [41].

Spontaneously assembled chiral crystals and chiral defects may provide a path to design chiral materials. Artificially designed chirality has applications in sensing and motion detection at molecular lengthscales [42, 43, 44, 45], polarization modulation [46, 47, 48, 49], and optical and mechanical metamaterials [50, 51].

Our results draw a connection between crystal growth anisotropy and the shape of a line-slip defect. It may be possible to design the shape of the line-slip defect in a more predictable manner by tuning the strength of the depletion interaction as well as the cylinder diameter. Another interesting question is at which stage of crystal growth the anisotropy emerges. We often find that the growth difference between faces of a

crystal grain emerges even before the crystal meets its own boundary. Finally, the kinked line-slips are a new class of defects that have not been observed before. Their near-equilibrium dynamics, melting behavior, interaction with other defects such as vacancies and grain boundaries, and influence on mechanical properties of a tubular structure are all worth future investigation.

2.8 Materials and methods

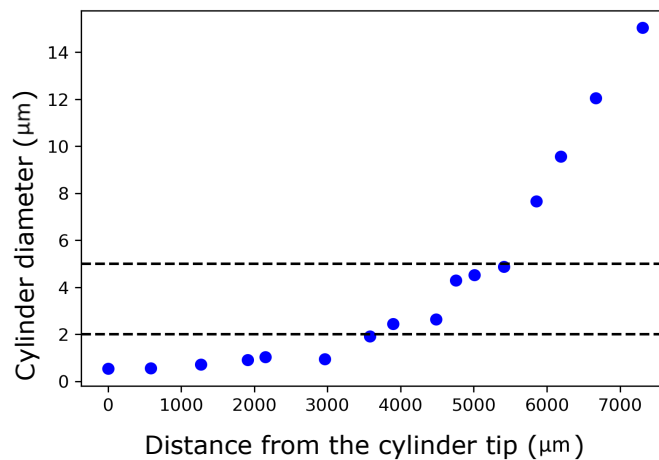


Figure 2.14: Cylinder diameter as a function of distance from the cylinder tip. The black dotted line indicates the diameter range used in experiment.

2.8.1 Fabrication of cylinders

We purchase silica optical fibers from Newport Corporation (part number F-SMF-28) and taper them down to fabricate thin cylinders. To prepare the fiber, we strip the outer layer using a fiber optic stripper (Thorlabs T06S13) to expose the cladding layer.

Then we clean the cladding by wiping it with isopropanol (VWR chemicals, 99.5%). We attach the two ends of the fiber to two motorized stages (Stepping motor controller supplied by SURUGA SEIKI, Part number D220) and place a hydrogen/oxygen type 3H torch at the center of the fiber. Pulling the fiber using the motorized stages while the burner applies heat thins the cylinder gradually until it eventually breaks. The tip of the fiber usually has a diameter of 200 nm to 500 nm. Since the diameter of the cladding layer is 125 μm , we can achieve a broad diameter range of 0.2 μm to 125 μm .

To estimate the taper rate, we measure the cylinder diameter at different points along its length from images taken with a scanning electron microscope (SEM). Fig. 2.14 shows the cylinder diameter as a function of the distance from the tip of the cylinder. The region of the cylinder we use in the experiment has a diameter between 1.5 μm to 5.5 μm . By performing a linear fit around that region (see plot in Fig. 2.14), we find that the diameter changes by about 0.18 μm over a length of 100 μm .

2.8.2 Preparation of colloidal suspension

We purchase colloidal polystyrene microspheres with an average diameter of 710 nm from Microgenics corporation (Thermo Scientific Fluoro-Max R700). We wash 100 μl of 1 % w/v particles five times by centrifuging at 8100 g , removing the supernatant, and re-dispersing in deionized water (resistivity 18.2 $\text{M}\Omega\text{cm}$, obtained from a Millipore Milli-Q Synthesis system). We adjust the particle concentration in the final colloidal suspension to be about 0.5 % w/v.

We mix the colloidal particles with sodium dodecyl sulfate (SDS, Sigma-Aldrich, > 99%) with deionized water to make an SDS micellar solution, which gives rise to

the depletion interaction between the colloidal particles and between the particles and the cylinder. To prepare the final suspension, we mix 20 μl of 0.5 % w/v colloidal suspension with 20 μl of SDS solution at 67.6 mM to achieve a particle concentration of 0.25 % w/v and SDS concentration of 33.8 mM. We find that a crystalline monolayer successfully forms on the cylinder surface when the SDS concentration is between 33.6 mM and 34 mM.

2.8.3 Preparation of roughened glass coverslips

We use two flat glass coverslips to make our sample chamber, which contains the colloidal suspension and a cylinder (Fig. 2.15). Because the depletion force scales linearly with the overlap of excluded volume, the depletion attraction between a spherical colloidal particle and the flat glass surface is more than twice as strong as the attraction between a colloidal particle and the cylinder. As a result, particles tend to crystallize on the coverslips instead of the cylinder. To avoid this effect, we coat the coverslips with a monolayer of smaller colloidal particles (average diameter 300 nm, Life Technologies S37492). The resulting roughness reduces the attraction between the coverslips and the colloidal particles, as evidenced by the fact that the particles (diameter 710 nm) crystallize only on the surface of the cylinder and not on the coverslips.

To attach the smaller colloidal particles to the coverslips, we first wash the 300-nm polystyrene nanoparticles three times by centrifuging at 12000*g*, removing the supernatant, and redispersing in ethanol (Koptec, 190 proof). We adjust the final concentration of the particle suspension to be 4.0 % w/v. We treat the glass coverslips

for 3 min with oxygen plasma in a Harrick PDC-32G plasma cleaner at high RF settings. The plasma treatment and the dispersion in ethanol help the colloidal suspension wet the coverslips. We spin-coat a droplet of particle suspension (volume from 50 μl to 100 μl , depending on the surface area of the coverslip to be covered) onto the coverslip in two steps, using a spin-coater (Headway PWM32): first at 1000 rpm for 5 s, then at 2500 rpm for 30 s. After spin-coating, we bake the treated coverslips at 52 $^{\circ}\text{C}$ for about 30 min to ensure good adhesion between the particles and the glass surface.

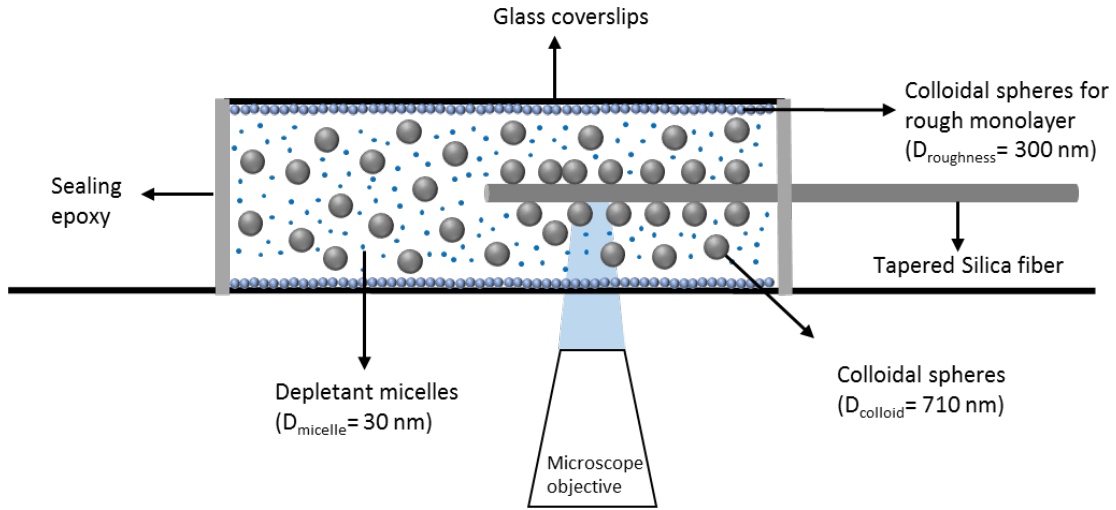


Figure 2.15: Sample chamber setup on a microscope stage. Only the colloidal spheres (diameter 710 nm) are fluorescently dyed (Firefli Fluorescent Red 542/612 nm). We use a confocal microscope to observe them forming crystals on the cylinder.

2.8.4 Setup and imaging of sample chamber

To prepare a sample chamber, we place a tapered optical fiber that has been plasma-treated for 5 min between two roughened coverslips, as shown in Fig. 2.15.

The plasma treatment reduces irreversible binding between the particles and the glass cylinder, both of which are negatively charged. The bottom coverslip is 24×60 mm and the top is 22×22 mm (VWR, no. 1). We place two thin strips of plastic film (Dupont Teijin film Mylar A 300 gauge) with a thickness of $67 \mu\text{m}$ between the coverslips to control the thickness of the sample chamber. We draw a thin line of vacuum grease (Dow Corning) on top of the bottom cover slip in the shape of a square with one open side. The part of the fiber where colloidal particles crystallize is contained within the square. We use binder clips to make a coverslip sandwich with the fiber, plastic film spacers, and vacuum grease inside. We then apply UV-curable epoxy (Norland Products, NOA-85) to all three sides of the sample chamber as a secondary seal. Finally, we inject the mixture of colloidal particles with SDS solution into the chamber from the open side of the chamber and seal it using a 5-minute epoxy (Devcon). It is important to have a completely sealed sample chamber because a leak in the seal over time causes evaporation of the colloidal solution, which may disrupt the self-assembly of colloidal particles.

We use a confocal microscope (Leica DMI6000) and a water immersion objective ($63\times$, NA 1.2) to image the system. Crystals form and cover the surface of the cylinder within 2 h to 5 h of sample preparation. After a crystalline grain wraps around the cylinder, the typical length of the grain along the cylinder is $15 \mu\text{m}$ to $20 \mu\text{m}$. Within a typical grain, the diameter of the fiber changes about $0.036 \mu\text{m}$ owing to the taper, which is close to the standard deviation in the particle size ($0.021 \mu\text{m}$, as estimated from the reported 3 % polydispersity). Therefore, the diameter of the fiber changes insignificantly on the scale of a crystalline grain, and treating the tapered fiber as a

cylinder is a good approximation.

2.9 Calculation of equilibrium length of line-slip defect

2.9.1 Model

As described in the main text, to calculate the equilibrium length of a line-slip defect, we generate all possible configurations of a kinked line-slip defect with path length L and calculate the equilibrium length l_{eq} using Boltzmann statistics. A line-slip defect in its ground state is straight, as shown in Fig. 2.16a. We define a starting point of this line slip \mathbf{v}_i and a terminating point \mathbf{v}_f . Then we find all the possible paths between \mathbf{v}_i and \mathbf{v}_f , and we repeat for all the possible \mathbf{v}_f .

The vector $\mathbf{v}_f - \mathbf{v}_i$ can be expressed as one or more linear combinations of the unit vectors \mathbf{v}_1 , \mathbf{v}_2 , and \mathbf{v}_3 (Fig. 2.16a), which are defined for a 2D hexagonal lattice. We consider a Cartesian coordinate system where the x -axis is aligned with the line-slip defect. The vector \mathbf{v}_1 is aligned with the x -axis as well as the line-slip direction, and \mathbf{v}_2 and \mathbf{v}_3 are aligned at $\mp 60^\circ$ with respect to \mathbf{v}_1 :

$$\mathbf{v}_1 = \begin{bmatrix} 1 \\ 0 \end{bmatrix}. \quad (2.1)$$

$$\mathbf{v}_2 = \text{rot}(-60^\circ) \cdot \mathbf{v}_1 = \begin{bmatrix} \cos(60^\circ) & -\sin(-60^\circ) \\ \sin(-60^\circ) & \cos(60^\circ) \end{bmatrix} \begin{bmatrix} 1 \\ 0 \end{bmatrix} = \begin{bmatrix} \frac{1}{2} \\ -\frac{\sqrt{3}}{2} \end{bmatrix}. \quad (2.2)$$

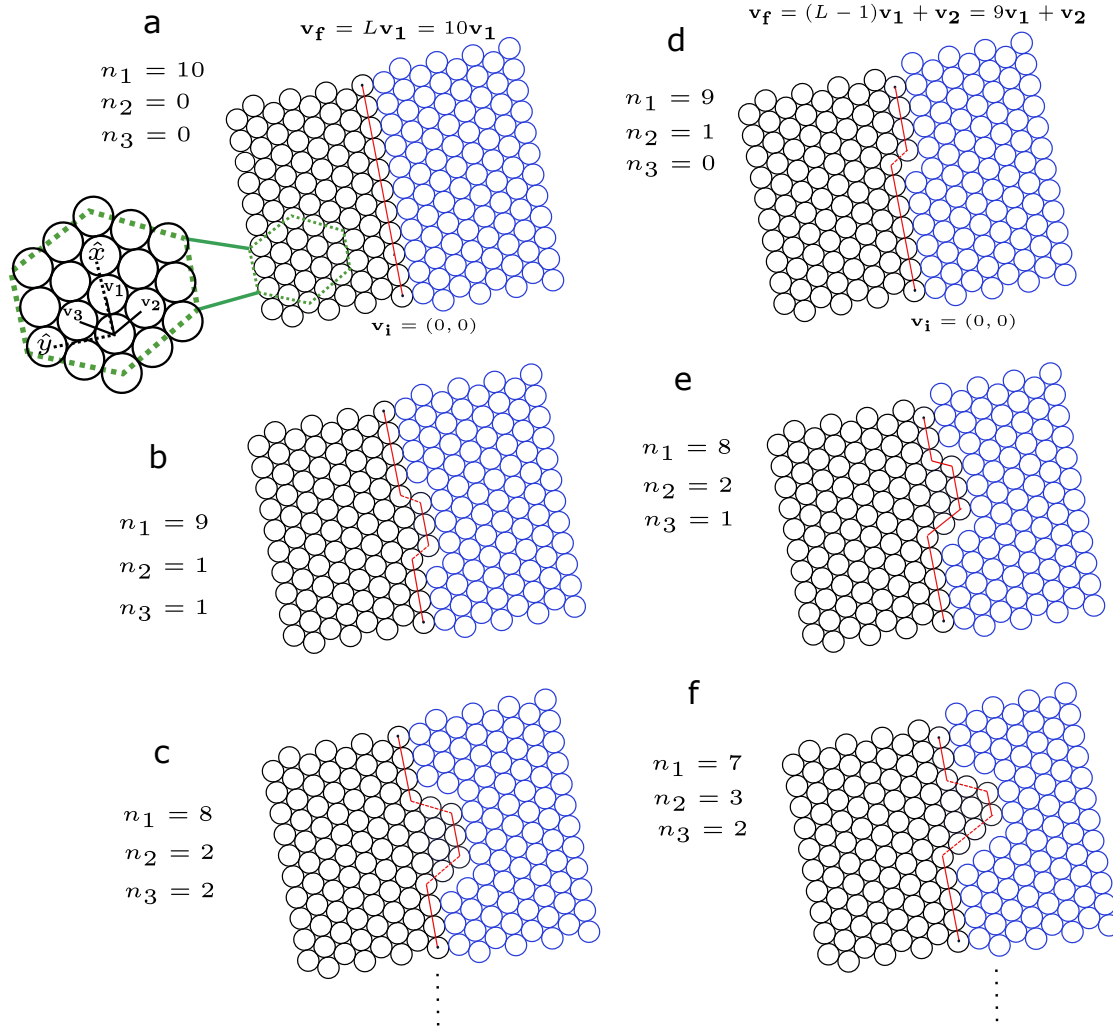


Figure 2.16: **(a)** Ground state configuration of a line-slip defect with length $L = 10$. The starting point of the defect is \mathbf{v}_i and the ending point is \mathbf{v}_f . **(b)** One excited state with the same \mathbf{v}_i and \mathbf{v}_f as in (a). **(c)** Another excited state with the same \mathbf{v}_i and \mathbf{v}_f as in (a), (b). All of the excited states can be calculated from the possible configurations of n_1 , n_2 , and n_3 . **(d)**, **(e)**, **(f)** Excited states of the line-slip defect that ends at a different \mathbf{v}_f . The values for n_1 , n_2 , and n_3 are different from those in (a), (b), and (c).

$$\mathbf{v}_3 = \text{rot}(60^\circ) \cdot \mathbf{v}_1 = \begin{bmatrix} \cos(60^\circ) & -\sin(60^\circ) \\ \sin(60^\circ) & \cos(60^\circ) \end{bmatrix} \begin{bmatrix} 1 \\ 0 \end{bmatrix} = \begin{bmatrix} \frac{1}{2} \\ \frac{\sqrt{3}}{2} \end{bmatrix}. \quad (2.3)$$

We set the starting point of the line-slip to $\mathbf{v}_i = [0, 0]^\top$. The end point $\mathbf{v}_f = [x_f, y_f]^\top$ can vary, depending on the number of kinks. The set of all possibilities for \mathbf{v}_f is

$$\mathbf{v}_f = \begin{bmatrix} x_f \\ y_f \end{bmatrix} \in \{L\mathbf{v}_1, (L-1)\mathbf{v}_1 \pm \mathbf{v}_2, (L-2)\mathbf{v}_1 \pm 2\mathbf{v}_2, \dots, \pm L\mathbf{v}_2\}. \quad (2.4)$$

For each \mathbf{v}_f , we solve the following equation for n_1 , n_2 , and n_3 to find all possible line-slip paths:

$$\begin{bmatrix} \mathbf{v}_1 & \mathbf{v}_2 & \mathbf{v}_3 \end{bmatrix} \begin{bmatrix} n_1 \\ n_2 \\ n_3 \end{bmatrix} = \begin{bmatrix} x_f \\ y_f \end{bmatrix}. \quad (2.5)$$

For each solution i , we calculate the line-slip length l_i and energy ΔE_i (note that the path length $L = n_1 + n_2$ is constant for all the paths). For any solution, the line-slip length $l_i = n_{1,i}$, since \mathbf{v}_1 is aligned with the line-slip orientation. We estimate ΔE_i from the number of broken “bonds,” or depletion interactions, across the line slip. In a line slip without kinks, each particle interacts with one other particle across the line slip. Therefore the maximum number of bonds across the line-slip is L , while the actual number of bonds is $n_{1,i}$. The energy of the kinked line slip relative to the ground state is then $\Delta E_i = (L - n_{1,i})E_b$, where E_b is the well depth of the interparticle attraction. We can then calculate l_{eq} as the equilibrium expectation value over all N paths:

$$l_{\text{eq}} = \frac{\sum_{i=1}^N l_i e^{-\Delta E_i/k_B T}}{\sum_{i=1}^N e^{-\Delta E_i/k_B T}}. \quad (2.6)$$

Here, i corresponds to a solution of equations 2.4 and 2.5. The total number of possible solutions for a given L is N , where

$$N = N_{L\mathbf{v}_1} + 2N_{(L-1)\mathbf{v}_1 + \mathbf{v}_2} + \dots + 2N_{L\mathbf{v}_2}, \quad (2.7)$$

where $N_{L\mathbf{v}_1}$ is the number of paths for $\mathbf{v}_f = L\mathbf{v}_1$, $N_{(L-1)\mathbf{v}_1+\mathbf{v}_2}$ is the number of paths for $\mathbf{v}_f = (L-1)\mathbf{v}_1 + \mathbf{v}_2$, and so on. $N_{L\mathbf{v}_2}$ is the number of paths for $\mathbf{v}_f = L\mathbf{v}_2$. The coefficients of 2 in (2.7) arise because each kinked geometry has a mirror image with respect to the line slip (Fig. 2.17a,b).

For a given N_i (for example, $N_i = N_{L\mathbf{v}_1}$), we find all solutions sets (n_1, n_2, n_3) . For each solution, we calculate the number of configurations $N_{(n_1, n_2, n_3)}$ from the following equation:

$$N_{(n_1, n_2, n_3)} = \frac{(n_1 + n_2 + n_3)!}{n_1! n_2! n_3!} \quad (2.8)$$

In this model, we assume that the cylinder circumference is larger than the line-slip length L . When the circumference is smaller than L , the crystal loops back on itself before reaching $\mathbf{v}_f = L\mathbf{v}_2$. As a result, the higher-order configurations near $\mathbf{v}_f = L\mathbf{v}_2$ do not contribute to the equilibrium line-slip length, and the value of l_{eq} increases. Therefore, by including all configurations up to $\mathbf{v}_f = L\mathbf{v}_2$, we calculate the lower bound of l_{eq} . Because our experimental values l are smaller than the lower bound of l_{eq} , the assumption about the circumference does not change the conclusion that the kinked defects are out of equilibrium.

2.9.2 Example of calculating configurations

To show how the model accounts for the possible geometries of the kinked line slip, consider an example of a defect with $L = 10$. Fig. 2.16a–c shows a number of different paths that start at $\mathbf{v}_i = [0, 0]^T$ and end at $\mathbf{v}_f = 10\mathbf{v}_1$. When these ends are fixed, all paths can be determined by solving equation (2.5) for n_1 , n_2 , and n_3 after

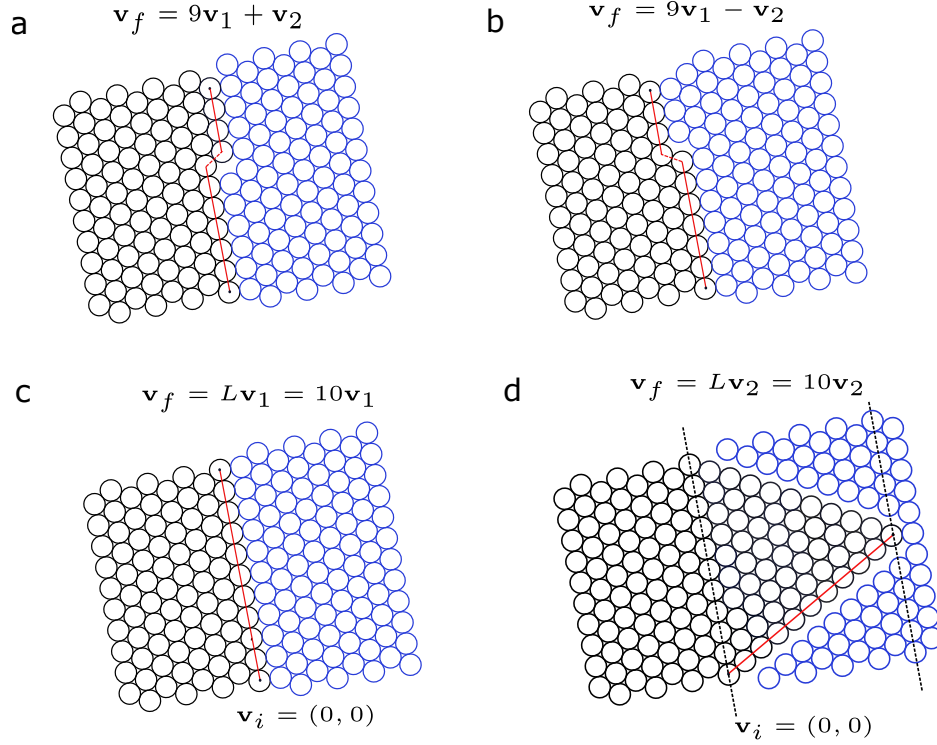


Figure 2.17: **(a)** One excited state configuration for $\mathbf{v}_f = 9\mathbf{v}_1 + \mathbf{v}_2$. **(b)** The same excited state configuration for $\mathbf{v}_f = 9\mathbf{v}_1 - \mathbf{v}_2$. This is a mirror image of the one in (a). Since the number of configurations in this mirror setup is exactly the same, we calculate only the number of configurations for $\mathbf{v}_f = 9\mathbf{v}_1 + \mathbf{v}_2$ and multiply this by 2. **(c)** Image of the configuration for the first $\mathbf{v}_f = 10\mathbf{v}_1$. This is also the ground state. **(d)** Image of the configuration for the final $\mathbf{v}_f = 10\mathbf{v}_2$. In this configuration, the line-slip is full of fractional vacancies. This is the maximum \mathbf{v}_f that is relevant. If the cylinder circumference (indicated by the dotted black parallel lines) is larger than the line-slip length L , we must consider all values of \mathbf{v}_f starting from the one in (c) and ending in the one in (d).

substituting the values of \mathbf{v}_i and \mathbf{v}_f :

$$n_1 \begin{bmatrix} 1 \\ 0 \end{bmatrix} + n_2 \begin{bmatrix} \frac{1}{2} \\ \frac{-\sqrt{3}}{2} \end{bmatrix} + n_3 \begin{bmatrix} \frac{1}{2} \\ \frac{\sqrt{3}}{2} \end{bmatrix} = \begin{bmatrix} 10 \\ 0 \end{bmatrix}, \quad (2.9)$$

subject to the constraints

$$n_1 + n_2 = 10, \quad (2.10)$$

and

$$n_2 = n_3. \quad (2.11)$$

We consider n_1 , n_2 , and n_3 to be positive integers only, because negative values create a detour to the end point \mathbf{v}_f . These detours have high energy and therefore we expect their contribution to l_{eq} to be negligible.

To enumerate the possible solutions, we use a Python script that loops over n_3 from $n_3 = 0$ to $n_3 = 10$ and calculates the corresponding values of n_1 and n_2 using equations (2.10) and (2.11). The solutions are

$$(n_1, n_2, n_3) = (10, 0, 0), (9, 1, 1), (8, 2, 2), \dots, (0, 10, 10). \quad (2.12)$$

We show the shapes of the line-slips for the first three solutions in Fig. 2.16a,b,c. For the first solution $(n_1, n_2, n_3) = (10, 0, 0)$, shown in Fig. 2.16a, the path consists of ten \mathbf{v}_1 vectors only. In this case, there is only one possible configuration: $N_{(10,0,0)} = 1$.

The second solution $(n_1, n_2, n_3) = (9, 1, 1)$ is shown in Fig. 2.16b. The path here consists of nine \mathbf{v}_1 vectors, one \mathbf{v}_2 vector, and one \mathbf{v}_3 vector. The number of possible configurations is

$$N_{(9,1,1)} = \frac{(n_1 + n_2 + n_3)!}{n_1!n_2!n_3!} = \frac{11!}{9!1!1!} = 110. \quad (2.13)$$

We then use the Python script to calculate $N_{\mathbf{v}_1}$ for all the other solutions in equation (2.12).

$$N_{\mathbf{v}_1} = N_{(10,0,0)} + N_{(9,1,1)} + \dots + N_{(0,10,10)} \quad (2.14)$$

We next calculate the configurations for a different end point. Fig. 2.16d–f shows paths for $\mathbf{v}_i = [0, 0]^\top$ and $\mathbf{v}_f = 9\mathbf{v}_1 + \mathbf{v}_2$. Substituting into equation (2.5), we get

$$n_1 \begin{bmatrix} 1 \\ 0 \end{bmatrix} + n_2 \begin{bmatrix} \frac{1}{2} \\ \frac{-\sqrt{3}}{2} \end{bmatrix} + n_3 \begin{bmatrix} \frac{1}{2} \\ \frac{\sqrt{3}}{2} \end{bmatrix} = (L - 1) \begin{bmatrix} 1 \\ 0 \end{bmatrix} + \begin{bmatrix} \frac{1}{2} \\ \frac{-\sqrt{3}}{2} \end{bmatrix}, \quad (2.15)$$

now subject to the constraints

$$n_1 + n_2 = 10, \quad (2.16)$$

and

$$n_3 = n_2 - 1. \quad (2.17)$$

Now the possible solutions are

$$(n_1, n_2, n_3) = (9, 1, 0), (8, 2, 1), (7, 3, 2), \dots, (0, 10, 9). \quad (2.18)$$

From this solution, we repeat the previous steps and calculate all the different configurations $N_{9\mathbf{v}_1+\mathbf{v}_2}$ as well. We then shift the terminating point and repeat until $\mathbf{v}_f = 10\mathbf{v}_2$ in which case no line-slip defect exists (Fig. 2.17d) and, as a result, l becomes zero.

2.9.3 Estimation of bond energy E_b

One way to estimate the depth of interaction potential is to measure the average lifetime of a dimer (a cluster of two particles) and use an Arrhenius equation to extract the energy barrier [52]:

$$\tau = \tau_D e^{U/k_B T}, \quad (2.19)$$

where τ is the measured lifetime of a dimer, U is the depth of the potential, and $\tau_D = w^2/D$ is the timescale for the particles to diffuse a distance equal to the range of the potential w given a diffusion coefficient D .

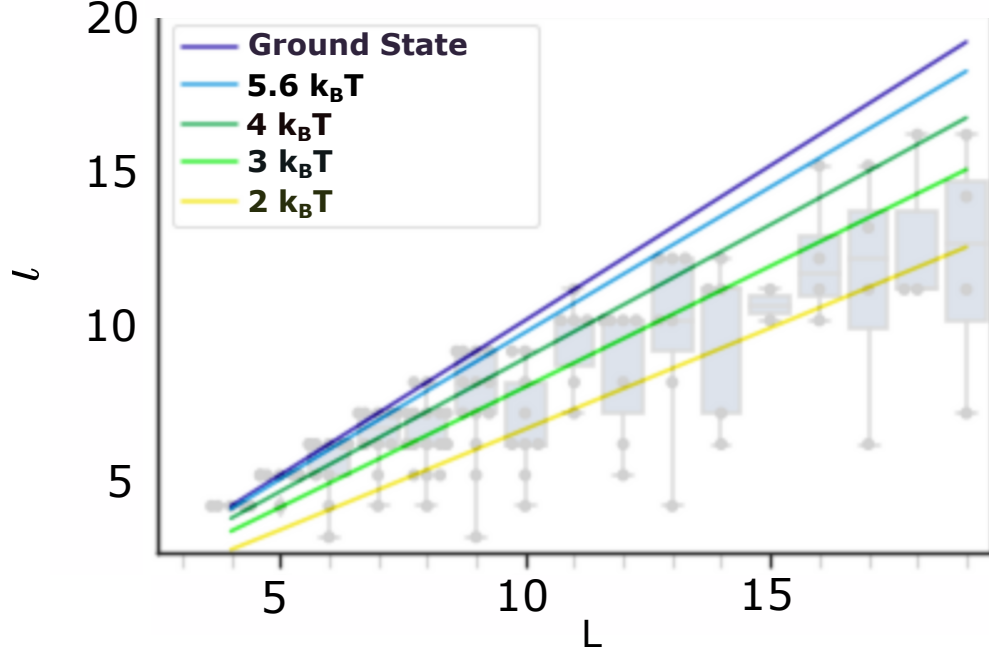


Figure 2.18: Equilibrium line-slip length l_{eq} as a function of total line-slip length L for different values of the potential well depth.

We measure τ and D from a movie of the early stages of crystal growth on a cylinder. We find that the value of τ varies from 0.52 s to 4.64 s. We measure the diffusion constant using the Python package Trackpy for particle tracking (<https://github.com/soft-matter/trackpy>). Our measured value of the diffusion constant D is $(0.188 \pm 0.035) \mu\text{m}^2/\text{s}$. From these values, we estimate the depth of interaction potential to be $4\text{--}7k_B T$.

In this estimate, we assume that D is a constant equal to the single-particle diffusion coefficient on the cylinder surface. However, D may vary with the interparticle distance and should in general be smaller than the single-particle value because of hydrodynamic interactions. Therefore the U we calculate is likely an overestimate.

In Fig. 2.18, we plot l_{eq} and the total line-slip length L for different values of the potential well depth. We find agreement between our calculated l_{eq} and the measured values only when if the potential well depth is $2k_B T$, which is significantly lower than our estimate and likely too low to lead to stable crystals [18].

2.10 Supplementary results

2.10.1 Relaxation of a line-slip-like defect on flat surface

As shown in Fig. 2.19, defects with a form similar to that of a line-slip defect can appear in flat crystals. However, it is possible for them to relax by shear within a short time.

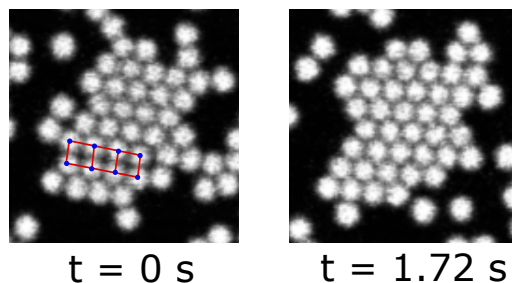


Figure 2.19: A line-slip like defect found in a small crystalline grain on a flat 2D surface. It relaxes in a short time because the grain is free to translate and rotate.

2.10.2 Closure of a crystal without any line-slip defect

We observe the closure of a crystal that does not have a line-slip defect. As shown in Fig. 2.20, in the absence of a line-slip defect, the crystal can close perfectly without

becoming kinetically trapped.

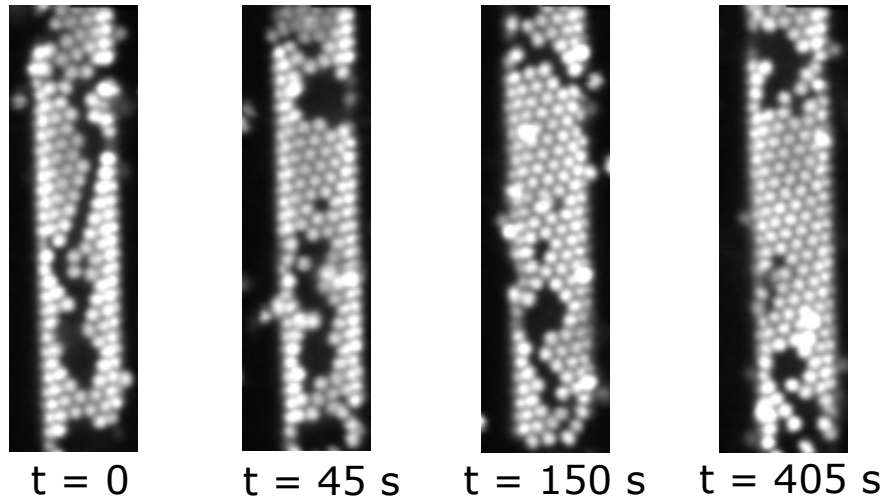


Figure 2.20: Closure of a crystal without any line-slip defect. The grain closes within a few minutes and does not get kinetically trapped.

2.10.3 Long time dynamics of kinked line-slip defects

We observe the dynamics of kinked line-slip defect over about 2 h. In Fig. 2.21, we show one kinked line-slip defect with only one fractional vacancy. According to our definition of the line-slip length l , in this case $l = L - 1$ and $n_2 = 1$. Although in equilibrium, it is possible that one fractional vacancy can form or disappear owing to thermal fluctuations, we find that the fractional vacancy in the line-slip in Fig. 2.21 does not disappear in the observed timescale. Instead, it moves back and forth from one position to another (Fig. 2.21a–c), keeping the the total number of bonds constant. The only way for this line-slip to reach its ground state is for the fractional vacancy to translate along the line-slip until it reaches the grain boundary and exists the crystal.

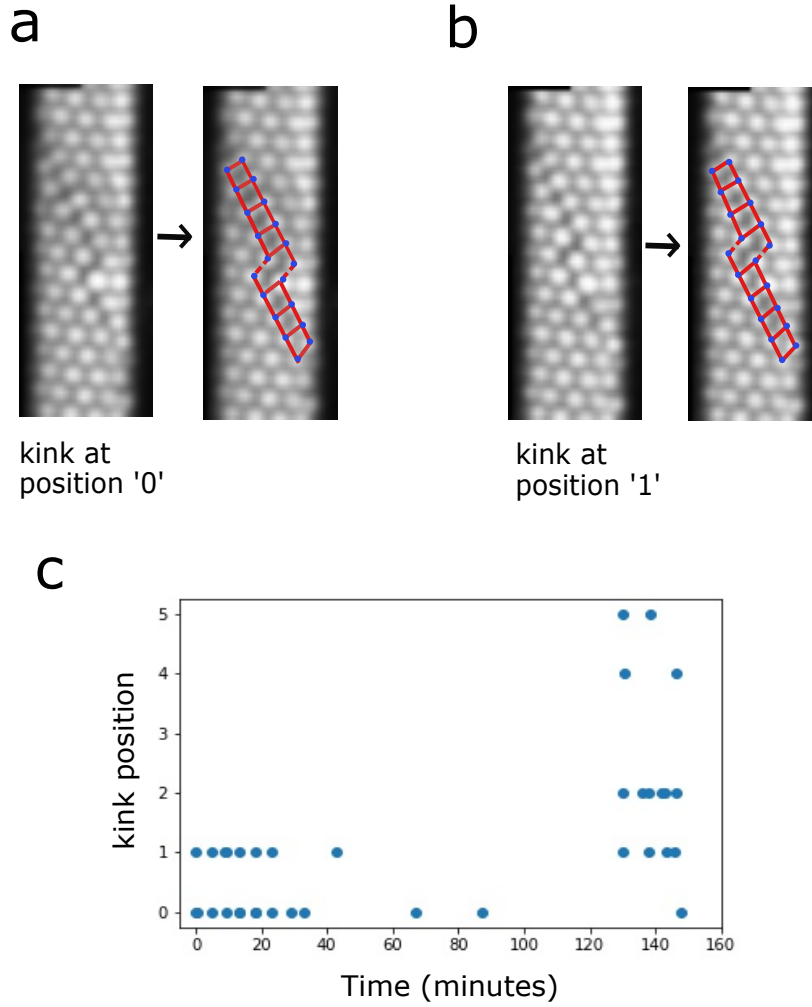


Figure 2.21: Dynamics of a kinked line-slip defect with one fractional vacancy. **(a)** Confocal microscope image of the kinked line-slip defect when the fractional vacancy is at position 0. **(b)** Confocal microscope image of the kinked line-slip defect when the fractional vacancy is at position 1. **(c)** Position of the kink identified from the confocal images over about 150 min. The kink mostly moves back and forth between positions 0 and 1, but it also jumps to positions 2, 4, and 5 later. However, the number of bonds stays the same throughout.

However, given the timescale of one fractional vacancy moving back and forth as measured in Fig. 2.21c, it may take a very long time for the vacancy to diffuse out of

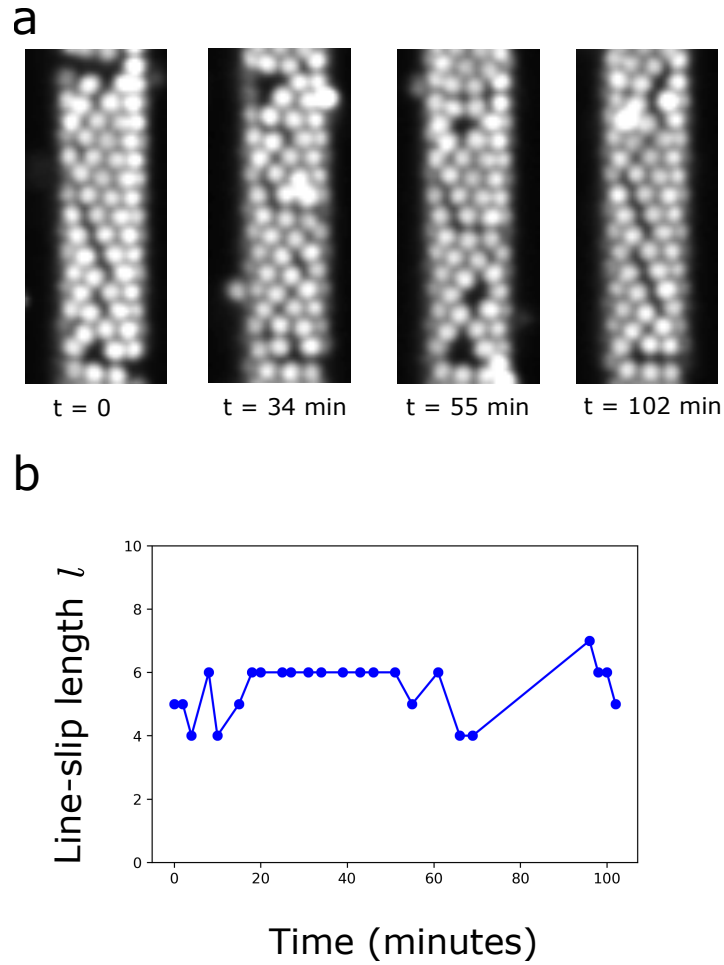


Figure 2.22: Dynamics of a kinked line-slip defect with many fractional vacancies. **(a)** Confocal microscope image of the kinked line-slip defect at different points in time. **(b)** Line-slip length l for the defect as a function of time. l fluctuates, but does not decrease significantly or reach its ground state value.

the crystal. This result indicates that kinked line-slip defects with a relatively small number of fractional vacancies can be kinetically trapped if the fractional vacancies are far from a crystal boundary.

We observe the dynamics of another kinked line-slip defect with a higher number of fractional vacancies over about 100 min (Fig. 2.22). This line-slip starts with $l = 5$,

$n_2 = 7$, and $L = 12$. Over time, the line-slip length l shows small fluctuations and does not significantly decrease, indicating that kinked line-slip defects with a higher number of fractional vacancies are kinetically trapped.

2.10.4 Particle motion at the kinks

The kinked line-slip defects exhibit small fluctuations in line-slip length over a long period of time. To understand the nature of these fluctuations, we quantify the motion of the particles adjacent to the kinks on a kinked line-slip defect. Using Trackpy, we identify the locations of eight particles (Fig. 2.23a) at each frame of the movie and calculate their displacements. We track two sets of particles; the red particles that make bonds with 4 nearest neighbors and the black particles that make bonds with 5 nearest neighbors (Fig. 2.23a). As plotted in Fig. 2.23b, we find that the red particles are more mobile compared to the black particles. Their maximum displacement is close to $0.35\text{ }\mu\text{m}$, which is less than a particle diameter. This result makes sense because the space available for fractional vacancies at the kinks should be less than a particle diameter. Although most black particles are immobile, one black particle has a huge displacement at around 25s, which is related to the motion of the neighboring red particle.

From these results we see that motion at the kinks is not uniform – particles adjacent to the fractional vacancies (which usually have 4 neighbors) are more mobile compared to the particles adjacent to the line slip (which usually have 5 neighbors). The less mobile particles restrict the diffusion of the fractional vacancies along the line-slip.

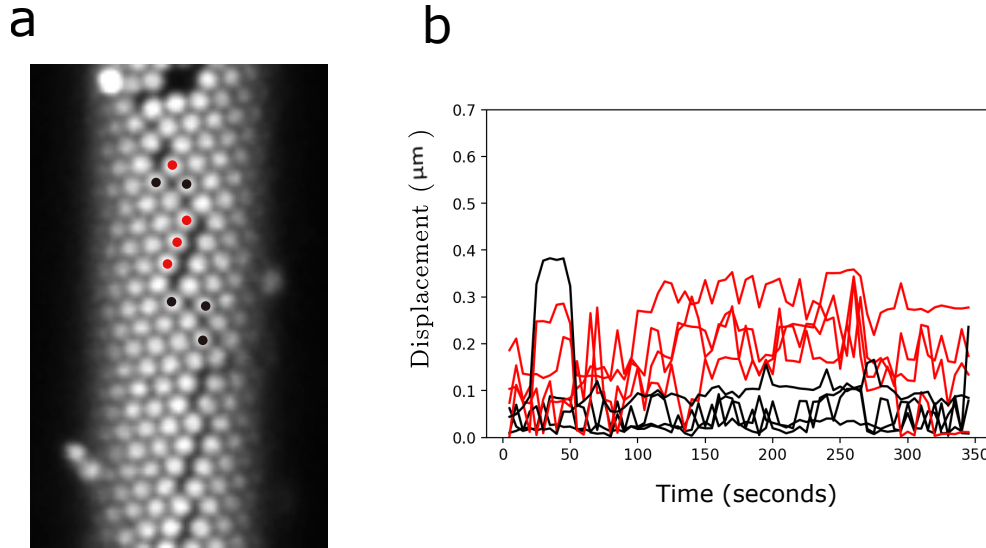


Figure 2.23: (a) Confocal microscope image of a kinked line-slip defect. Particles are color-coded based on the number of bonds. The red particles make bonds with 4 nearest neighbors and the black particles make bonds with 5 nearest neighbors. (b) Displacement of each red and each black particle in (a) as a function of time.

2.10.5 Interaction of line-slip defect with other defects

We observe the processes in which a line-slip defect in a small crystal can interact with the crystal boundary and vacancies. In the kinked line-slip shown in Fig. 2.24a, the fractional vacancy eventually exits the crystal boundary (Fig. 2.24b) and the line-slip reaches the ground state. Following a similar process, a kink can enter through the boundary resulting in a fractional vacancy in the line-slip.

We find that line-slip defects can interact with full vacancies too. The line-slip defect shown in Fig. 2.24c has a vacancy in it. Over time, part of the full vacancy diffuses out of the crystal boundary leaving a fractional vacancy as well as a kink in the line-slip (Fig. 2.24d).

We observe both of these interactions in a small crystalline grain and on a short timescale. For larger grains as shown in Fig. 2.21 and Fig. 2.22, these interactions happen locally and do not significantly change the structure of the line-slip defect. However, they may play an important role during the growth of the crystals in determining the local shape of the line-slip defect with kinks.

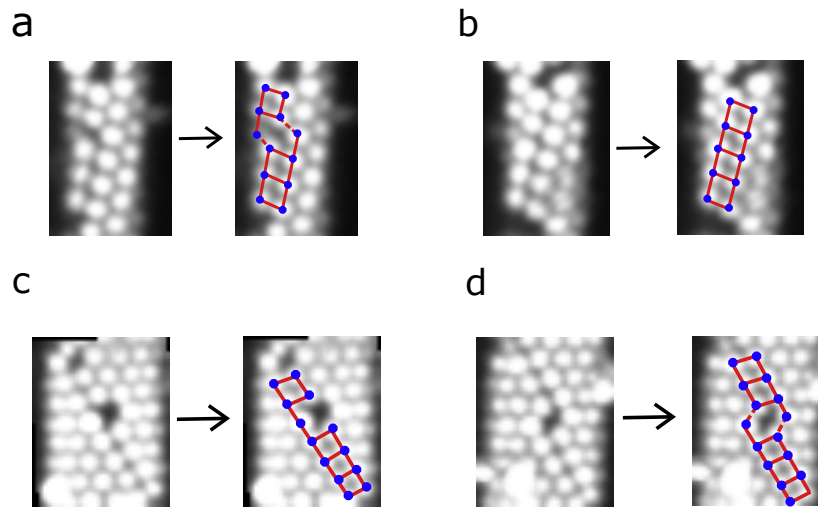


Figure 2.24: **(a)** A line-slip defect with a single fractional vacancy. **(b)** Over time, the vacancy from (a) moves out of the crystal boundary. **(c)** A line-slip defect with a full vacancy on the slip-line. **(d)** Over time, part of the vacancy moves out of the crystal boundary creating a fractional vacancy in a kinked line-slip defect.

Chapter 3

Structure of colloidal polycrystals on a cylinder

The research described in this Chapter was supported by the National Science Foundation under grant no. DMR-1420570.

3.1 Introduction

A polycrystalline material is made of multiple crystalline grains; the structure of the grains control the mechanical, optical, and electrical properties of the material [53, 54]. Polycrystals made of colloidal particles are used to study numerous microscopic phenomena, such as grain boundary fluctuations [55], grain growth in the presence of impurities [56, 57], and grain boundary sculpting [58]. However, most studies on colloidal polycrystals focus on crystals grown in bulk, ignoring the effect of their substrate geometry.

We examine the structure of colloidal polycrystals on the surface of a cylinder. A cylinder with a length much larger than its diameter imposes a closure constraint along its circumferential direction, but not along its axial direction. This anisotropic constraint is not present for a crystal formed on a flat 2D substrate with no size constraint in any direction. As we have seen in Chapter 2, in such a system, single crystals close around the circumference of the cylinder and multiple single crystals form along the length of the cylinder. In Chapter 2, we focused only on morphology and growth dynamics of each single crystal. Here, we measure the size and shape of all single crystalline grains for different cylinder-to-sphere size ratios and compare them to the values for crystalline grains formed on a flat 2D surface. These measurements not only indicate how polycrystalline structure is different on a cylindrical substrate, but also help our understanding of grain growth mechanisms and grain boundary dynamics on a cylinder.

3.2 Methods

3.2.1 Polycrystals on cylindrical substrate

We use the same experimental system demonstrated in Chapter 2. As shown in the confocal images of Fig. 3.1a, crystals with different orientations or chirality can form along the length of a cylinder. We find that the grain boundaries are mostly aligned with the circumferential axis of the cylinder. Because of this geometry, we assume the crystalline grain to have a cylindrical shape (Fig. 3.1b). Using this approximation, we calculate three geometrical parameters of each crystalline grain on a cylinder: length

L , area S , and anisotropy A .

Length L We measure length \tilde{L} (in pixels) of each grain from the confocal images and normalize it by the particle center-to-center distance d_{sp} (in pixels):

$$L = \frac{\tilde{L}}{d_{sp}}. \quad (3.1)$$

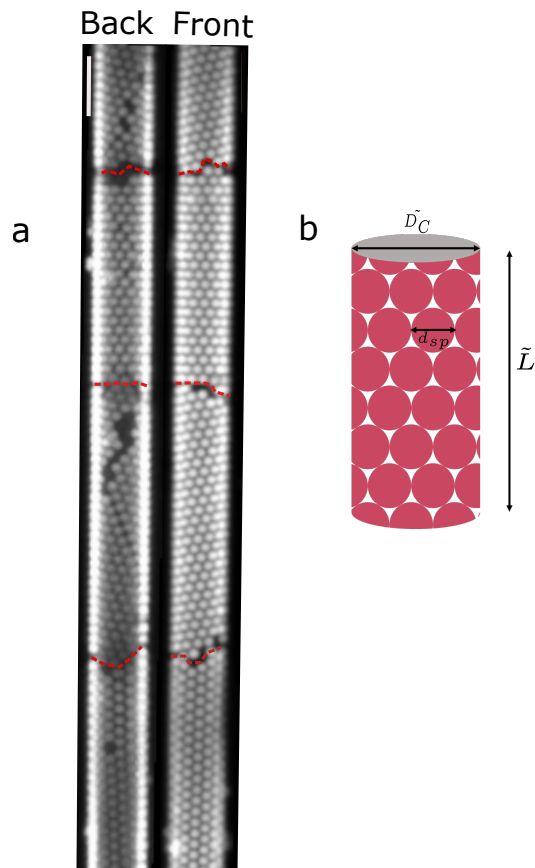


Figure 3.1: **(a)** Confocal image of polycrystals on a cylinder. The red dotted lines show the position of grain boundaries between each single crystal wrapped around the cylinder. **(b)** Model of a cylindrical crystal.

Area S We calculate the normalized area of a grain from its cylindrical approximation:

$$S = \pi D_c L, \quad (3.2)$$

where D_c is the normalized cylinder diameter:

$$D_c = \frac{\tilde{D}_c}{d_{\text{sp}}}. \quad (3.3)$$

Anisotropy A We calculate anisotropy of the crystal grain from the ratio of the crystal length to the cylinder circumference:

$$A = \frac{L}{\pi D_c}. \quad (3.4)$$

3.2.2 Polycrystals on flat 2D substrate

We calculate the average length of crystal grains using the grain intercept method [59]. On a confocal image of 2D polycrystals (Fig. 3.2a), we draw multiple straight lines in the horizontal, vertical, and diagonal directions. To calculate the grain length L , we measure the length of each line \tilde{L} , normalize it by the particle center-to-center distance d_{sp} , then divide it by the number of grain boundaries N_{gb} that we find along the line. We repeat this process for all lines (all 9 lines drawn on Fig. 3.2a) to calculate L for each line, and then take the mean from those nine values to calculate an average L_{av} for that image.

$$L = \frac{L_{\text{line}}}{N_{\text{gb}}}, \quad (3.5)$$

where

$$L_{\text{line}} = \frac{\tilde{L}}{d_{\text{sp}}}. \quad (3.6)$$

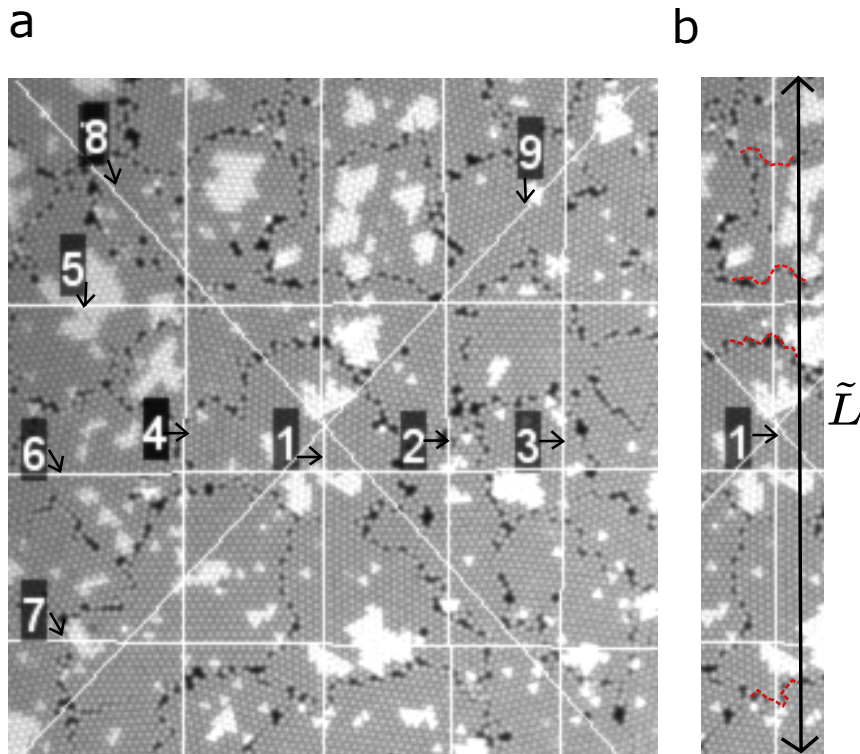


Figure 3.2: **(a)** Confocal image of polycrystals on a flat 2D surface. To calculate the average grain length, we draw 9 straight lines at different angles throughout the image. **(b)** Line 1 and its surroundings. We find four grain boundaries shown by the red dotted lines. Therefore, $N_{\text{gb}} = 4$. We repeat this procedure to find values of N_{gb} for all nine lines in **(a)**.

3.3 Results

3.3.1 Length L

We find that the grain length L increases very slowly with cylinder-to-sphere size ratio D_C . As shown by the linear fit in Fig. 3.3, the average grain length L on a cylinder approaches the average grain length on a flat 2D surface for $D_C \approx 3.0$. However, for $D_C \lesssim 3.0$, we find quite a few grains with $L < L_{\text{av}}$.

To calculate L_{av} for a flat 2D surface, we measure L_{av} from four different confocal

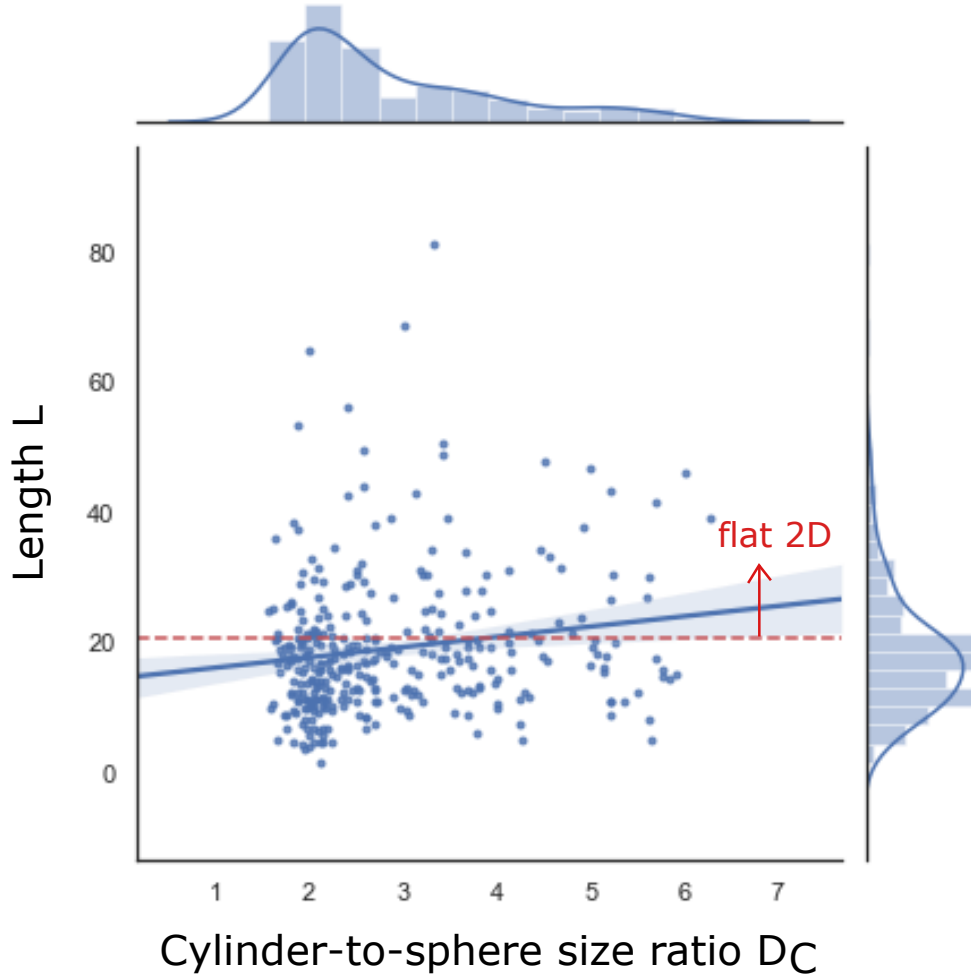


Figure 3.3: Grain length L measured for various cylinder-to-sphere size ratios D_C . Each blue point corresponds to one crystalline grain on a cylinder. The blue solid line represents a linear fit while the shaded region around it shows the span of one standard deviation. The red horizontal line shows L_{av} on a flat 2D surface.

images at four different spots on a flat 2D crystal. Each image is similar to the one in Fig. 3.2b. The values of L_{av} we find are 20.37, 21.52, 20.77, and 19.78. We take an average of all the four values to calculate the mean $L_{av} = 20.61$ which is shown by the red horizontal dotted line in Fig. 3.3. To calculate the distribution for cylindrical

crystals (blue scatter plot points in Fig. 3.3), we measure the lengths of 330 crystalline grains from 11 different experimental samples.

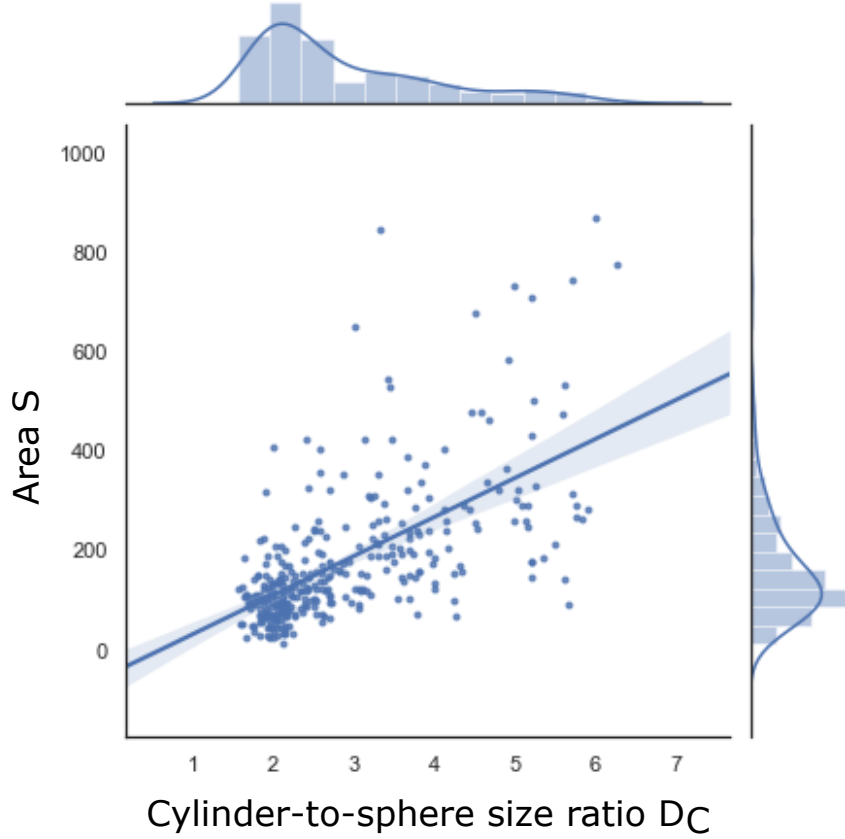


Figure 3.4: Grain area S for different cylinder-to-sphere size ratios D_C . The blue solid line represents a linear fit while the shaded region around it shows the span of one standard deviation.

3.3.2 Area S and anisotropy A

Using equations 3.2 and 3.4, we calculate the area S and anisotropy A for each of the 330 crystal grains. As shown in Fig. 3.4 and Fig. 3.5, the area S increases and anisotropy A decreases with the cylinder-to-sphere size ratio D_C .

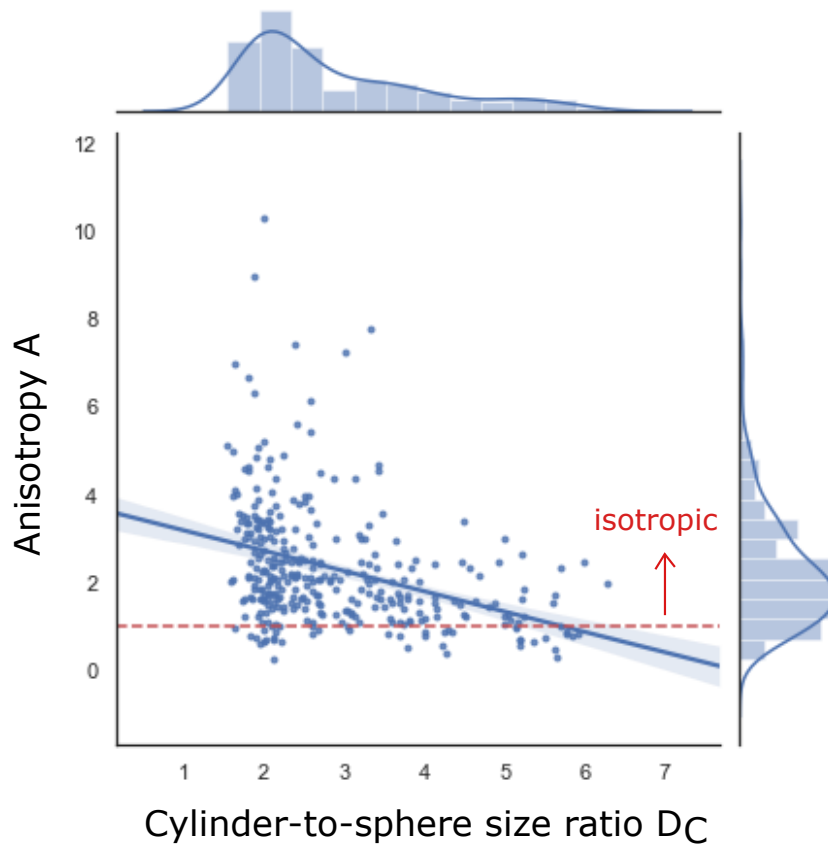


Figure 3.5: (a) Grain anisotropy A measured for various cylinder-to-sphere size ratios D_C . The blue solid line represents a linear fit while the shaded region around it shows the span of one standard deviation. The red dotted horizontal line corresponds to a grain of isotropic shape, with its length equal to its circumference, such that $L = \pi D_C$ and $A = 1.0$.

3.4 Discussions and outlook

Our results show that structure of polycrystals on a thin cylinder deviates from that of on a flat surface. The average grain length on a thin cylinder is shorter than that of a flat surface. To understand these results, we consider how the mechanism of grain growth may differ between a cylinder and flat substrate. From classical

nucleation theory [60], we know that the free energy of the formation of a circular crystalline grain with radius r in 2D can be expressed as

$$\Delta G = 2\pi r\gamma - \pi r^2\Delta\mu n, \quad (3.7)$$

where γ is the line tension of the crystal boundary, $\Delta\mu$ is the difference in chemical potential between the crystal and fluid phases, and n is the number of particles in the crystal per unit area.

The bulk energy (second term in equation 3.7) favors crystal growth while the interfacial energy (first term in equation 3.7) opposes it. Once a grain surpasses the size of a critical nucleus, it can keep growing by acquiring particles from the surrounding fluid. At room temperature, the crystal boundary fluctuates and interacts with other nearby crystalline grains. This often leads to the shrinking and eventual disappearing of the smaller of the two interacting grains because a large crystal has lower surface energy per unit area compared to a small crystal. This process is called Ostwald ripening [61], in which the components of a discontinuous phase preferentially diffuse from smaller to larger droplets through the continuous phase.

Another possible grain growth mechanism is the coalescence of two grains into a single, larger grain [62, 63]. This merging is preferred when (i) the angle between the grain boundaries is sufficiently small, and (ii) the grains themselves are small enough to rotate or translate to merge with each other.

On a flat 2D surface, both ripening and coalescence contribute to grain growth. However, on a cylindrical surface, the condition for coalescence is stricter than that on a flat surface. Once a grain wraps around a cylinder, it can not coalesce with another grain because it loses the degrees of freedom to translate or rotate with respect to the

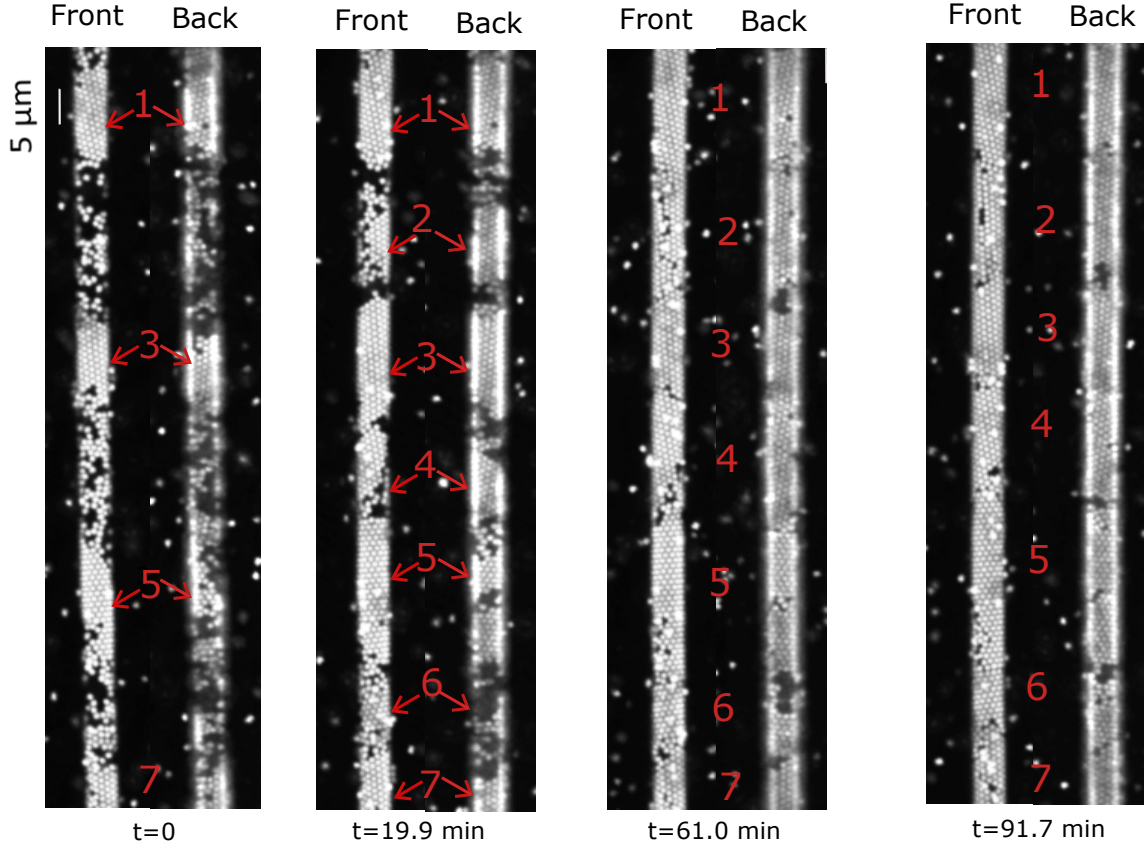


Figure 3.6: Confocal images of crystals growing on a cylinder, as viewed from the front and back sides of the cylinder. Grains 1, 3, 5, and 7 form about 20 minutes earlier than grains 2, 4, and 6. The chiral angle θ of the seven grains are $\theta_1 = 40.91^\circ$, $\theta_2 = 36.87^\circ$, $\theta_3 = 35.32^\circ$, $\theta_4 = 39.69^\circ$, $\theta_5 = 4.93^\circ$, $\theta_6 = 7.35^\circ$, and $\theta_7 = 33.69^\circ$.

cylinder axis. As we observe crystal growth on a cylinder experimentally (Fig. 3.6), we see that some grains finish wrapping around the cylinder (grains 1, 3, 5, and 7) before others even nucleate (grains 2, 4, and 6). The ones that wrap around earlier are stable and do not merge into the adjacent grains even though the mismatch in their chiral angles or orientations is quite small. As shown in Fig. 3.6, the chiral angles of grains 1, 2, 3, and 4 are very similar, but they do not merge with each other, and then maintain their boundaries for a long period of time ($t = 61$ min and $t = 91.7$ min).

This is probably why we find that the average grain length L is smaller than L_{av} on a 2D surface specifically for thin cylinders. On a thin cylinder, a grain can wrap around the cylinder quickly and once it does, grain growth through coalescence may slow down. Afterwards, grains can still grow through Ostwald ripening, but ripening is driven by particle diffusion from one grain to another, which may not be possible to observe on experimental timescales.

Furthermore, Ostwald ripening may be slowed by the absence of curvature at the grain boundaries. Because the grain boundaries are oriented normal to the cylinder axis, their interfacial energy remains constant during growth (Fig. 3.1). Consequently, as a fully wrapped crystal grows, it does not pay any additional cost in interfacial energy.

Chapter 4

Random parking of colloidal spheres on a cylinder

This Chapter is based on the following publication: *Europhysics Letters* **127** (3), 38004 (2019) – Edvin Memet, **Nabila Tanjeem**, Charlie Greboval, Vinothan N. Manoharan, L. Mahadevan.

This work was supported by the Harvard MRSEC under National Science Foundation grant no. DMR-1420570.

4.1 Introduction

Adsorption processes in which particles are randomly deposited on an extended substrate can occur in a broad range of physical, chemical, and biological systems, such as binding of ligands on polymer chains, chemisorption, physisorption, coating, paint, filtration, designing composites, drug delivery, and solid-state transformations

[64, 65, 66, 67, 24, 68]. On the one hand, the monolayer adsorption of small molecules is usually described by an equilibrium picture, resulting from adsorption-desorption kinetics, particle hopping, or diffusion [64, 69]. On the other hand, larger molecules (proteins, viruses, bacteria, colloids, cells) may interact with the surface so strongly that they exhibit virtually no desorption, surface diffusion, or reaccommodation, and do not interact with subsequently adsorbed molecules except for steric exclusion effects [70, 71, 72, 69]. The irreversible particle deposition that occurs in such nonequilibrium systems can be modeled as a random sequential adsorption (RSA) process [69, 73], also known as a “car parking problem” in the one-dimensional continuum case [74].

Two natural questions are of central interest in RSA [75, 76, 77]. The first is the surface coverage fraction ρ_∞ – the ratio of surface covered by adsorbed particles to the total collector area in the longtime limit, when there is no more space for additional particles to adsorb. This surface coverage fraction is smaller than the close-packing density. The second is the kinetics of particle adsorption $\rho(t)$. The answers to both these questions depend on the geometry, dimensionality, size, and shape of the particles being adsorbed [67].

The simplest version of the problem is the case of uniform size segments being adsorbed on an infinite line, solved analytically by Renyi [74]. Since then, many variants of this problem have been studied by considering the role of dimensionality and shape of both the particles and the substrate as well as particle size distribution. These include considerations of heterogeneous 1D particles on 1D substrates, 1D particles on flat 2D substrates (needles on a plane [78, 70], polymer chains on a lattice [79, 65], dimers on a ladder [80, 81]), 2D particles on flat 2D substrates (disks,

rectangles/ellipses [82, 78] with fixed or arbitrary orientation, stars and other concave objects [83], mixed concave/convex objects [67], or compound objects [76] on a plane or on a narrow strip [84]); 3D particles on fractals [85] or porous solids [69]; and 3D particles on flat 2D substrate (polydisperse spheres on a plane [86]).

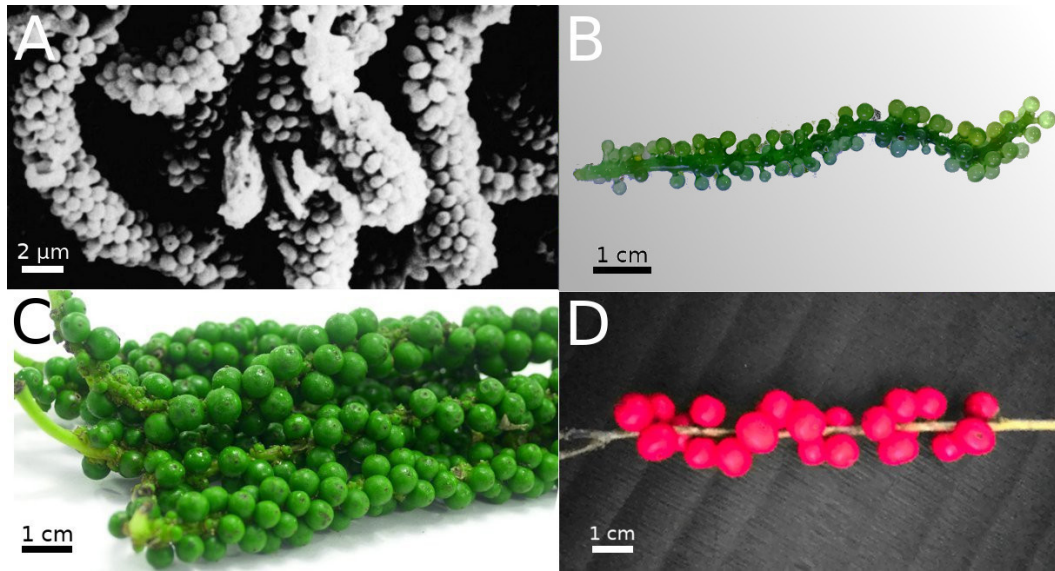


Figure 4.1: Spheres-on-cylinder morphologies in (a) dental plaque “corncob” formations [5], (b) sea grapes, (c) peppercorn drupes, and (d) winterberries.

Here we consider the adsorption of spheres on a cylindrical wire, inspired by a range of biological systems that exhibit such a morphology, such as those shown in Fig. 4.1. These include dental plaque which exhibits a “corncob” morphology (Fig. 4.1a), comprised of streptococci held by an extracellular polysaccharide matrix on large filamentous bacteria [87, 5], and fruits such as peppercorn, winterberry, and seagrapes (Fig. 4.1b, c, and d), where phyllotaxis may also be relevant [21, 88]. Despite the commonality of these observations, there seem to be few studies on the adsorption of objects onto curved substrates.

Some exceptions include parking on spheres [71, 89, 24, 19, 90, 91, 92], hyperboloids [92], projective planes [92], and cylinders [24]. Previous studies [24, 93] have argued that the asymptotic coverage $\rho_{\infty}^{\text{cyl}}$ for random parking of spheres of radius R on a cylinder of radius r and length L can be related to that of disks on a flat plane by effectively unrolling the cylinder that passes through the centers of the particles: $\rho_{\infty}^{\text{cyl}} := N_{\infty} \pi R^2 / (2\pi r L) = \rho_{\infty}^{\text{plane}} (1 + R/r)$, where N_{∞} is the number of particles adsorbed in the infinite time limit. This approximation is valid for relatively small values of R/r but breaks down as particles become larger compared to the cylinder ($R/r \rightarrow \infty$) – in other words, when wire curvature becomes important. Here, we do not limit ourselves to the weak curvature regime and use a combination of analysis, simulations, and experiments to characterize the asymptotic coverage of spheres on a rigid wire as a function of R/r .

4.2 Theory

We start by noting that the adsorption of spheres of radius R on a cylinder of radius r is characterized by two degrees of freedom – the axial coordinate z and the azimuthal angle ϕ (Fig. 4.2a). Consequently, it is possible to map the 3D geometry of this process onto a 2D adsorption problem in the $\phi - z$ plane, where spheres are characterized by an angular envelope with an extent that depends on the axial coordinate. Such a transformation has been used previously in studies pertaining to the packing of spheres inside a cylinder [1, 30, 94]. To find this angular envelope, consider a sphere whose center is located at (z_0, ϕ_0) . In a horizontal slice at height z , the radius of the circle is $s(z - z_0) = \sqrt{R^2 - (z - z_0)^2}$ and its angular extent is

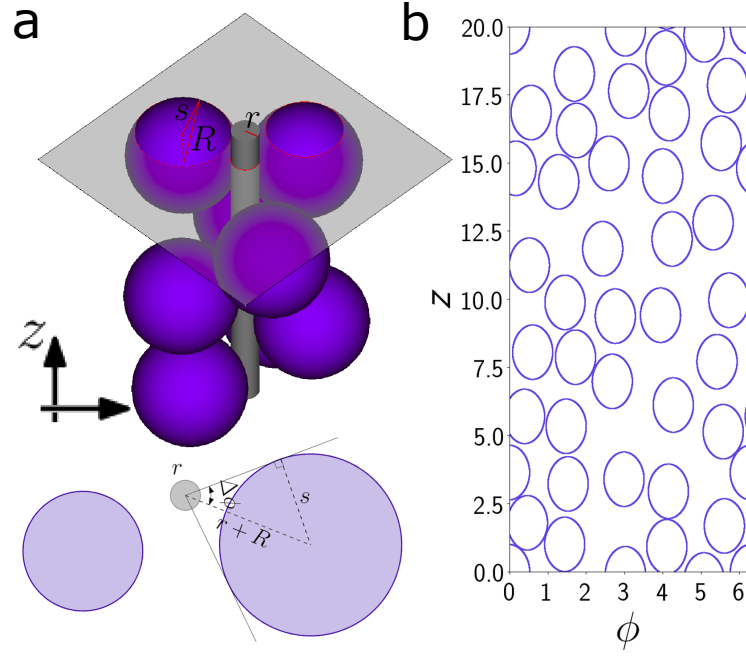


Figure 4.2: **(a)** Cartoon of spheres adsorbed on a wire. A sectioning plane indicated through the shade change is shown below, with r indicating the cylinder radius and R the particle radius, ρ indicating the radius of a particular cross-section through the particle, and $\Delta\phi$ indicating the angle subtended by the particle cross-section at the center of the wire. **(b)** Two-dimensional representation in the $\phi - z$ plane of spheres of radius $R = 1$ adsorbing on a cylinder of radius $r = 1$ and length $L = 20$.

$\Delta\phi = \arcsin(s(z - z_0)/(R + r))$ (Fig. 4.2a). This gives us an equation for $\phi(z)$ – that is, the shape of a sphere in the $\phi - z$ plane:

$$\begin{aligned} \phi(z - z_0) &= \phi_0 \pm \Delta\phi \\ &= \phi_0 \pm \arcsin \left[\frac{\sqrt{R^2 - (z - z_0)^2}}{(R + r)} \right], \end{aligned} \quad (4.1)$$

where $z - z_0 \in [-R, R]$.

Consequently, random sequential adsorption of spheres on a cylinder is equivalent to random sequential adsorption of oblong 2D objects with shape given by Eq. 4.1

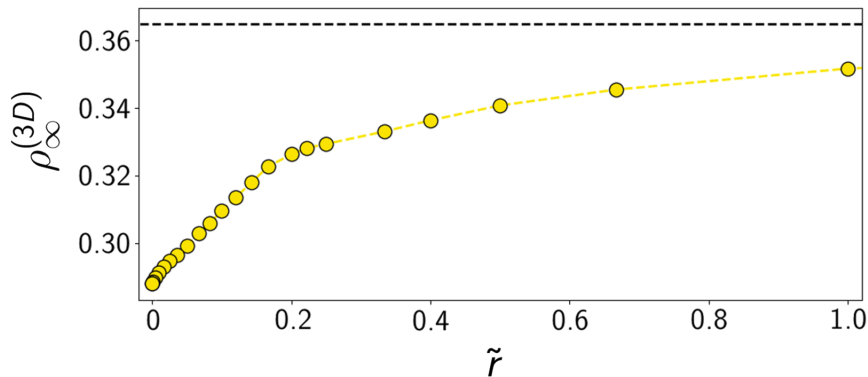


Figure 4.3: Longtime coverage $\rho_{\infty}^{(3D)}$ versus scaled wire size $\tilde{r} = r/R$ (Eq. (4.3)) from effective 2D simulations of spheres parking on a cylinder. The dashed black line indicates the longtime coverage for random sequential adsorption of spheres on a plane, $\lim_{\tilde{r} \rightarrow \infty} \rho_{\infty}^{(3D)} = (2/3) \lim_{\tilde{r} \rightarrow \infty} \rho_{\infty}^{(2D)} \approx 0.3647$, where $\lim_{\tilde{r} \rightarrow \infty} \rho_{\infty}^{(2D)} \approx 0.5471$ is the asymptotic coverage of discs on a plane [6].

on a 2D strip of width 2π and length L (Fig. 4.2b). We simulate the latter process for different values of the ratio between cylinder and particle size $\tilde{r} \equiv r/R$, using periodic boundary conditions. For each deposition attempt we generate a pair of random numbers (ϕ, z) representing a potential adsorption site and check for overlaps with existing particles in the vicinity. In the absence of overlaps, the trial particle is successfully adsorbed and remains fixed thereafter; otherwise it is removed from the system. Since reaching a completely blocked state in which there remains no space for new particles to adsorb may take very long, we instead extrapolate N_{∞} , the asymptotic number of particles deposited on the cylinder, from the longtime kinetics [95, 83, 82]. That is, for particles with two degrees of freedom, $\rho_{\infty} - \rho(\tau) \sim \tau^{-1/2}$, as $\tau \rightarrow \infty$ [96], where scaled time τ is the attempt number times the area fraction of a particle scaled by the total area of the substrate. In addition, to minimize boundary effects, we use a cylinder size L that is large compared to the particle size R [76].

To find the longtime coverage from N_∞ , we define coverage as the ratio of occupied to available area in the 2D $\phi - z$ space (where “area” has dimensions of length, since it is defined in the $\phi - z$ plane). The area occupied by a sphere is $A = \tilde{A} R$ where \tilde{A} is the dimensionless area, $\tilde{A} = 2 \int_{-1}^1 \arcsin \left[\frac{\sqrt{1 - \tilde{z}^2}}{1 + \tilde{r}} \right] d\tilde{z}$, expressed in terms of the scaled axial coordinate $\tilde{z} = (z - z_0) / R$ and scaled cylinder radius $\tilde{r} = r / R$. If we let N be the total number of spheres adsorbed up to the current time and $L \rightarrow \infty$ be the length of the cylinder, the 2D coverage density is given by

$$\rho^{(2D)}(\tilde{r}) = \frac{N \tilde{A} R}{2\pi L} = \frac{1}{2\pi} \frac{N}{\tilde{L}} \tilde{A} = \frac{\lambda(\tilde{r}) \tilde{A}(\tilde{r})}{2\pi}, \quad (4.2)$$

where $\tilde{L} = L / R$ is the scaled cylinder length and $\lambda = N / \tilde{L}$ is the scaled linear particle density. We note that in the limit $\tilde{r} \rightarrow 0$, we have $\tilde{A} \rightarrow 4$ and $\rho^{(2D)} \rightarrow 2\lambda(\tilde{r}) / \pi$, while as $\tilde{r} \rightarrow \infty$, $\tilde{A} \rightarrow \pi / \tilde{r}$ and $\rho^{(2D)} \rightarrow \lambda(\tilde{r}) / (2\tilde{r})$.

To help facilitate the comparison to experiments, we convert the surface coverage $\rho^{(2D)}$ to a three-dimensional coverage representing the ratio between the total volume of the adsorbed spheres and the total available volume – that is, the volume of the cylindrical annulus of inner radius r and outer radius $r + 2R$:

$$\rho^{(3D)}(\tilde{r}) = \frac{4/3 N \pi R^3}{4\pi R L (R + r)} = \frac{1}{3} \frac{N}{\tilde{L}} \frac{1}{1 + \tilde{r}} = \frac{1}{3} \frac{\lambda(\tilde{r})}{1 + \tilde{r}}. \quad (4.3)$$

We note that in the low-curvature regime, $\tilde{r} \rightarrow \infty$, $\rho^{(3D)} \rightarrow \lambda(\tilde{r}) / (3\tilde{r}) \approx 0.3647$ (Fig. 4.3), while in the high-curvature regime, $\tilde{r} \rightarrow 0$, $\rho^{(3D)} \rightarrow \lambda(\tilde{r}) / 3$.

How do these densities compare to the maximum densities achieved by close-packed spheres on the surface of a cylinder? To get the maximum packing density as a function of the ratio of wire and particle size, we refer to the literature on packing spheres *inside* cylinders [1, 30, 97, 21]; as long as there is a single layers of particles inside

the cylinder (that is, all the particles are in contact with the cylinder), the packing densities can be easily mapped to densities corresponding to packing *on* the surface of a cylinder. Using this method we find that the ratio of random to close-packed densities varies around 0.62. For example, when $\tilde{r} \rightarrow 0$, the random parking density is around 0.288 (Fig. 4.3), while the densest packing of spheres inside a cylinder twice as large as the particles is around 0.47, giving a ratio of 0.61. Similarly, when $\tilde{r} = 0.5$, the corresponding ratio is approximately 0.63.

4.3 Experiments

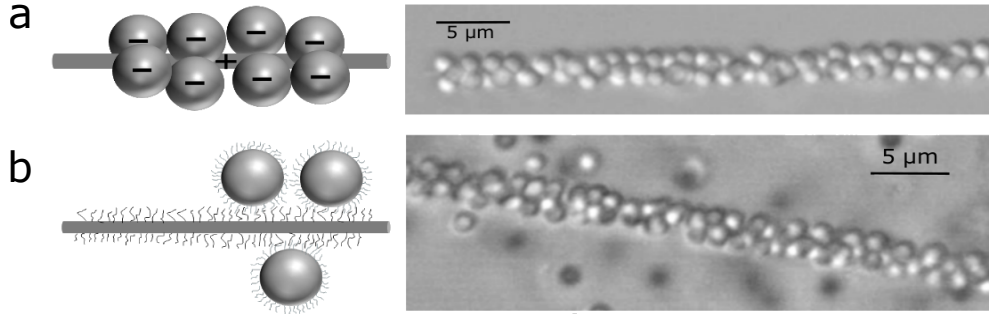


Figure 4.4: **(a)** Schematic (left) and optical micrograph (right) of negatively charged particles binding irreversibly to a positively charged nanowire **(b)** Schematic (left) and optical micrograph (right) of DNA-coated particles binding to nanowire coated with complementary DNA strands.

To test our predictions, we designed an experimental system consisting of colloidal microspheres that can irreversibly attach to a wire (see Materials and Methods for details of the protocols). An aqueous dispersion of microspheres, which have an average radius $R = 0.65 \mu\text{m}$, is allowed to adhere to a silica wire via two different kinds of attractive interactions to drive the microsphere to adsorb: electrostatic and

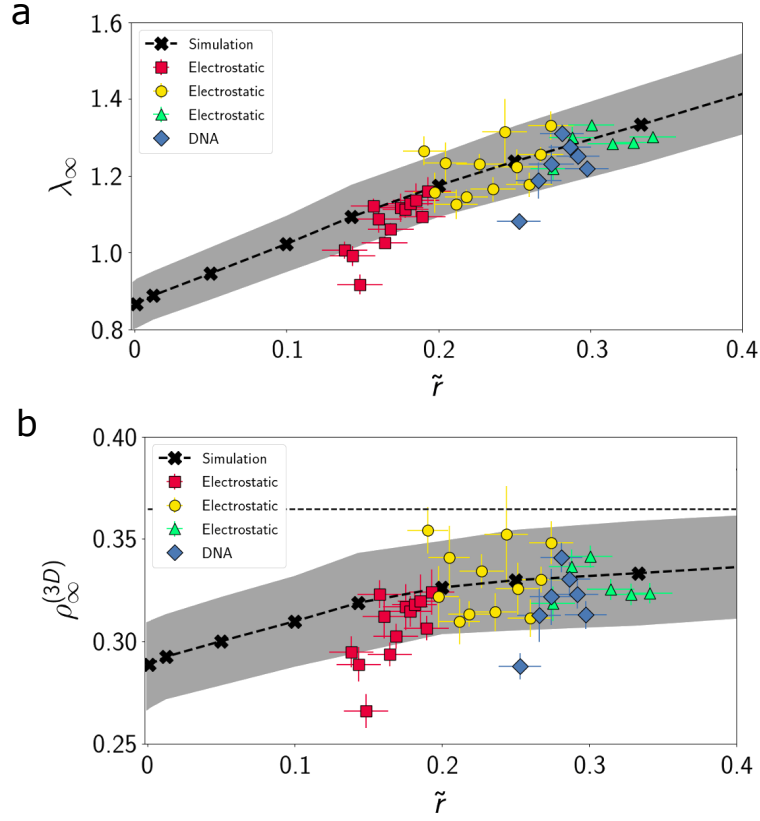


Figure 4.5: **(a)** Linear particle density λ versus scaled wire size $\tilde{r} = r/R$ and **(b)** 3D asymptotic density $\rho_\infty^{(3D)}$ versus scaled wire size $\tilde{r} = r/R$ from simulations (black crosses), and experiments using either electrostatic attraction (red squares, yellow circles, and green triangles show results from three different experiment samples) or DNA hybridization (blue diamonds). The dashed black line indicates, as in Fig. 4.3, the longtime coverage for random sequential adsorption of spheres on a plane, $\lim_{\tilde{r} \rightarrow \infty} \rho_\infty^{(3D)} \approx 0.3647$. Shaded regions indicate an interval of two standard deviations from the mean simulation results. In order to reproduce the experimental uncertainty associated with small particles numbers, simulations were performed on short wire segments that accommodate around 50 particles.

DNA-mediated interactions. For electrostatic-mediated adsorption, we use oppositely charged microspheres and nanowires. The surfaces of the colloidal polystyrene microspheres contain negatively charged sulfate groups. To impart positive charge to the nanowire, we coat it with a cationic polyelectrolyte, poly-diallyldimethylammonium

chloride. After the colloidal microspheres are dispersed in water in the presence of the nanowire, they adsorb on the wire surface (Fig. 4.4a).

For DNA-mediated adsorption, we functionalize the colloidal microspheres and silica nanowire with complementary DNA strands, which at room temperature can form strong, irreversible bonds between the wire and the particles (Fig. 4.4b). The DNA strands contain a dibenzocyclooctyne (DBCO) group, which binds to an azide group of a polymer layer deposited on the surfaces of the wire and the microspheres. For both electrostatic and DNA-mediated adsorption, we do not observe particles diffusing on the surface or desorbing within the experimental timescale. Furthermore, in both systems, the range of the interaction between adsorbed particles is much smaller than the particle size. Thus, both experimental systems provide a reasonable realization of the random sequential adsorption process. Using experiments on wires with different radii that range from 0.1–0.6 μm allows us to examine adsorption over a range of \tilde{r} values.

To find $\rho_\infty^{(3D)}$ experimentally, we count the number of particles N_∞ adsorbed on a wire segment of length L and average radius r and compute the normalized linear particle density for that segment, $\lambda_\infty(\tilde{r}) = N_\infty/\tilde{L}$. The results from experiments using electrostatic interactions are consistent between different samples (red squares, yellow circles, and green triangles in Fig. 4.5a) and with results obtained using DNA-mediated attraction (blue diamonds in Fig. 4.5b).

We see that our experimental results are consistent with results of simulations (Fig. 4.5a, black line) on wire segments of comparable length to the wire segments in the experiments (Fig. 4.4a and 4.4b). While a few experimental points lie outside

the two-sigma interval (Fig. 4.5a, black shaded region) of the simulation results, these deviations are likely associated with the effects of energetics and kinetics. In our analysis and simulations, all contacts are assumed to be point contacts, while in reality, the contact interactions have a non-zero range. As a result, the energy of a contact decreases as the curvature of the wire increases. Consequently, the regime in which wires are highly curved (small \tilde{r}) is difficult to probe experimentally because weakly bound particles on highly curved wires can detach more quickly, leading to undersaturation. Indeed, the data are consistent with this hypothesis – the measured densities at the smallest \tilde{r} values for both the electrostatic and DNA-mediated interactions fall below the simulated values (Fig. 4.5a and 4.5b, red squares and blue diamonds). Nonetheless, outside of these values, the experimental results agree with those of simulation, and, importantly, both the simulations and experiments show that the longtime coverage lies below that for random sequential adsorption on a plane (Fig. 4.5b). These results validate our understanding of random sequential adsorption at weak to moderate wire curvature ($\tilde{r} \gtrsim 0.2$).

4.4 Discussions

Although energetic and kinetic limitations prevent us from experimentally exploring the limit of high wire curvature ($\tilde{r} \lesssim 0.2$), we can understand this regime theoretically in terms of the effective parking of 2D shapes on the unwrapped cylinder (Eq. (4.2)). Simulations in this regime reveal a surprising effect: $\rho_\infty^{(2D)}$ varies non-monotonically with wire radius (Fig. 4.6), in contrast to λ_∞ and $\rho_\infty^{(3D)}$, both of which vary monotonically with \tilde{r} (Figs. 4.3, 4.5a, 4.5b). To understand this, we note that from Eq. (4.2) we see

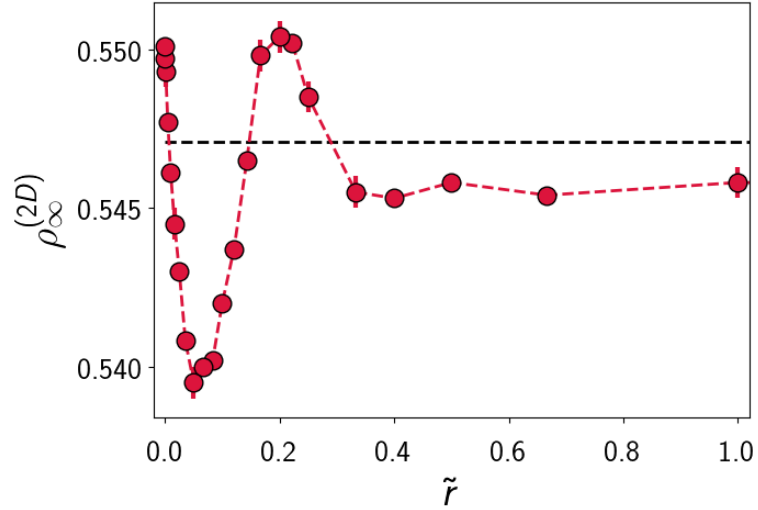


Figure 4.6: Longtime (asymptotic) coverage $\rho_{\infty}^{(2D)}$ versus scaled wire size $\tilde{r} = r/R$ (Eq. (4.3)) from simulation. The dashed black line at 0.5471 indicates the longtime coverage for the random adsorption of discs on the plane (that is, in the limit $\tilde{r} \rightarrow \infty$).

that $\rho_{\infty}^{(2D)}$ is the product of two terms that depend on the scaled cylinder radius \tilde{r} .

While $\tilde{A} = 2 \int_{-1}^1 \arcsin [\sqrt{1 - \tilde{z}^2}/(1 + \tilde{r})] d\tilde{z}$ necessarily decreases as \tilde{r} increases, the asymptotic particle density $\tilde{\lambda}_{\infty}$ increases with \tilde{r} , since the maximum angular extent $\Delta\phi_{\max} = \sin^{-1}(1/(1 + \tilde{r}))$ decreases, allowing for more spheres to fit around the wire. The contrasting behavior of the two terms indeed allows for the observed non-monotonicity in $\rho_{\infty}^{(2D)}$, though it does not guarantee it. In contrast, we find $\rho_{\infty}^{(3D)}$ increases monotonically with \tilde{r} in simulations (Fig. 4.3), even though Eq. (4.3), which expresses $\rho_{\infty}^{(3D)}$ as the ratio of two terms that both increase with \tilde{r} , does not exclude non-monotonic behavior.

Having examined the longtime coverage as a function of wire curvature, we now turn to the second quantity of interest, the kinetics of particle adsorption. Interestingly, in idealized conditions where the energetics of the substrate-particle interaction play

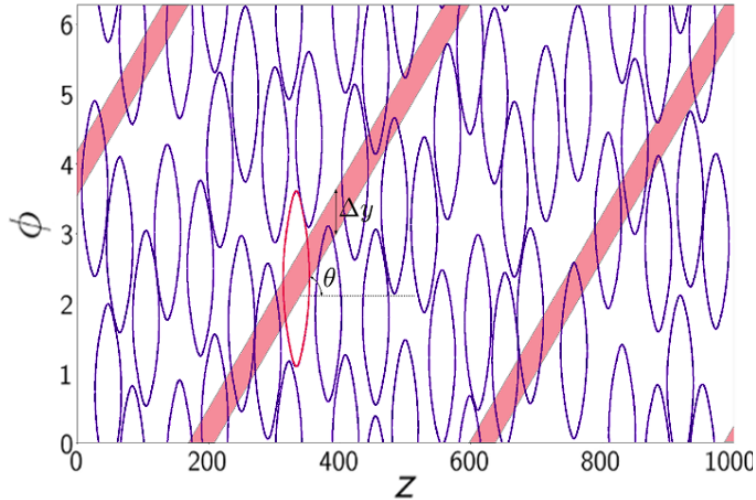


Figure 4.7: Two-dimensional representation in the $\phi - z$ plane of spheres of radius $R = 20$ adsorbing on a cylinder of radius $r = 1$ and length $L = 1000$. To compute the angular density-density correlation function, we fix a particle (shown in red), consider a strip of width Δy along a direction θ , and count the number of particles whose centers are contained inside this strip. Repeating this procedure for all particles and then for different angles θ yields the plot in Fig. 4.8.

no role, there is a near-universal law (for convex particles) associated with the kinetic approach to the asymptotic coverage, described by a power-law form [67, 98]

$$\rho_{\infty} - \rho(\tau) \sim \tau^{-1/d_f}, \quad \tau \rightarrow \infty, \quad (4.4)$$

where time τ is defined so that each trial (adsorption attempt) corresponds to a scaled time increment equal to the area of an adsorbing particle scaled by the system area and d_f represents the number of degrees of freedom of the object. In our system $d_f = 2$, meaning that we expect to find $\rho_{\infty} - \rho(\tau) \sim \tau^{-1/2}$. However, we also note that quasi-one-dimensionality emerges with increasing wire curvature, in that the 2D strip in $\phi - z$ space becomes increasingly narrow in the ϕ direction, which could change the

asymptotic kinetics accordingly [84]. For example, in the limit $\tilde{r} \rightarrow 0$, the strip allows no more than two spheres to fit (tightly) around the cylinder at the same value of z . However, we do not observe a crossover to 1D asymptotic kinetics in our simulations as $\tilde{r} \rightarrow 0$, which suggests that the asymptotic exponent $d_f = 2$, independent of the scaled cylinder size \tilde{r} .

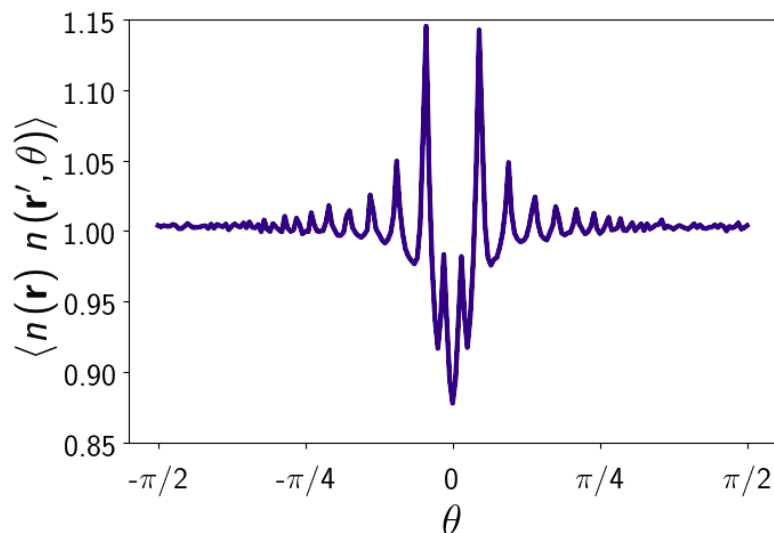


Figure 4.8: Plot of the angular density-density correlation $\langle n(\vec{r}) n(\vec{r}', \theta) \rangle$ as a function of angle θ .

Strongly and weakly charged colloidal chiral orderings in cylinders have been studied both theoretically and experimentally [20, 99]. An interesting question is whether any chiral order emerges on short scales in our random adsorption process, where the system is not allowed to relax to its ground state. Long-time adsorption structures such as those shown in Fig. 4.7 suggest that there may be preferential alignment along certain directions. To quantify the alignment, we define an angular density-density correlation $\langle n(\vec{r}) n(\vec{r}', \theta) \rangle$ which counts pairs of particles whose centers

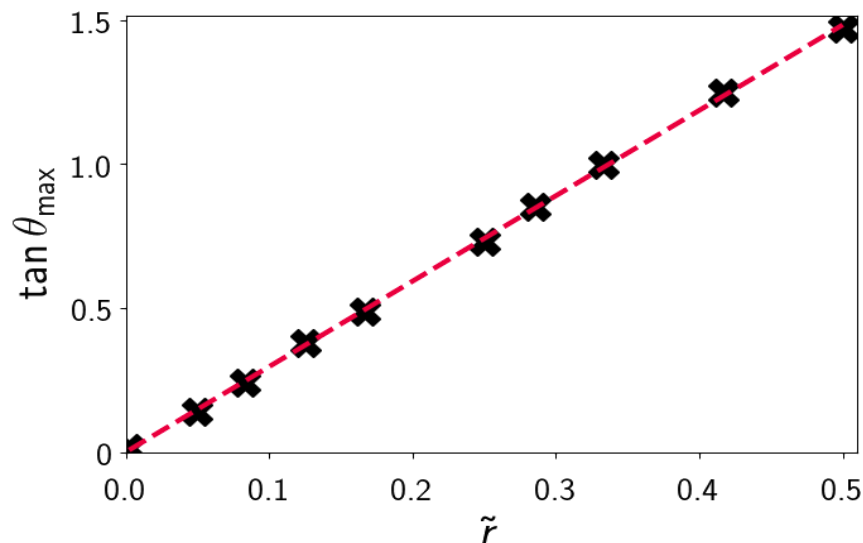


Figure 4.9: Varying $\tilde{r} = r/R$ changes the maximal density direction θ_{\max} (that is, the angle for which $\langle n(\vec{r}) n(\vec{r}', \theta) \rangle$ is maximum) as $\tan \theta_{\max} \approx 3\tilde{r}$.

are aligned at an angle θ within some tolerance Δy (Fig. 4.7, red shaded regions). An example of this correlation function is shown in Fig. 4.8 for the case in which we consider only pairs of particles within a range of $10R$ from each other. From visual inspection of Fig. 4.7, the density-density correlation function exhibits two moderate peaks at values of $\pm\theta_{\max}$ symmetric around $\theta = 0$. Sufficiently increasing the range over which we compute density correlations will eventually lead to the disappearance of the peaks. This is what we expect intuitively: as noted previously, random parking densities are only about 60% of the maximum close-packing densities, which suggests that ordering cannot survive on arbitrarily large scales.

Repeating this analysis for different values of $\tilde{r} = r/R$, we find that the maximal density direction θ_{\max} varies with \tilde{r} (Fig. 4.9, black crosses) such that the relationship between $\tan \theta_{\max}$ and \tilde{r} is linear: $\tan \theta_{\max} \approx 3\tilde{r}$ (Fig. 4.9, red dashed line). Very large

particles ($R \gg r$ or $\tilde{r} \rightarrow 0$) tend to be slightly more aligned axially, while smaller particles (increasing \tilde{r}), with $\theta_{max} \rightarrow \pi/2$, tend to be more aligned radially (to take advantage of the additional space available due to substrate curvature).

4.5 Conclusion

In this chapter, we have examined the random adsorption of large spherical particles on a thin cylindrical wire. By reducing the 3D adsorption problem to an effective 2D problem, we showed that curvature effects can indeed become significant and thus cannot be treated as a small perturbation. In order to test our predictions for the longtime particle density λ_∞ as a function of the ratio \tilde{r} of particle to wire size, we performed experiments in which the particle-wire interaction was mediated by electrostatics or DNA hybridization and showed the results are consistent with each other and with the results of simulations. While the high curvature limit was not accessible experimentally because of kinetic effects, simulations in this regime reveal an intriguing non-monotonic behavior of the 2D asymptotic coverage $\rho_\infty^{(2D)}$. Meanwhile, the 3D asymptotic coverage $\rho_\infty^{(3D)}$ varies monotonically with the ratio \tilde{r} of wire to particle size, providing a recipe for designing structures with well-defined volume coverage simply by tuning the ratio of the radii. Accounting for the energetics of substrate and particle deformation is a natural, if complicated, next step.

4.6 Materials and methods

4.6.1 Nanowire fabrication

We fabricate a thin cylindrical wire by tapering an optical fiber made of silica (supplied by Newport Corporation, part number F-SMF-28). First, we strip the outer layer from a piece of a fiber and clean the cladding by wiping it with isopropanol. We then attach the two ends of the fiber to two motorized stages (Stepping motor controller supplied by SURUGA SEIKI, Part number D220) and place a hydrogen/oxygen type 3H torch at the center of the fiber. Pulling the fiber by the motorized stages while the torch applies heat thins the wire down gradually until it eventually breaks [32, 33, 34]. The resulting wires are imaged with scanning electron microscopy, which allows us to measure the local wire diameter. Data from four different nanowires show that the change in wire diameter is approximately linear and gradual along the length of the fiber. Diameter variations for four different wires per 10 μm length are 1.76 nm, 3.63 nm, 5.12 nm, and 3.85 nm.

4.6.2 Preparation of positively charged nanowire

We submerge the nanowire overnight in a 1 M KOH solution to impart a negative charge to its surface. After the KOH treatment, we wash the nanowire five times with MilliQ water and transfer it to a solution of poly-diallyldimethylammonium chloride (shortened as polyDADMAC, purchased from Polysciences Inc., Molecular weight 240,000) in 20 mM Tris-HCl buffer, prepared by mixing 28% w/w polyDADMAC in water with 40 mM Tris-HCl in 50:50 ratio and vortexing for 30 s. After waiting 4–5

hours to allow the polyDADMAC to coat the nanowire, providing a positively charged surface, we take the nanowire out and wash it well with MilliQ water.

4.6.3 Preparation of negatively charged colloidal particles

We purchase 8% w/v sulfate-modified polystyrene particles (supplied by Molecular Probes, Life Technologies Inc.) with an average diameter of 1.3 μm and wash them three times by centrifuging at 4000*g* and re-dispersing in MilliQ water. After the final wash, we disperse them in 0.05 mM NaCl in water, resulting in a final particle concentration of 2% w/v.

4.6.4 Preparation of DNA functionalized nanowire

To functionalize the silica nanowire with DNA oligonucleotides, we first clean it by overnight submersion in 1 M KOH, then rinse with MilliQ water five times, and transfer it into (3-aminopropyl) triethoxysilane (APTES) solution. We prepare the solution by mixing 100 mL methanol (99.9%, supplied by VWR), 5 mL glacial acetic acid (99.8%, supplied by Acros Organics), and 3 mL APTES (99%, supplied by Sigma-Aldrich). After treating the nanowire in this solution for 30 min, we rinse it with methanol and MilliQ water and transfer it to a PEG solution. The PEG solution is prepared by mixing NHS-PEG (5000 Da, supplied by Nanocs) and NHS-PEG-N₃ (5000 Da, supplied by Nanocs) in 10:1 ratio and dissolving them in 0.1 M sodium bicarbonate buffer. We place the nanowire along with 192 μL of PEG solution between two glass coverslips and leave it overnight, at room temperature, so that the amino groups from APTES can form covalent linkages through *N*-hydroxysuccinimide

(NHS) chemistry and form a PEG layer. The following day, we take the nanowire out from the PEG solution and rinse it with MilliQ water. Afterward, we attach DNA oligonucleotides to the NHS-PEG-N₃ molecules on the nanowire surface by copper-free click chemistry [100]. The DNA strands are 64-bases long and are synthesized with a dibenzocyclooctyne (DBCO) group on the 5'- end (purchased from Integrated DNA Technologies, HPLC purified). We put the nanowire in 10 μ M of 168 μ L DBCO-DNA (5'-T₅₀-AAGAGTAGGTTGATG-3') in phosphate buffer, sandwich it between two coverslips, and leave it for 24 h before finally rinsing the nanowire with MilliQ water.

4.6.5 Preparation of DNA functionalized colloidal particles

To coat the polystyrene microspheres with high density DNA brushes (5'-T₅₀-CCACATCAACCTACT-3') we incorporate a diblock copolymer made from polystyrene and poly(ethylene oxide)-azide into the microspheres and then attach DBCO-DNA to the azide functional group using copper-free click chemistry [101].

4.6.6 Sample setup, imaging, and data analysis

After either functionalization method, we place the functionalized nanowire between two glass coverslips to make a sandwich sample chamber whose thickness is set to 67 μ m using mylar-film spacers. We then inject the suspension of particles and wait 10 min before washing out excess particles. We wash by injecting a control solution with the same salt concentration as the colloidal suspension. We use NaCl for electrostatic screening in both cases: 0.05 mM NaCl for electrostatic interactions and 200 mM NaCl for DNA-mediated interactions.

Finally, we image the sample using a $60\times$ water immersion objective. Using optical microscopy images (Fig. 4.4a, 4.4b), we count the number of particles on wire segments of about $30\text{ }\mu\text{m}$ (chosen such that the segment diameters do not vary significantly along the length) and calculate \tilde{N} . We assign error bars on $\tilde{r} = r/R$ based on the known polydispersity in particle size and the uncertainty in estimating the diameter of the wire. To calculate this uncertainty, we use the uncertainty in fitting and the difference in wire diameter between the two ends of the segment analyzed. Because the experimental images analyzed do not have periodic boundary conditions at the end of the wire segments, we find a number of particles that are only partially in the field of view of each analyzed segment. For each segment, we assign a lower limit of \tilde{N} by not counting those particles and an upper limit by counting them. Then we calculate the mean and standard deviation of \tilde{N} to assign an error bar to \tilde{N} .

Chapter 5

Polyhedral plasmonic nanoclusters through multi-step colloidal chemistry

The research described in this Chapter is performed in collaboration with Nicholas B. Schade, Cyril Chomette, Mona Tréguer-Delapierre, Serge Ravaine, and Etienne Duguet. This work was supported by the National Science Foundation under grant no. DMR-1420570.

5.1 Introduction

Fabricating plasmonic structures for three-dimensional optical metamaterials [102, 103] requires precise arrangements of metal and dielectric. The optical response of such materials is sensitive to nanometer-scale variations in both the thickness of metal coatings as well as the distances between metal surfaces. To date, two general approaches have been developed to create such structures: lithography, in which metal

and dielectric are patterned and deposited stepwise [104, 105, 106, 107, 108] and self-assembly, in which metallodielectric nanoparticles form nanoclusters, driven by DNA-mediated [109, 110] or capillary interactions [111, 112]. Lithographic approaches offer precise control over morphology but limited throughput, and they do not easily scale to three dimensions. Self-assembly approaches offer high precision but limited control over morphology. Here we demonstrate a third approach that is based neither on lithography nor self-assembly: multi-step colloidal synthesis. Starting from highly monodisperse silica seeds, we grow octahedral clusters of polystyrene spheres using seeded-growth polymerization. We then overgrow the silica and remove the polystyrene to create a template to which we attach exactly six silica satellite particles that we can then coat with gold. Using single-particle spectroscopy, we demonstrate that this approach leads to clusters with plasmonic resonances that are reproducible from cluster to cluster. By comparing the spectra to theory, we show that the chemical synthesis approach can control the distances between metallic and dielectric surfaces to nanometer-scale precision. More broadly, our approach illustrates how different, high-yield colloidal synthesis elements can be combined to produce bulk quantities of specific morphologies, much as is done in organic synthesis.

5.2 Multi-step synthesis of plasmonic nanoclusters

We focus on the creation of nanoclusters with octahedral symmetry because the high symmetry may enable their use in metafluids [113, 114]. We first synthesize a silica template with octahedrally-coordinated “dimples” [115, 116], as shown in steps 1–4 of Fig. 5.1. This method takes advantage of several high-yield synthetic steps: a

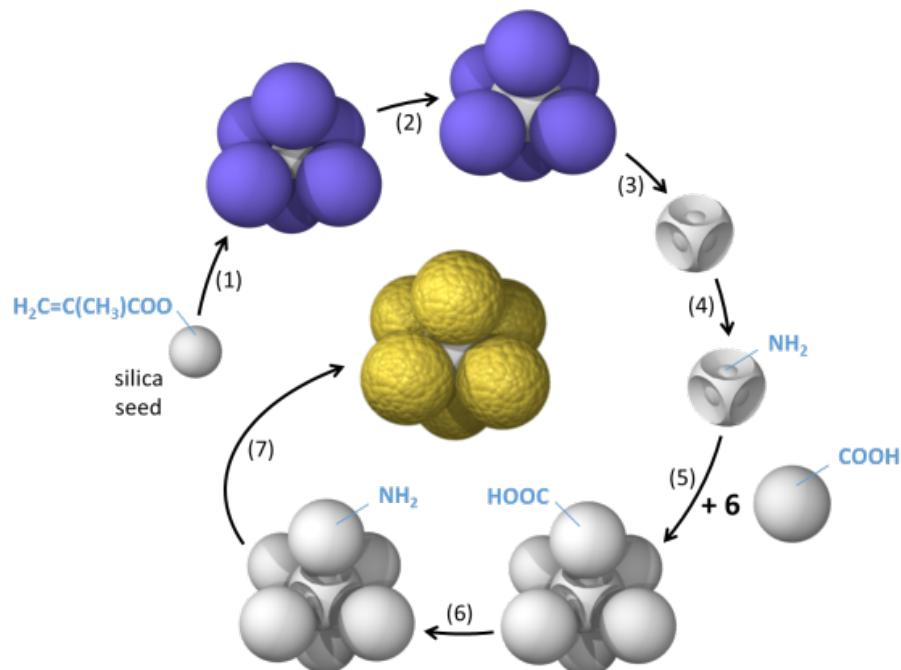


Figure 5.1: Our synthesis scheme for plasmonic clusters consists of seven steps: (1) We perform seeded-growth emulsion polymerization of styrene on spherical silica particles with a diameter of 86 nm. (2) We then overgrow the silica seed and (3) dissolve polystyrene, which results in structures with six concave dimples. (4) We aminate the residual polystyrene at the bottom of the dimples to complete the template. (5) We lock carboxylated silica nanospheres with a diameter of 137 nm onto the aminated dimples. (6) We convert the carboxylate groups on the silica satellites into amine groups using ethylene diamine. (7) We grow a thin gold shell on top of the spheres by the site-specific adsorption of gold nuclei and subsequent regrowth.

multi-stage silica-particle synthesis process [117] that results in seed particles with a polydispersity index of only 1.002 (see Materials and methods); the templated synthesis of polystyrene colloidal molecules [118], which results in octahedral clusters with a yield as high as 80% [117, 119]; the overgrowth of the silica core followed by removal of the polystyrene spheres [115]; and the regioselective functionalization of the resulting concave dimples in the silica.

The challenge is to attach metal to the resulting functionalized, dimpled, octa-

hedrally symmetric silica particles such that the distance between metal surfaces is controlled to nanometer-scale precision or better. In self-assembly approaches, this precision can be achieved by functionalizing gold nanoshells with a self-assembled monolayer and clustering them with capillary forces [111, 112], but this method yields clusters with many different morphologies. Another self-assembly approach involves attaching DNA-functionalized gold nanoparticles to DNA origami templates [110]. This method also leads to precise control over the separation distance, but it produces clusters with different numbers of particles and morphologies. By contrast, the dimpled templates offer greater control over the morphology, but until now no approach has led to precise control over the separation distance. In previous work, gold satellites were grown directly on the dimpled templates [120]. This approach requires iterative growth and oxidative etching of the gold, which results in the satellites varying in size and shape. Hence the interparticle distances are not well controlled. In the present study, we first attempted to lock pre-synthesized, highly monodisperse, ultra-smooth gold spheres [121] to the dimples, but we obtained a low yield of six-particle clusters, perhaps because of the large density difference between silica and gold.

Therefore, instead of attaching gold directly to the dimples, we pursue a multi-step approach, as shown in steps 5–7 of Fig. 5.1. We first attach silica spheres to the dimples and then grow a gold layer on top of them. We lock highly monodisperse silica particles (polydispersity index 1.001) onto the dimples through amide coupling, building on a previously developed recipe [122]. To fill all the dimples, we use a large excess of these particles (400:1). Then we use a seeded-growth method [123] to grow a gold film of controlled thickness on the silica. Growth occurs only on the silica

satellites and not the central particle because the satellites are functionalized with carboxyl groups, which we can selectively convert to amine groups prior to gold plating. This approach takes advantage of the very low polydispersity of the silica synthesis reaction [124, 117] and the sensitivity of the seeded-growth gold plating technique to precisely control the separation distance between the gold layers. Furthermore, because the silica core size and gold shell thickness can be changed independently, our approach provides independent control over the two geometrical features that control the frequency of the plasmon resonances: the separation distance and the separation-to-diameter ratio [125].

5.3 Characterization of plasmonic nanoclusters

Transmission electron microscopy (TEM) confirms successful synthesis. As shown in Fig. 5.2a, we can control the thickness of the gold shell by changing the amount of gold precursor in the synthesis step. We find that for a shell thickness of about 25 nm, the geometry remains consistent from cluster to cluster (Fig. 5.2b). Elemental mapping using energy-dispersive X-ray analysis (EDX) shows that the gold layer is specifically deposited on each of the six silica satellites, while the central silica particle remains gold-free (Fig. 5.8). The microscope images confirm that the nanoclusters have octahedral symmetry and that the number and approximate positions of the core-shell particles are consistent from cluster to cluster. We estimate the morphology yield to be as high as 80%. This value is determined by the yield of silica/polystyrene colloidal molecules [117, 119] achieved in step 1 of Fig. 5.1, because the rest of the steps are performed with nearly perfect yield. Furthermore, because each step of the

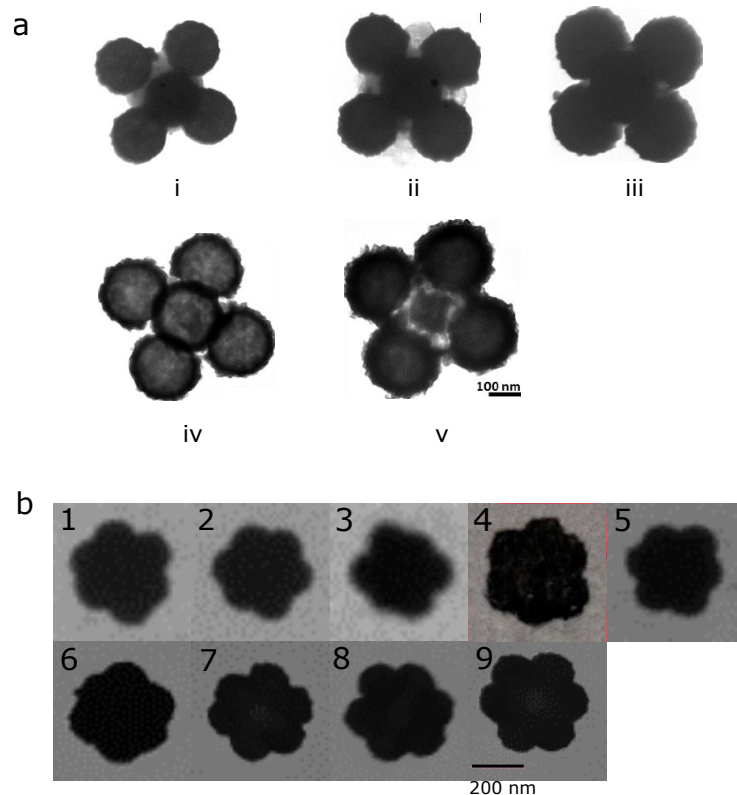


Figure 5.2: **(a)** TEM images of silica/gold clusters with varying gold shell thicknesses, obtained with different amounts of gold precursor: a) 5 mL; b) 10 mL; c) 20 mL; d) 25 mL and e) 35 mL. **(b)** Nine different clusters for the regrowth condition of 25 mL gold precursor.

synthesis is done in bulk, we can scale up the procedure to produce these clusters at gram scales or more.

Because the gold shells are separated by only a few nanometers—too small to measure precisely with TEM—we infer these separation distances and their variation using single-particle spectroscopy and simulation. The plasmon resonances provide the most stringent test of the precision of our technique because they are sensitive to very small changes or variations in the separation [113]. We start by identifying

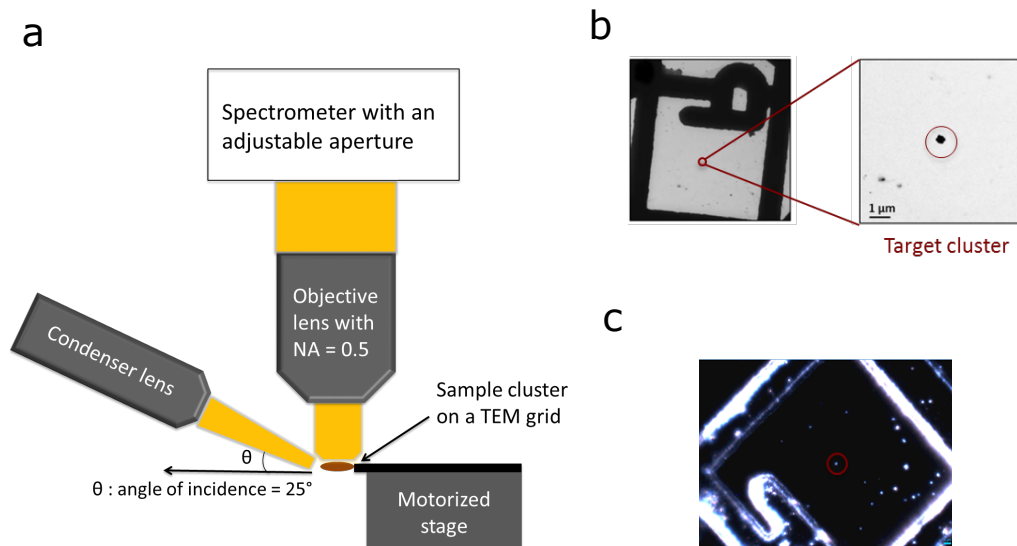


Figure 5.3: Single-particle spectroscopy setup. **(a)** Setup for measuring the spectrum of light scattered from individual nanoclusters. The light source is an unpolarized halogen lamp illuminating the sample at an incidence angle of 65° (25° with respect to the horizontal axis). An objective ($50\times$, $\text{NA} = 0.5$) is placed on top of the grid to collect the scattered light. An adjustable aperture is placed in the optical path of the spectrometer to collect light from only a narrow area (a circle with a diameter of about $1\text{ }\mu\text{m}$) surrounding the cluster. To make sure that clusters are well separated, we dilute the experimental sample. **(b)** TEM image of a target cluster (inside red circle) near marker “P” on TEM grid. **(c)** The same target cluster imaged with the dark-field microscope.

each octahedral cluster on a grid with alphabetical markers using TEM (Fig. 5.3b), then transfer the TEM grid to a microscope stage (Fig. 5.3a). We set the illumination angle such that the objective collects only the light scattered by each nanocluster. After identifying the nanoclusters in this dark-field setup (Fig. 5.3c), we measure the spectrum of scattered light using a spectrometer attached to the microscope.

We find that all nine clusters from Fig. 5.2b show two major peaks, one at $(791.5 \pm 6.5)\text{ nm}$ and the other at $(886.2 \pm 5.9)\text{ nm}$ (Fig. 5.4). Positions of the first

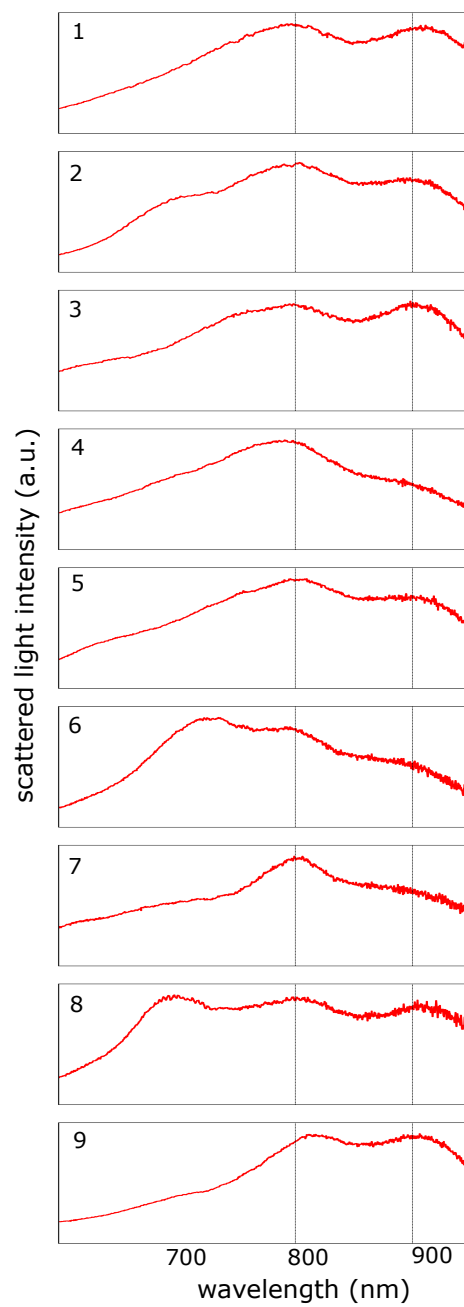


Figure 5.4: Measured spectra of nine individual octahedral clusters.

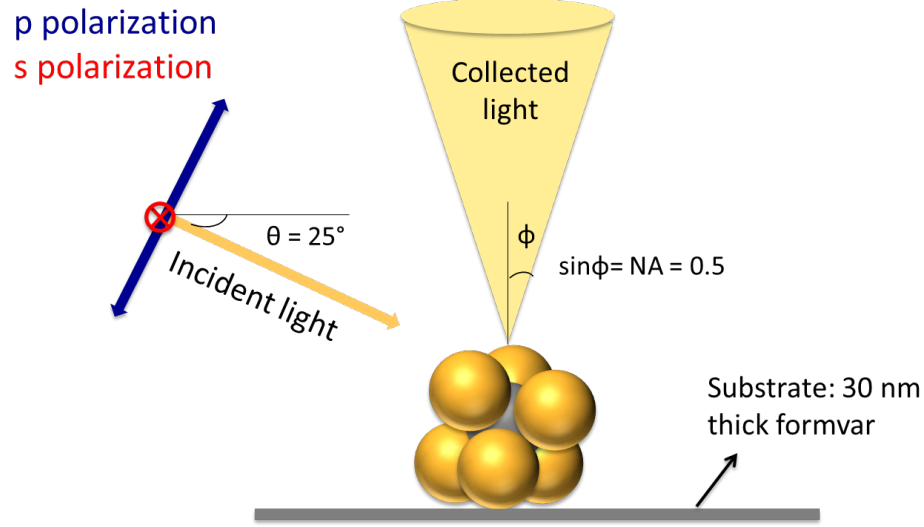


Figure 5.5: Diagram of experimental geometry. Our model accounts for the incidence angle, collection angle, and substrate geometry used in the experiments. To mimic an unpolarized light source, we add the scattered intensity from two orthogonal polarizations.

peaks are at 788.2 nm, 795.0 nm, 790.1 nm, 783.0 nm, 800.7 nm, 783.3 nm, 790.7 nm, 790.0 nm, and 802.8 nm. Positions of the second peaks are at 897.0 nm, 884.1 nm, 884.7 nm, 878.8 nm, 881.2 nm, 888.1 nm, 879.2 nm, 890.4 nm, and 892.2 nm. We identify the peak positions for each cluster by searching for the local maxima in its spectrum. The small uncertainty in peak positions suggests that the separation distance is consistent from cluster to cluster. To make a quantitative statement about how precise this distance is controlled, we first use a model to determine where the resonances come from, then explore how changing the separation distance affects the resonances.

To understand the origin of the scattering peaks, we use finite-difference time-

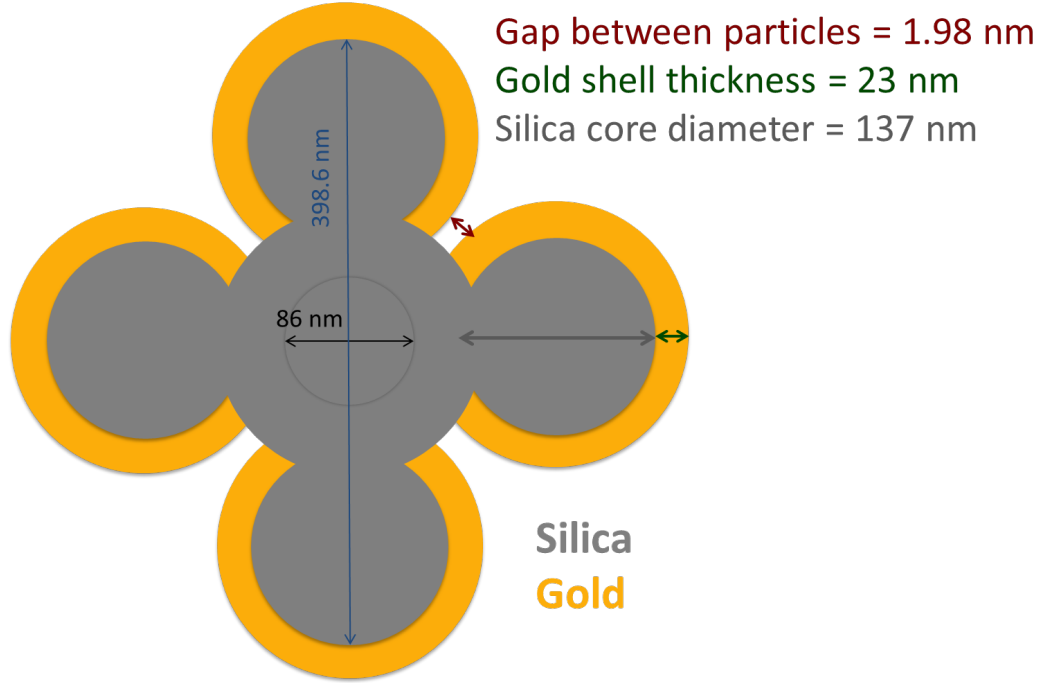


Figure 5.6: Cross-sectional view of the geometry of the octahedral cluster simulated in FDTD, showing the gold shell thickness (23 nm) and separation between the gold layers on the satellites (1.98 nm), both of which were estimated from TEM images of clusters before and after the gold plating step.

domain (FDTD) simulations. Our simulation accounts for the experimental setup (Fig. 5.5)—including, for example, the substrate and the numerical aperture of the lens—and the geometry of the nanoclusters (Fig. 5.6). We coarsely estimate the positions of the particles and the interparticle separations from TEM images, then refine these values to obtain agreement between the simulation and experiment. We find that the model reproduces the peaks at 808.7 nm and 892.5 nm when the interparticle separation is 1.98 nm (Fig. 5.7). Furthermore, by mapping the charge

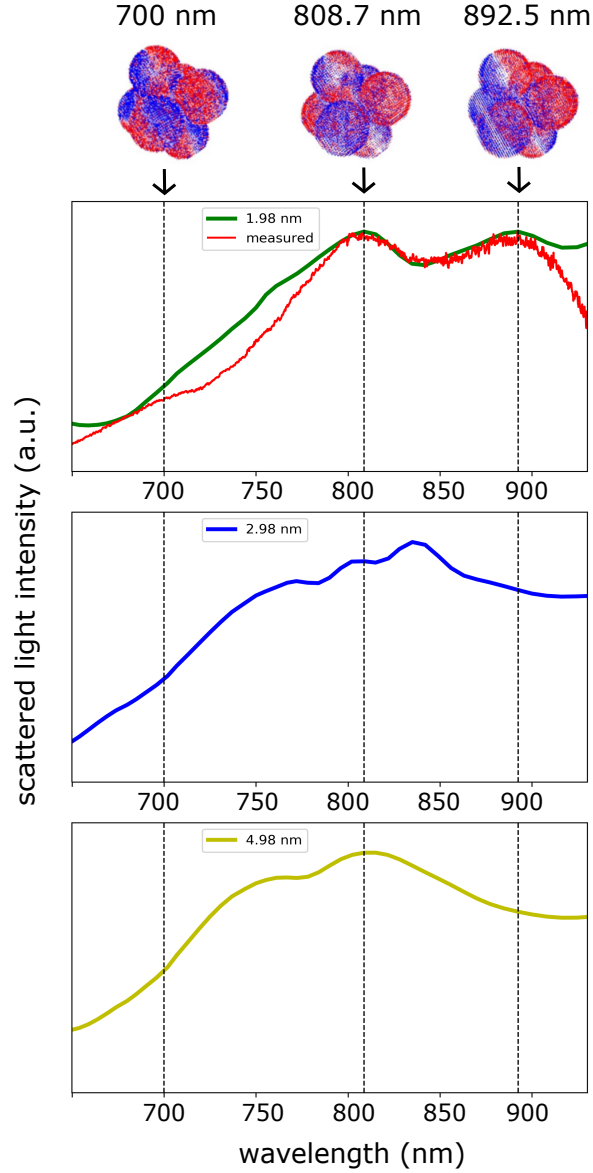


Figure 5.7: Finite-difference time-domain (FDTD) simulations reproduce the locations of the measured peaks. Charge density maps near 700 nm, 808.7 nm, and 892.5 nm show different resonant modes inside the cluster at those wavelengths. As we increase the separation distance between particles, all the peaks shift to shorter wavelengths.

density in the simulations (Fig. 5.7) and calculating the far-field radiation pattern at different wavelengths (Fig. 5.11), we find that the peak at 892.5 nm originates from

an electric dipolar resonance, and the peak at 808.7 nm has an electric quadrupolar component. The model does not explain all the features of the spectra. The peak close to 700 nm, which appears in only three of the nine spectra, and the variation in the heights of the peaks at 808.7 nm and 892.5 nm might arise from variations in the measurement conditions, such as in the incident angle or relative orientation of the cluster with respect to the incident light direction.

With this understanding of the peak origins, we examine how changing the separation distance affects the locations of the resonances. Previous theoretical studies have shown that the dipolar resonances in a tetrahedral cluster are very sensitive to the ratio of the inter-particle separation distance to particle diameter [113]. When this ratio changes from 0.02 to 0.04, the electric dipolar resonance shifts by about 100 nm. From the separation estimated with TEM (2–5 nm) and the overall diameter of the core-shell geometry, we estimate that the separation-to-diameter ratio of our octahedral cluster is between 0.011 and 0.027. Within this range, we expect the resonance peaks to be at least as sensitive as those in the previous study [113].

We use our simulation to confirm this sensitivity. By changing the inter-particle separation from 1.98 nm (shell thickness 23 nm, diameter $137+46 = 183$ nm, separation-to-diameter ratio 0.011) to 4.98 nm (shell thickness 21.5 nm, diameter $137+43 = 180$ nm separation-to-diameter ratio 0.022), the dipolar peak at 892.5 nm blue-shifts about 90 nm (Fig. 5.7) and the higher-order peak at 808.7 nm blue-shifts about 50 nm. The uncertainty in peak positions from experimental measurements is an order of magnitude smaller, 5.9 nm for the dipolar peak and 6.5 nm for the higher-order peak. Assuming a linear relationship between peak positions and interparticle separations, we estimate

the uncertainty in interparticle separation to be 0.2 nm to 0.4 nm. From this result, we conclude that using this synthesis method, very high precision (less than a nanometer) in controlling interparticle separations can be achieved.

To be clear, “nanometer precision” refers to the average distance between the gold layers on the silica satellites. As can be seen in Fig. 5.2a, the gold layers have a roughness that is much larger than a nanometer. This roughness might contribute to the observed variation in amplitude of the peaks from cluster to cluster. However, the consistency of the peak positions from cluster to cluster indicates that the average separation distance is very well controlled. In previous measurements of the spectra of individual nanoclusters [126, 127], the measurements varied from cluster to cluster, while bulk measurements of nanoclusters [128, 129] show spectral broadening arising from the variation in cluster geometry.

5.4 Conclusion

Future work might extend this approach to produce other plasmonic structures, including ones that display a magnetic resonance. To this end, it may be useful to control the dimple geometry of the silica core; by tuning the core size, it is possible to make tetrahedral and dodecahedral geometries [115, 130]. Also, because the core size, shell thickness, and interparticle separation can be tuned independently of one another, there are many ways to tune the positions of the plasmon resonances. Thus the multi-step synthesis scheme is a versatile way of producing “artificial plasmonic molecules” [113].

More generally, our method illustrates the degree to which colloidal morphology can now be controlled through chemistry. The precision of our method stems from the versatility of seeded-growth reactions. These are used to create the highly monodisperse silica particles for the core and satellites, to control the thickness of the gold films, to overgrow the silica core, and to make the octahedral cluster of sacrificial polymer particles that coordinate the central silica core. This last reaction relies on a geometrical effect [19] that results in a narrow distribution of numbers of particles attached to a central core, even when the initial seeds of those particles are randomly distributed on the core surface [131]. A similar process in which spheres adsorb onto a central core—rather than grow on it—is the basis of a recent synthesis method for making patchy colloidal particles with controlled morphology [132]. Like our method, this method uses multiple high-yield synthesis steps to produce large quantities of specific clusters. Such schemes, which resemble the multi-step synthetic schemes used to produce complex molecules from organic reagents, represent a new and emerging paradigm in colloidal materials. They have clear advantages over self-assembly and lithography: they can produce bulk quantities of complex three-dimensional structures in bulk with no annealing required. Our results demonstrate that the multi-step approach can meet even the most stringent requirements for precision over the assembly.

5.5 Materials and methods

5.5.1 Synthesis of spherical silica particles

We use a two-stage protocol [124, 117] to synthesize silica particles. The first stage is the synthesis of pre-seeds. We pour 100 mL of 6 mM L-arginine aqueous solution (purchased from Sigma-Aldrich, 99 %) in a 150 mL double-walled vial equipped with a reflux condenser. When the temperature stabilizes at 60 °C, we add 10 mL tetraethoxysilane (TEOS, Sigma-Aldrich 99 %). We set the magnetic stirring to 150 rpm for a 3 cm cylindrical magnetic stirrer to generate a small and stable vortex and an interface of constant surface area between both phases. The reaction continues until the TEOS (upper phase) fully disappears, typically in two days. We estimate the diameter of the as-obtained silica pre-seeds from TEM imaging and find an average value of 29.2 nm and a polydispersity index (PDI) of 1.01. The dry extract method allows us to determine the silica concentration (25.2 g L^{-1}) and then to calculate the concentration of pre-seeds ($8.8 \times 10^{-17} \text{ L}^{-1}$). In the second stage, we re-grow these silica pre-seeds in a 1 L flask surmounted by a bubbler where 455 mL ethanol (Sigma-Aldrich), 35 mL ammonia (J.T. Baker, 28–30 % in water) and 10 mL pre-seed aqueous dispersion are mixed by magnetic stirring. Then the proper volume of TEOS is added dropwise using a syringe pump at the rate of 0.5 mL h^{-1} to reach a TEOS/silica weight ratio of 83. In such conditions, the diameter of the silica particles increases to 86 nm (PDI = 1.002) and the final concentration of the silica particles is $1.47 \times 10^{-16} \text{ L}^{-1}$. To achieve 137 nm silica particles (PDI = 1.001), we use this last silica particle dispersion and add TEOS dropwise again to reach a TEOS/silica weight ratio of 20.

5.5.2 Functionalization of silica particles with carboxylic acid groups

We modify the 137 nm silica particle surfaces with amino groups and then derivatize into carboxylic ones following a previously reported protocol [133]. We carry out the reaction just after the regrowth stage, in the same reacting medium, where we add an amount of APTES (aminopropyltriethoxysilane, Sigma-Aldrich, 98 %) corresponding to 20 functional groups per nm² of silica surface. We stir the dispersion for 12 h at room temperature. Then we add a volume of glycerol (Sigma-Aldrich, 99 %) corresponding to 10 % of the dispersion volume. We evaporate ethanol and water using a rotary evaporator set at 90 °C. We heat the dispersion in glycerol, in an oil bath set at 105 °C for a subsequent 2 h thermal treatment under the vacuum produced by a rotary vane pump (RV5 from Edwards). Finally, we wash the particles by performing four cycles of centrifugation/redispersion in ethanol (12,000*g* for 20 min). We check the efficiency of the reaction by ζ -potential measurements performed in water, which show a value of $(+35 \pm 3)$ mV in the 4–10 pH range.

Next, we transfer the aminated silica particles to dimethylformamide (DMF) by performing three centrifugation/redispersion cycles (12,000*g* for 20 min). Between the second and third cycle, we add an amount of triethylamine (TEA, Sigma-Aldrich, 99.5 %) corresponding to 50 functional groups per nm² of silica surface. We adjust the volume to 50 mL and transfer the dispersion into a round-bottom flask placed in an oil bath set at 60 °C for dehydration for 2 h under the vacuum of the rotary vane pump. We add an amount of succinic anhydride (Sigma-Aldrich, >99 %) corresponding to 50 functional groups per nm² of silica surface and let react overnight at 60 °C. We

wash the particles by two centrifugation/redispersion cycles in ethanol and three extra ones in DMF (12,000*g* for 20 min). We add an amount of TEA corresponding to 50 functional groups per nm² before the last washing cycle, and we dehydrate the last dispersion under the vacuum of the rotary vane pump. We check the efficiency of the reaction by ζ -potential measurements performed in water, which show a value of $(+35 \pm 5)$ mV in the 5–10 pH range, and by infrared absorption spectroscopy, which shows the presence of amide and carboxylate groups in stretching bands at 1650 cm⁻¹ and 1730 cm⁻¹, respectively.

5.5.3 Synthesis of dimpled silica particles from silica/polystyrene octahedra

We prepare batches of silica/polystyrene octahedra made of a central 86 nm silica core and six polystyrene (PS) satellite nodules by seeded-growth emulsion polymerization of styrene, according to a previously developed procedure [117, 119]. Briefly, this procedure consists of the emulsion polymerization of styrene performed in the presence of the 86 nm silica particles, which are surface modified with methacryloxymethyltriethoxysilane (MMS, ABCR, 98 %).

The MMS modification reaction is carried out just after the silica regrowth stage, in the same reacting medium, where we add an amount of MMS corresponding to 0.5 functional groups per nm² of silica surface. We let react under stirring for 3 h at room temperature before heating to 90 °C for 1 h under reflux of ethanol. We concentrate the dispersion with the rotary evaporator to remove ethanol and ammonia and replace them with water. Then we let the dispersion cool down at room temperature and

dialyze against water for three days. We measure the particle concentration by the dried extract method.

In a 250 mL three-neck flask, equipped with a stirring anchor and a condenser surmounted by a bubbler, we introduce water, the 86 nm silica seed dispersion (concentration $7.3 \times 10^{15} \text{ L}^{-1}$), and a surfactant mixture (3 g L^{-1}) made of Symperonic NP30 (95 % w/w) and sodium dodecyl sulfate (SDS, Sigma-Aldrich, >90 %, 5 % w/w). We thoroughly deaerate the dispersion by bubbling nitrogen through it while stirring (170 rpm). We emulsify by adding styrene (Sigma-Aldrich, 99 %, 100 g L^{-1}) at 250 rpm for 15 min. We carry out the polymerization at 70°C after addition of sodium persulfate (Sigma-Aldrich, 99 %, 0.5 % w/w with respect to styrene). After 6 h, the monomer-to-polymer conversion is 80 % as determined by the dried extract method. We characterize the sample by TEM and determine statistically that it consists of octahedra with a morphology yield higher than 80 %. The average diameter of the PS satellites is 150 nm.

We overgrow the silica cores using a previously reported method [115]. We prepare a mixture of 450 mL ethanol and 35 mL ammonia (1 M) and first add a volume of the polymerization medium to fix the octahedron concentration to $1.5 \times 10^{14} \text{ L}^{-1}$. Then we add 4.5 mL TEOS (10 % v/v in ethanol) at a rate of 1 mL h^{-1} . We make the silica surface hydrophobic by adding a volume of propyltrimethoxysilane (PTMS, Sigma-Aldrich, >98 %) corresponding to 50 functional groups per nm^2 of the silica surface area. We complete the reaction under stirring at ambient temperature for 12 h. Finally, we wash the particles by performing three cycles of centrifugation ($12,000g$ for 20 min) and redispersion in ethanol. TEM experiments show that the diameter of

the silica core increases from 86 nm to 145 nm.

To dissolve the PS satellites, we add a volume of DMF equal to 10 % of the total volume. Subsequently we heat the dispersion to 70 °C and partially evaporate it under vacuum using a rotary evaporator. Then we increase the temperature to 90 °C and let the evaporation continue until the dispersion changes from white to almost transparent. To remove the dissolved PS, we perform three cycles of centrifugation/redispersion in THF (10,000*g* for 20 min).

5.5.4 Amination of the residual PS macromolecules at the bottom of the dimples

For this procedure, we use a previously reported recipe [116]. Briefly, after transferring the as-prepared dimpled silica particles in chloroform, we add butyl chloromethyl ether in chloroform (3 M; 5 mL) and 0.3 mL tin tetrachloride (SnCl_4 , Sigma-Aldrich, >99 %). We set the temperature to 45 °C and then age the mixture overnight. Finally we wash the nanoparticles using three cycles of centrifugation/redispersion (5,000*g* for 15 min) in aqueous HCl solution (4 % w/w) and then in water/ethanol (50/50 w/w) before redispersion in 20 mL DMF. We perform the amination using 10^{13} chloromethylated silica particles in DMF and 3 mL ethylene diamine (Fluka, 99.5 %), such that the ethylene diamine is in excess to minimize cross-linking. We heat the system to 90 °C and let the reaction proceed overnight under stirring. We wash the nanoparticles using two cycles of centrifugation/redispersion (12,000*g* for 20 min) in ethanol and two additional cycles in water. After having protonated the amino groups with a few drops of HCl, we centrifuge the dispersion and redisperse the particles in water.

Lastly, we transfer the aminated dimpled silica particles into DMF by performing two cycles of centrifugation/redispersion (12,000*g* for 20 min). We add an amount of TEA corresponding to 50 functional groups per nm² of surface of a sphere of similar diameter and we wash the solution one more time with DMF. Finally, we remove the remaining water from the dispersion by heating at 50 °C under stirring and vacuum generated by a rotary vane pump for 1 h.

5.5.5 Synthesis of silica/silica octahedra

To assemble the 137 nm carboxylated spherical silica particles onto the 145 nm aminated dimpled silica particles, we use a peptidic coupling reaction. We perform the reaction in DMF, activating the carboxylate groups with ethyl chloroformate (ECF, Sigma-Aldrich, >97 %) used in exact stoichiometry, avoiding thoroughly the presence of water, and efficiently deprotonating the reactive groups with triethylamine (TEA).

In a 1.5 mL Eppendorf tube, we introduce the DMF dispersion of carboxylated silica particles and an amount of ECF corresponding to 4 functional groups per nm² of silica surface, mix on a vortexer, and homogenize on a roller mixer for 2 min. Then we add the DMF dispersion of aminated dimpled silica particles in excess, such that there are 400 carboxylated particles for each aminated dimpled ones, and we let the assembly proceed for 30 min on the roller mixer. We transfer the dispersion to 40 mL water (containing 0.1 mL TEA) and attempt to selectively remove the excess of carboxylated particles by performing three centrifugation/redispersion cycles (500*g* for 20 min). We check the assembly success and silica/silica octahedron morphology by TEM.

5.5.6 Gold decoration of silica satellites of the silica/silica octahedra

We grow a gold shell specifically onto the silica satellites by first turning the carboxylate groups into amino ones, then adsorbing tiny gold nanoparticles (diameter of 2–5 nm prepared by following a previously developed recipe [134]) selectively on the satellites. A gold plating solution (GPS) prepared according to a previously reported protocol [123] is then used to grow a gold shell on the gold-seed-covered satellites.

Because the carboxylate groups are deactivated at the time of the purification step in water, we re-activate them by transferring them into DMF and adding ECF under conditions previously described. After 5 min, we add an amount of ethylene diamine corresponding to 50 functional groups per nm² of the silica satellite surface and let the mixture react overnight. Then we wash the particles by three centrifugation/redispersion cycles in water (2,000*g* for 10 min), acidify using a few drops of HCl to protonate the amino groups, and wash one more time with water.

In parallel, we prepare the tiny gold seeds in a 500 mL flask by introducing 227.5 mL water, 7.5 mL aqueous solution of NaOH (Sigma-Aldrich, 98 %, 0.2 M) and 5 mL tetrakis(hydroxymethyl)phosphonium chloride (THPC, Aldrich, 80 %) aqueous solution (120 μ L in 10 mL). After homogenization for 15 min under stirring, we quickly inject 10 mL HAuCl₄ (25 mM, Sigma-Aldrich, 99.9 %). The solution turns from pale yellow to brown in a few seconds, indicating the formation of gold nanoparticles.

We put these tiny gold nanoparticles (30 mL) in contact with the silica/silica octahedra (1 mL) by mixing both dispersions, and we let the selective adsorption proceed over a roller mixer for at least 4 h. We wash the particles and remove excess

gold seeds by three centrifugation/redispersion cycles in water (500*g* for 20 min).

To make the GPS, we prepare a 10 mL stock solution of gold precursor from HAuCl₄ (25 mM) and store it in the dark at 4 °C. In a 100 mL flask, we mix 8 mL gold stock solution and 300 mg potassium carbonate and then fill the flask to a total volume of 100 mL with water. We stir the solution overnight at 4 °C.

In a 50 mL falcon tube, we introduce the gold decorated silica/silica octahedra (0.5 mL), PVP solution (10 mL, 10 g L⁻¹), the GPS solution (25 mL), and formaldehyde (1.25 mL). We let the reaction proceed for at least 12 h over a roller mixer. Then we wash the nanoparticles using three cycles of centrifugation (3,000*g* for 15 min) and redispersion in water. To tune the gold shell thickness, we vary the amount of GPS solution (X mL) and formaldehyde (X/20 mL) where X is the value of targeted shell thickness in nanometer. We vary the value of X from 5 to 35 to achieve clusters with different shell thicknesses as shown in Fig. 5.2a.

5.5.7 Characterization techniques

Transmission electron microscopy (TEM). We perform TEM measurements using a Philips CM20 microscope that operates at 75 kV. We prepare the samples by depositing one drop of the colloidal dispersion on a conventional carbon-coated copper grid. We then air-dry the grids at room temperature and store in a closed box to prevent dust accumulation.

Scanning transmission electron microscopy (STEM). We perform STEM measurements coupled with energy dispersive X-ray spectroscopy (EDX) using a JEOL

2200 FS equipped with a field emission gun which operates at 200 kV (PLACAMAT, UMS 3626 CNRS/Univ. Bordeaux). STEM-EDX images are shown in Fig. 5.8.

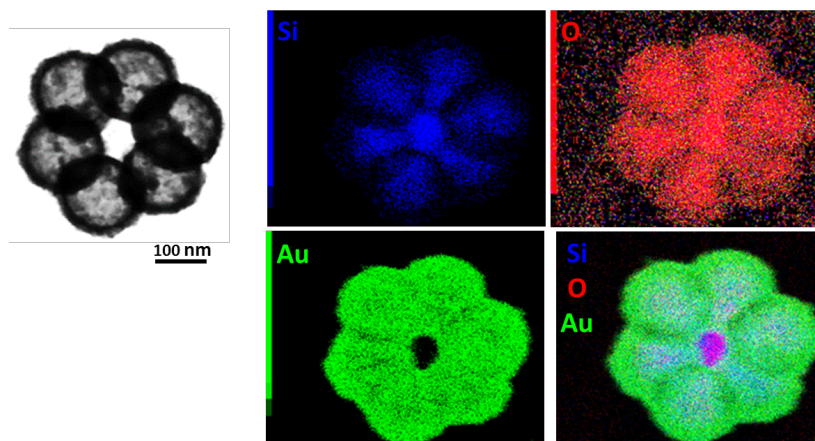


Figure 5.8: STEM-EDX elemental mapping of the gold clusters: bright field TEM image (top left) and silicon, oxygen, gold and superimposed EDX maps evidencing the core-shell morphology of the six satellites.

Single-particle dark-field spectroscopy. To prepare a sample for single-particle spectroscopy, we mix a dispersion of 10 μL of the gold-decorated octahedra with 450 μL of ultrapure deionized water (obtained from a Millipore Synthesis) in an Eppendorf tube. We homogenize the dispersion using a vortexer and an ultrasonic bath. We deposit 3 μL of this suspension on a TEM grid (Electron Microscopy Sciences, model number LF200) and let it dry. The TEM grids contain squares with distinct alphabetical markers and are covered with a thin layer of Formvar, a hydrophobic polymer. After drying the suspension on the grid, we observe the sample with a TEM and identify the locations of octahedral clusters using the alphabetical markers on the TEM grid. Finally, we transfer the grids to the spectroscopy setup.

In the dark-field setup, we use an unpolarized white light beam from a halogen goose neck lamp (supplied by Cole Parmer, 41723-Series high intensity illuminator). We focus the beam on the sample using a 20 \times long working distance Olympus objective. The incidence angle of light is about 65 $^\circ$ with respect to the direction perpendicular to the sample. This oblique incidence angle ensures that only the scattered light passes through the collection objective. We mount the sample on a rotation stage which is placed on a motorized stage connected to the microscope-spectrometer setup (LabRAM HR Evolution Raman spectrometer from HORIBA Scientific). We collect scattered light from the sample using a 50 \times long working distance Olympus objective with a numerical aperture of 0.5. We use an adjustable aperture situated in the optical path of the spectrometer to collect scattered light from only the surroundings of one cluster, with an area of approximately 1 μm^2 .

We measure the spectrum of scattered light from individual clusters by subtracting the signal from the background and then normalizing by the incident light spectrum:

$$I = \frac{I_{\text{sc}} - I_{\text{bg}}}{I_{\text{inc}}}, \quad (5.1)$$

where I_{sc} is the measured intensity of the scattered light *with* a cluster in the field of view and I_{bg} is the measured intensity of the scattered light *without* a cluster. I_{inc} is the intensity of incident light recorded from a Spectralon diffuse reflectance standard (supplied by Labsphere).

5.5.8 Modeling optical properties of plasmonic nanoclusters

We use the commercial package Lumerical to perform finite-difference time-domain (FDTD) simulations of scattering from the nanoclusters. We use a total-field-scattered-

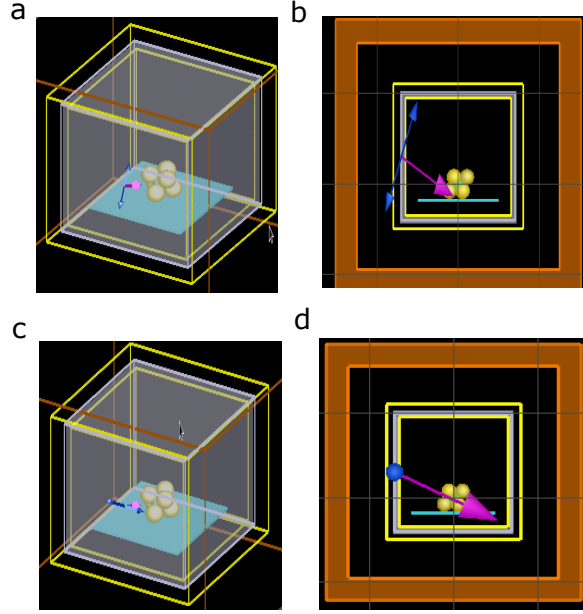


Figure 5.9: (a) 3D view of the simulation setup for p -polarized light. (b) Sideview of the simulation setup for p -polarized light. (c) 3D view of the simulation setup for s -polarized light. (d) Sideview of the simulation setup for s -polarized light.

field (TFSF) implementation, which allows us to separate the scattered field from the incident field. We model a cluster by implementing the octahedral geometry with the approximate parameters measured from TEM images. To replicate the experimental setup, we place the cluster on a substrate (thickness 30 nm, refractive index 1.5) and implement an incidence angle of 25° . The simulation setup is shown in Fig. 5.9.

Fig. 5.10 shows a cross-sectional view and the mapping of refractive index across the model of the cluster. It shows the presence of the gold shells surrounding spherical silica particles. From simulations, we measure the scattered light at coordinates in the far-field, a centimeter away from the cluster (approximately the distance between the cluster and objective lens in experiment). We implement the numerical aperture by

defining a cone with a cone angle of 30° and integrating the scattered light intensity over the area of the base of the cone. To measure the response to our unpolarized light source, we perform simulations separately with *s*-polarized and *p*-polarized incident light and take their sum. To plot the far-field radiation patterns as shown in Fig. 5.11, we calculate the intensity of scattered light along the perimeter of a circle with a diameter of 1 m placed in three different planes: the *XY*, *YZ*, and *XZ* plane.



Figure 5.10: Map of refractive index in a cross-sectional plane of an octahedral nanocluster modeled in simulation.

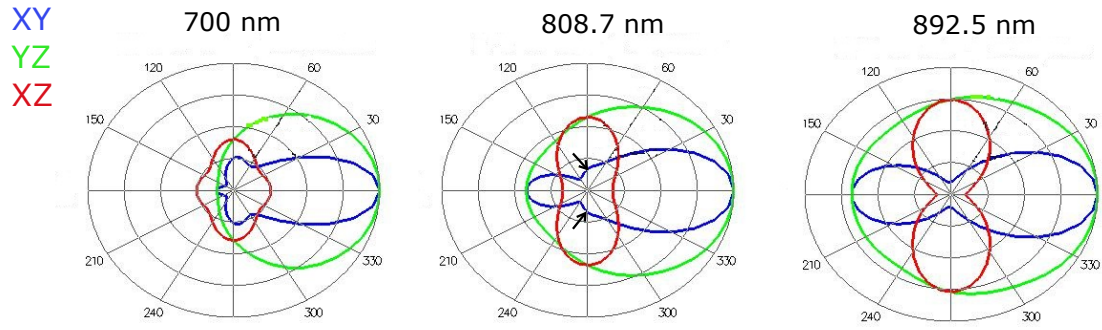


Figure 5.11: Far-field radiation pattern of a modeled nanocluster at three different wavelengths. The incident light polarization is aligned with the x -axis. The patterns at 892.5 nm represent electric dipolar radiation and the patterns at 700 nm represent electric quadrupolar radiation, in both XY and XZ planes. At the wavelength of 808.7 nm, the quadrupolar mode shows up in the XY plane (shown by the black arrows).

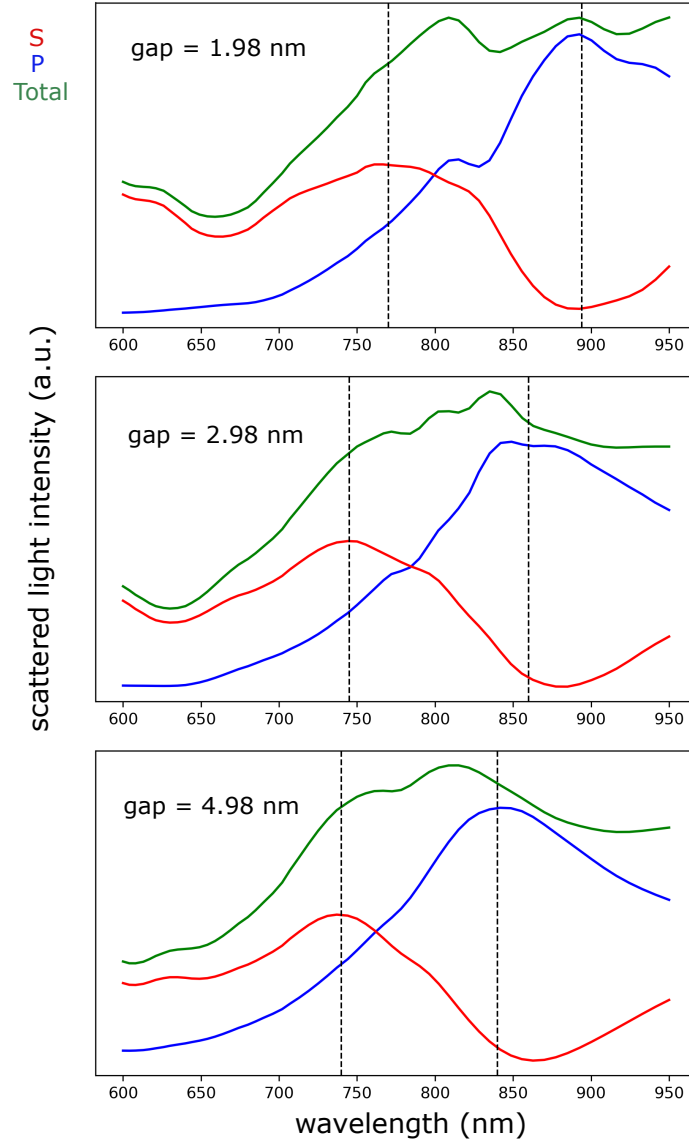


Figure 5.12: Scattering spectra for clusters with different gaps. The total intensity is the sum of the intensity of s -polarized and p -polarized light. We find one dominant peak for each of the polarizations. For a 1.98 nm gap geometry, the peak for s -polarized light is around 770 nm and the peak for p -polarized light is around 892.5 nm. As the gap increases from 1.98 nm to 4.98 nm, both of the peaks for s -polarized and p -polarized light blue-shift. As a result, the peaks in the total scattered light spectra (shown by green plot) also blue-shift.

Chapter 6

Conclusion and outlook

The experimental systems in this thesis demonstrate progress toward a general understanding of packing and parking of colloidal spheres and potential applications. Experiments on close packing on a cylinder through weak colloidal interactions confirm that chiral crystals and chiral line-slip defects emerge owing to the cylindrical geometry. Moreover, we observe new structural features, such as kinked line-slip defects with fractional vacancies. This observation led to our investigation on crystallization dynamics, and we find a close connection between morphology and crystal growth dynamics. Inspired by the structures of snowflakes and rock crystals, studies on crystal morphology and growth dynamics have been an intensive area of study for more than a century now [135]. Our results, which indicate that geometry of the substrate plays a crucial role in both morphology and growth dynamics, might inspire future investigations on other substrate geometry.

Our experiments on random parking on a cylinder through strong colloidal interactions show that cylinders with higher curvature have lower surface coverage compared

to a surface with no curvature. Our theory and simulations confirm that this is a geometric effect and not just a kinetic and energetic one.

Experiments on multi-step colloidal synthesis demonstrate that colloidal packing can be used to design patchy structures with well defined symmetry, and those structures can be coated with plasmonic materials. This result shows that by combining effects of substrate geometry with colloidal chemistry, it is possible to design structures with precise geometry at the nanoscale.

Below I outline opportunities of future investigations that have been inspired by our findings.

6.1 Future directions for self-assembly on a cylinder

6.1.1 Frustration at kinks

We showed in Chapter 2 that the kinked line-slip defects stay kinetically trapped for hours even when they have low energy with only one fractional vacancy. This result can be attributed to the shape of the kink itself. Preliminary results from simulation show that the line-slip geometry can vary depending on the sphere-to-cylinder size ratio and the chiral angle of the crystal. As shown in Fig. 6.1, a line-slip defect with smaller gaps at the slip has a larger angle at its kink, and a line-slip defect with larger gaps at the slip has a smaller angle at its kink. The small angle at the kink can make it hard for the particle at kink to move because doing so requires stretching the crystal or moving out of the plane. This effect should be verified and measured in experiment, which will require confocal images with higher spatial and temporal resolution.

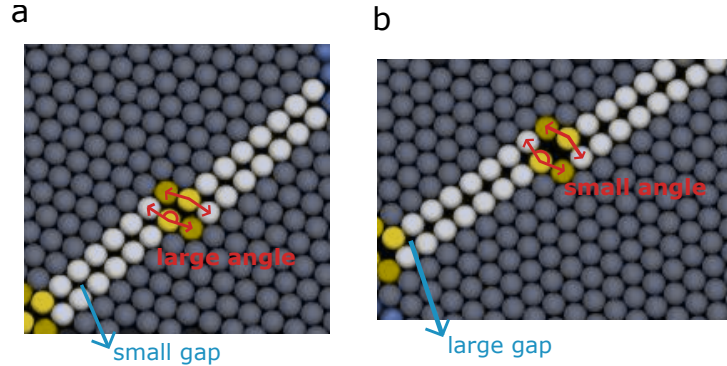


Figure 6.1: **(a)** Line-slip defect with small gap at the slip and large angle at the kink. The large angle enables particles at the kink to hop more often. **(b)** Line-slip defect with large gap at the slip line and small angle at the kink. The small angle does not enable particles at the kink to hop often.

6.1.2 Design of different interactions

All our experiments and simulations were carried out with a fixed range of interaction potential. Frustration at the kinks can be attributed to the short interaction range. Future investigations might address how the structure and dynamics of kinked line-slip defect vary with the range of interaction. Moreover, our crystallization scheme driven by depletion does not allow crystallization on a cylinder with a diameter less than a particle diameter. More specific interactions, such as DNA-mediated attraction, could make it possible to study crystallization at small size ratios, thereby providing an opportunity to compare structures directly with previous simulations [1, 2].

6.1.3 Sublimation dynamics at kinked line-slip defects

Previous research has examined the sublimation dynamics of colloidal crystals [136] and premelting at dislocations and grain boundaries [137]. How the kinked

line-slip defect contributes to sublimation and whether premelting is observed at the defect are both interesting questions for future investigation. Experiments to answer these questions can be done with our current system. At high temperature, the size of SDS micelles shrinks, reducing the depth of interaction potential and causing melting [136]. We present preliminary results for such a system in Fig. 6.2, in which at high temperature, partial melting of a crystal with line-slip defect is observed.

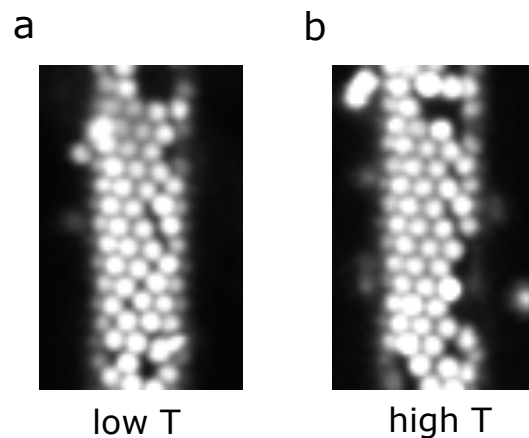


Figure 6.2: **(a)** Crystal with a kinked line-slip defect at room temperature. **(b)** At high temperature (60°C), the crystal starts to sublime (bottom right corner); half of the defect disappears as the crystal starts to sublime.

6.1.4 Self-assembly on dynamic substrate

All of the experiments presented in this thesis consider a cylinder and spheres with fixed size and shape. However, changing the cylinder diameter geometry dynamically [138] or bending the substrate [2] both can affect the dynamics of crystal defects. One approach to examine such dynamics is to use thermoresponsive colloidal spheres such as poly-(*N*-isopropylacrylamide) microgel spheres that change diameter in response

to temperature. Such a system has been used previously to examine packing inside thin cylinders [22]. One might use this system to observe dynamics of kinked line-slip defects.

6.1.5 Chirality and optical properties

Crystallization on a cylinder spontaneously results in chiral crystals and chiral defects. Because the chirality depends only on the size ratio of the cylinder to the spheres, the crystallization process can be used to design structures at any lengthscale. The field of chiral metamaterials requires 3D chiral nanoscale building blocks containing plasmonic nanoparticles. To date, most of the promising designs focus on producing single helices using lithography [48] or DNA origami [139, 42]. The chiroptical properties of our chiral crystals, which resemble carbon nanotubes have not been investigated. Thus there are opportunities for both future experiments and modeling of optical properties.

6.2 Self-assembly in different geometry

6.2.1 Crystallization on a cone

There are almost unlimited possibilities for the geometries on which we can study self-assembly. An immediate opportunity is to investigate colloidal self-assembly on the surface of a cone. A cone has a zero Gaussian curvature just like a cylinder (except at its tip), but its mean curvature varies along its length. In contrast to a cylinder, a single crystal with fixed chirality will fail to form on the surface of a cone without

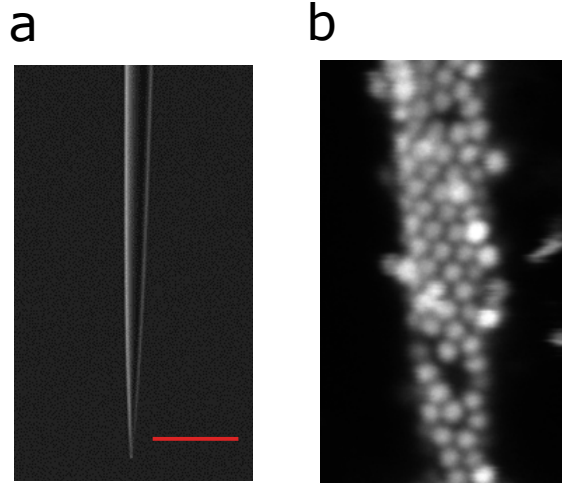


Figure 6.3: **(a)** Image of a cone fabricated by pulling a glass capillary tube. The red line shows a scale bar with a length of $10\text{ }\mu\text{m}$. **(b)** Confocal micrograph of colloidal particles self-assemble on the surface of a cone through depletion interactions.

defects or fractional vacancies, except on cones with very specific cone angles. We show in Fig. 6.3 that it is possible to design an experimental system where colloidal spheres self-assemble on a cone surface using the same colloidal interactions that we used for cylinders.

6.2.2 Self-assembly with bidisperse colloidal particles

Another way to induce geometric frustration is to use a bidisperse colloidal system. In Fig. 6.4 we show preliminary results for crystallization of colloidal spheres on a flat surface using two different sizes of colloidal particles, 700 nm (green particles) and 800 nm (red particles). As we change their number ratio, the structure of the crystal changes. For high enough ratios (90:1 and 9:1) the 800 nm particles act as impurities in the crystal, influencing the crystal grain size (Fig. 6.4a,d and 6.4b,e). For equal

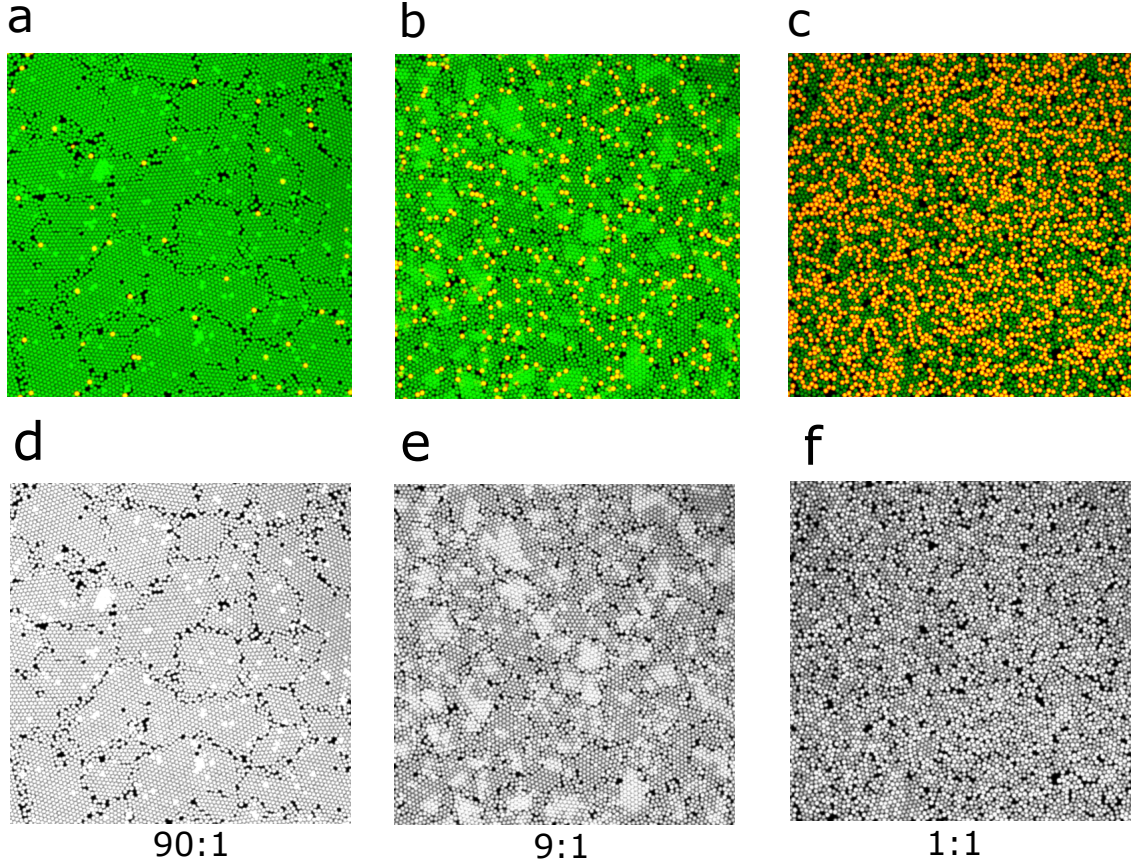


Figure 6.4: Confocal microscope images of a colloidal crystal made of particles with two different sizes, 700 nm (green) and 800 nm (red). The top panel shows variation in structure at their number ratios **(a)** 90:1 **(b)** 9:1, and **(c)** 1:1. The bottom panel shows the same images in black and white. Crystals in **(e)** have smaller grains and more grain boundaries. They also have more second layers (the bright white spots on top of the crystals) compared to the crystals in **(d)**. In contrast, the crystals in **(f)** have no long-range order and, as a result, do not form a second layer.

numbers of both sizes, we end up with short-ranged crystalline order (Fig. 6.4c,f).

The effects of impurities on defects such as grain boundaries in bulk colloidal crystals have been investigated to some extent [56, 57]. However, how impurities affect defects induced by geometric frustration, such as a line-slip defect, is not known and leaves ample opportunities to explore.

6.3 Final remarks

Inspired by the diversity of structures in nature from flowers to viruses, we explored self-assembly of colloidal particles under different conditions of geometry. There are still numerous unexplored questions in this area of study that have not been addressed even with the colloidal model system. How our understanding of the model system relates to the reality of structures present in nature is another question yet to be investigated. Nevertheless, the colloidal system provides opportunities to design new materials because of their promise in bottom-up self-assembly. Being part of a research project with both inspiration from nature and real-world applications has been a great privilege for me, and I look forward to the future possibilities in this area of research.

Bibliography

- [1] Galen T. Pickett, Mark Gross, and Hiroko Okuyama. Spontaneous Chirality in Simple Systems. *Physical Review Letters*, 85(17):3652–3655, October 2000.
- [2] D. A. Wood, C. D. Santangelo, and A. D. Dinsmore. Self-assembly on a cylinder: a model system for understanding the constraint of commensurability. *Soft Matter*, 9(42):10016, 2013.
- [3] Tara D. Iracki, Daniel J. Beltran-Villegas, Shannon L. Eichmann, and Michael A. Bevan. Charged Micelle Depletion Attraction and Interfacial Colloidal Phase Behavior. *Langmuir*, 26(24):18710–18717, December 2010.
- [4] Aysen Tulpar, Vivek Subramanian, and William Ducker. Decay Lengths of Double-Layer Forces in Solutions of Partly Associated Ions. *Langmuir*, 17(26):8451–8454, December 2001.
- [5] Lakshman Samaranayake. *Essential Microbiology for Dentistry*. Elsevier, 3rd edition, 2006.
- [6] Michal Cieřla and Robert M. Ziff. Boundary conditions in random sequential adsorption. *Journal of Statistical Mechanics: Theory and Experiment*, 2018(4):043302, April 2018.
- [7] Cris Kuhlemeier. Phyllotaxis. *Trends in Plant Science*, 12(4):143–150, April 2007.
- [8] Matthew F. Pennybacker, Patrick D. Shipman, and Alan C. Newell. Phyllotaxis: Some progress, but a story far from over. *Physica D: Nonlinear Phenomena*, 306:48–81, June 2015.
- [9] Antoni Luque and David Reguera. The Structure of Elongated Viral Capsids. *Biophysical Journal*, 98(12):2993–3003, June 2010.
- [10] Vinothan N. Manoharan. Colloidal matter: Packing, geometry, and entropy. *Science*, 349(6251), August 2015.

-
- [11] P. N. Pusey and W. van Megen. Phase behaviour of concentrated suspensions of nearly hard colloidal spheres. *Nature*, 320(6060):340–342, March 1986.
- [12] U. Gasser, Eric R. Weeks, Andrew Schofield, P. N. Pusey, and D. A. Weitz. Real-Space Imaging of Nucleation and Growth in Colloidal Crystallization. *Science*, 292(5515):258–262, April 2001.
- [13] Ziren Wang, Feng Wang, Yi Peng, Zhongyu Zheng, and Yilong Han. Imaging the Homogeneous Nucleation During the Melting of Superheated Colloidal Crystals. *Science*, 338(6103):87–90, October 2012.
- [14] Eric R. Weeks, J. C. Crocker, Andrew C. Levitt, Andrew Schofield, and D. A. Weitz. Three-Dimensional Direct Imaging of Structural Relaxation Near the Colloidal Glass Transition. *Science*, 287(5453):627–631, January 2000.
- [15] Sho Asakura and Fumio Oosawa. On Interaction between Two Bodies Immersed in a Solution of Macromolecules. *The Journal of Chemical Physics*, 22(7):1255–1256, July 1954.
- [16] P. D. Kaplan, J. L. Rouke, A. G. Yodh, and D. J. Pine. Entropically Driven Surface Phase Separation in Binary Colloidal Mixtures. *Physical Review Letters*, 72(4):582–585, January 1994.
- [17] Richard A. L. Jones. *Soft Condensed Matter*, volume 6 of *Oxford Master Series in Condensed Matter Physics*. Oxford University Press, 1st edition, 2002.
- [18] G. Meng, J. Paulose, D. R. Nelson, and V. N. Manoharan. Elastic Instability of a Crystal Growing on a Curved Surface. *Science*, 343(6171):634–637, February 2014.
- [19] Nicholas B. Schade, Miranda C. Holmes-Cerfon, Elizabeth R. Chen, Dina Aronzon, Jesse W. Collins, Jonathan A. Fan, Federico Capasso, and Vinothan N. Manoharan. Tetrahedral Colloidal Clusters from Random Parking of Bidisperse Spheres. *Physical Review Letters*, 110(14):148303, April 2013.
- [20] E. C. Oğuz, R. Messina, and H. Löwen. Helicity in cylindrically confined Yukawa systems. *EPL (Europhysics Letters)*, 94(2):28005, April 2011.
- [21] A. Mughal, H. K. Chan, and D. Weaire. Phyllotactic Description of Hard Sphere Packing in Cylindrical Channels. *Physical Review Letters*, 106(11), March 2011.
- [22] M. A. Lohr, A. M. Alsayed, B. G. Chen, Z. Zhang, R. D. Kamien, and A. G. Yodh. Helical packings and phase transformations of soft spheres in cylinders. *Physical Review E*, 81(4), April 2010.

-
- [23] Gaoxiang Wu, Hyesung Cho, Derek A. Wood, Anthony D. Dinsmore, and Shu Yang. Confined Assemblies of Colloidal Particles with Soft Repulsive Interactions. *Journal of the American Chemical Society*, 139(14):5095–5101, April 2017.
 - [24] Z Adamczyk and P Belouschek. Localized adsorption of particles on spherical and cylindrical interfaces. *Journal of Colloid and Interface Science*, 146(1):123–136, October 1991.
 - [25] A. R. Bausch. Grain Boundary Scars and Spherical Crystallography. *Science*, 299(5613):1716–1718, March 2003.
 - [26] Peter Lipowsky, Mark J. Bowick, Jan H. Meinke, David R. Nelson, and Andreas R. Bausch. Direct visualization of dislocation dynamics in grain-boundary scars. *Nature Materials*, 4(5):407, May 2005.
 - [27] Rodrigo E. Guerra, Colm P. Kelleher, Andrew D. Hollingsworth, and Paul M. Chaikin. Freezing on a sphere. *Nature*, 554(7692):346–350, February 2018.
 - [28] Antoni Luque, David Reguera, Alexander Morozov, Joseph Rudnick, and Robijn Bruinsma. Physics of shell assembly: Line tension, hole implosion, and closure catastrophe. *The Journal of Chemical Physics*, 136(18):184507, May 2012.
 - [29] Thomas C. T. Michaels, Mathias M. J. Bellaiche, Michael F. Hagan, and Thomas P. J. Knowles. Kinetic constraints on self-assembly into closed supramolecular structures. *Scientific Reports*, 7(1):12295, December 2017.
 - [30] A. Mughal, H. K. Chan, D. Weaire, and S. Hutzler. Dense packings of spheres in cylinders: Simulations. *Physical Review E*, 85(5), May 2012.
 - [31] J. Winkelmann, B. Haffner, D. Weaire, A. Mughal, and S. Hutzler. Simulation and observation of line-slip structures in columnar structures of soft spheres. *Physical Review E*, 96(1), July 2017.
 - [32] Limin Tong, Rafael R. Gattass, Jonathan B. Ashcom, Sailing He, Jingyi Lou, Mengyan Shen, Iva Maxwell, and Eric Mazur. Subwavelength-diameter silica wires for low-loss optical wave guiding. *Nature*, 426(6968):816–819, December 2003.
 - [33] Limin Tong, Jingyi Lou, Zhizhen Ye, Geoff T Svacha, and Eric Mazur. Self-modulated taper drawing of silica nanowires. *Nanotechnology*, 16(9):1445–1448, September 2005.
 - [34] Limin Tong and Eric Mazur. Glass nanofibers for micro- and nano-scale photonic devices. *Journal of Non-Crystalline Solids*, 354(12):1240–1244, February 2008.

-
- [35] P J G Butler. Self-assembly of tobacco mosaic virus: the role of an intermediate aggregate in generating both specificity and speed. *Philosophical Transactions of the Royal Society of London B*, 354:537–550, 1999.
 - [36] William (B.R.) Brinkley. Microtubules: A Brief Historical Perspective. *Journal of Structural Biology*, 118(2):84–86, March 1997.
 - [37] M. Kikkawa. Direct visualization of the microtubule lattice seam both in vitro and in vivo. *The Journal of Cell Biology*, 127(6):1965–1971, December 1994.
 - [38] Cheng Zeng, Guillermo Rodriguez Lázaro, Irina B. Tsvetkova, Michael F. Hagan, and Bogdan Dragnea. Defects and Chirality in the Nanoparticle-Directed Assembly of Spherocylindrical Shells of Virus Coat Proteins. *ACS Nano*, 12(6):5323–5332, June 2018.
 - [39] Céline Valéry, Franck Artzner, and Maité Paternostre. Peptide nanotubes: molecular organisations, self-assembly mechanisms and applications. *Soft Matter*, 7(20):9583–9594, October 2011.
 - [40] Mildred Quintana, Marek Grzelczak, Konstantinos Spyrou, Matteo Calvaresi, Sara Bals, Bart Kooi, Gustaaf Van Tendeloo, Petra Rudolf, Francesco Zerbetto, and Maurizio Prato. A Simple Road for the Transformation of Few-Layer Graphene into MWNTs. *Journal of the American Chemical Society*, 134(32):13310–13315, August 2012.
 - [41] Uwe B. Sleytr, Paul Messner, Dietmar Pum, and Margit Sára. Crystalline Bacterial Cell Surface Layers (S Layers): From Supramolecular Cell Structure to Biomimetics and Nanotechnology. *Angewandte Chemie International Edition*, 38(8):1034–1054, 1999.
 - [42] Anton Kuzyk, Yangyang Yang, Xiaoyang Duan, Simon Stoll, Alexander O. Govorov, Hiroshi Sugiyama, Masayuki Endo, and Na Liu. A light-driven three-dimensional plasmonic nanosystem that translates molecular motion into reversible chiroptical function. *Nature Communications*, 7:10591, February 2016.
 - [43] Yingyue Zhu, Liguang Xu, Wei Ma, Zhou Xu, Hua Kuang, Libing Wang, and Chuanlai Xu. A one-step homogeneous plasmonic circular dichroism detection of aqueous mercury ions using nucleic acid functionalized gold nanorods. *Chemical Communications*, 48(97):11889–11891, November 2012.
 - [44] E. Hendry, T. Carpy, J. Johnston, M. Popland, R. V. Mikhaylovskiy, A. J. Lapthorn, S. M. Kelly, L. D. Barron, N. Gadegaard, and M. Kadodwala. Ultra-sensitive detection and characterization of biomolecules using superchiral fields. *Nature Nanotechnology*, 5(11):783–787, November 2010.

-
- [45] Yang Zhao, Amir N. Askarpour, Liuyang Sun, Jinwei Shi, Xiaoqin Li, and Andrea Alù. Chirality detection of enantiomers using twisted optical metamaterials. *Nature Communications*, 8:14180, January 2017.
 - [46] Jiawei Lv, Defang Ding, Xuekang Yang, Ke Hou, Xiang Miao, Dawei Wang, Baichuan Kou, Ling Huang, and Zhiyong Tang. Biomimetic chiral photonic crystals. *Angewandte Chemie International Edition*, 58(23):7783–7787.
 - [47] Tetsuo Kan, Akihiro Isozaki, Natsuki Kanda, Natsuki Nemoto, Kuniaki Konishi, Hidetoshi Takahashi, Makoto Kuwata-Gonokami, Kiyoshi Matsumoto, and Isao Shimoyama. Enantiomeric switching of chiral metamaterial for terahertz polarization modulation employing vertically deformable MEMS spirals. *Nature Communications*, 6:8422, October 2015.
 - [48] J. K. Gansel, M. Thiel, M. S. Rill, M. Decker, K. Bade, V. Saile, G. von Freymann, S. Linden, and M. Wegener. Gold Helix Photonic Metamaterial as Broadband Circular Polarizer. *Science*, 325(5947):1513–1515, September 2009.
 - [49] Y. Zhao, M. A. Belkin, and A. Alù. Twisted optical metamaterials for planarized ultrathin broadband circular polarizers. *Nature Communications*, 3:870, May 2012.
 - [50] Ion Bitai and Edwin L. Thomas. Structurally chiral photonic crystals with magneto-optic activity: indirect photonic bandgaps, negative refraction, and superprism effects. *Journal of the Optical Society of America B*, 22(6):1199–1210, June 2005.
 - [51] Tobias Frenzel, Muamer Kadic, and Martin Wegener. Three-dimensional mechanical metamaterials with a twist. *Science*, 358(6366):1072–1074, November 2017.
 - [52] A. D. Dinsmore and A. G. Yodanis. Entropic Confinement of Colloidal Spheres in Corners on Silicon Substrates. *Langmuir*, 15(2):314–316, January 1999.
 - [53] V. Randle. Grain boundary engineering: an overview after 25 years. *Materials Science and Technology*, 26(3):253–261, March 2010.
 - [54] Shreyas Gokhale, K. Hima Nagamanasa, Rajesh Ganapathy, and A. K. Sood. Grain growth and grain boundary dynamics in colloidal polycrystals. *Soft Matter*, 9(29):6634–6644, July 2013.
 - [55] Thomas O. E. Skinner, Dirk G. A. L. Aarts, and Roel P. A. Dullens. Grain-Boundary Fluctuations in Two-Dimensional Colloidal Crystals. *Physical Review Letters*, 105(16):168301, October 2010.

-
- [56] François A. Lavergne, Samuel Diana, Dirk G. A. L. Aarts, and Roel P. A. Dullens. Equilibrium Grain Boundary Segregation and Clustering of Impurities in Colloidal Polycrystalline Monolayers. *Langmuir*, 32(48):12716–12724, December 2016.
 - [57] Volkert W. A. de Villeneuve, Roel P. A. Dullens, Dirk G. A. L. Aarts, Esther Groeneveld, Johannes H. Scherff, Willem K. Kegel, and Henk N. W. Lekkerkerker. Colloidal Hard-Sphere Crystal Growth Frustrated by Large Spherical Impurities. *Science*, 309(5738):1231–1233, August 2005.
 - [58] Caitlin E. Cash, Jeremy Wang, Maya M. Martirosyan, B. Kemper Ludlow, Alejandro E. Baptista, Nina M. Brown, Eli J. Weissler, Jatin Abacousnac, and Sharon J. Gerbode. Local Melting Attracts Grain Boundaries in Colloidal Polycrystals. *Physical Review Letters*, 120(1):018002, January 2018.
 - [59] A. Thorvaldsen. The intercept method—1. Evaluation of grain shape. *Acta Materialia*, 45(2):587–594, February 1997.
 - [60] K. F. Kelton. Crystal nucleation in liquids and glasses. In *Solid state physics*, volume 45, pages 75–177. 1991.
 - [61] W. Ostwald. Studien uber die Bildung und Umwandlung fester Korper. *Zeitschrift für Physikalische Chemie*, 22:289–330, 1897.
 - [62] Tara D. Edwards, Yuguang Yang, Daniel J. Beltran-Villegas, and Michael A. Bevan. Colloidal crystal grain boundary formation and motion. *Scientific Reports*, 4(1):1–8, August 2014.
 - [63] Agustín E. González. Colloidal Crystallization in 2d for Short-Ranged Attractions: A Descriptive Overview. *Crystals*, 6(4):46, April 2016.
 - [64] J. W. Evans. Random and cooperative sequential adsorption. *Reviews of Modern Physics*, 65(4):1281–1329, October 1993.
 - [65] Jian-Sheng Wang and Ras B. Pandey. Kinetics and Jamming Coverage in a Random Sequential Adsorption of Polymer Chains. *Physical Review Letters*, 77(9):1773–1776, August 1996.
 - [66] Brendan Osberg, Johannes Nuebler, and Ulrich Gerland. Adsorption-Desorption Kinetics of Soft Particles. *Physical Review Letters*, 115(8):088301, August 2015.
 - [67] Pradip B. Shelke, S. B. Ogale, M. D. Khandkar, and A. V. Limaye. Peculiarities of the adsorption kinetics of mixed convex plus concave contour objects. *Physical Review E*, 77(6):066111, June 2008.

-
- [68] Masaharu Tanemura and Masami Hasegawa. Geometrical models of territory I. Models for synchronous and asynchronous settlement of territories. *Journal of Theoretical Biology*, 82(3):477–496, February 1980.
 - [69] Aidan P Thompson and Eduardo D Glandt. Random sequential adsorption in porous solids. *Journal of Colloid and Interface Science*, 146(1):63–68, October 1991.
 - [70] J. Talbot, G. Tarjus, P. R. Van Tassel, and P. Viot. From car parking to protein adsorption: an overview of sequential adsorption processes. *Colloids and Surfaces A: Physicochemical and Engineering Aspects*, 165(1):287–324, May 2000.
 - [71] L. A. Rosen, N. A. Seaton, and E. D. Glandt. Random sequential adsorption onto the surface of small spheres. *The Journal of Chemical Physics*, 85(12):7359–7363, December 1986.
 - [72] Robert H. Swendsen. Dynamics of random sequential adsorption. *Physical Review A*, 24(1):504–508, July 1981.
 - [73] M. C. Bartelt and V. Privman. Kinetics of irreversible multilayer adsorption: One-dimensional models. *The Journal of Chemical Physics*, 93(9):6820–6823, November 1990.
 - [74] A Renyi. On a one-dimensional problem concerning random space filling. *Selected Translations in Mathematical Statistics and Probability*, 4:203–218, 1963.
 - [75] V. Privman, J.-S. Wang, and P. Nielaba. Continuum limit in random sequential adsorption. *Physical Review B*, 43(4):3366–3372, February 1991.
 - [76] Michał Cieřła and Jakub Barbasz. Kinetics of random sequential adsorption of nearly spherically symmetric particles. *Physical Review E*, 89(2):022401, February 2014.
 - [77] G. Tarjus and P. Viot. Asymptotic results for the random sequential addition of unoriented objects. *Physical Review Letters*, 67(14):1875–1878, September 1991.
 - [78] P. Viot, G. Tarjus, S. M. Ricci, and J. Talbot. Random sequential adsorption of anisotropic particles. I. Jamming limit and asymptotic behavior. *The Journal of Chemical Physics*, 97(7):5212–5218, October 1992.
 - [79] Jeffrey L. Becklehimer and Ras B. Pandey. Percolation of chains and jamming coverage in two dimensions by computer simulation. *Journal of Statistical Physics*, 75(3):765–771, May 1994.

-
- [80] Y. Fan and J. K. Percus. Random sequential adsorption on a ladder. *Journal of Statistical Physics*, 66(1):263–271, January 1992.
 - [81] J. W. Evans and R. S. Nord. Random and cooperative sequential adsorption on infinite ladders and strips. *Journal of Statistical Physics*, 69(1):151–162, October 1992.
 - [82] Benjamin J. Brosilow, Robert M. Ziff, and R. Dennis Vigil. Random sequential adsorption of parallel squares. *Physical Review A*, 43(2):631–638, January 1991.
 - [83] Michał Cieřła and Jakub Barbasz. Random packing of regular polygons and star polygons on a flat two-dimensional surface. *Physical Review E*, 90(2):022402, August 2014.
 - [84] Soong-Hyuck Suh, Byung-Doo Jung, Yong-Jin Park, Viorel Chihaiia, Viorica Parvulescu, and Mariuca Gartner. Simulation Studies for Random Sequential Adsorption in Narrow Slit: Two-Dimensional Parking Model. *Bulletin of the Korean Chemical Society*, 29(4):873–875, 2008.
 - [85] Michal Ciesla and Jakub Barbasz. Random sequential adsorption on fractals. *The Journal of Chemical Physics*, 137(4):044706, July 2012.
 - [86] Panu Danwanichakul and Tawatchai Charinpanitkul. Random sequential adsorption of polydisperse spherical particles: An integral-equation theory. *Physica A: Statistical Mechanics and its Applications*, 377(1):102–114, April 2007.
 - [87] Angus C. Cameron and Richard P. Widmer. *Handbook of Pediatric Dentistry*. Elsevier, 4th edition, 2013.
 - [88] A. Mughal and D. Weaire. Phyllotaxis, disk packing, and Fibonacci numbers. *Physical Review E*, 95(2):022401, February 2017.
 - [89] Marc L. Mansfield, Leela Rakesh, and Donald A. Tomalia. The random parking of spheres on spheres. *Journal of Chemical Physics*, 105:3245, August 1996.
 - [90] Jens Feder and Ivar Giaever. Adsorption of ferritin. *Journal of Colloid and Interface Science*, 78(1):144–154, November 1980.
 - [91] Marta Sadowska, Zbigniew Adamczyk, Magdalena Oćwieja, and Małgorzata Nattich-Rak. Monolayers of silver nanoparticles on positively charged polymer microspheres. *Colloids and Surfaces A: Physicochemical and Engineering Aspects*, 499:1–9, June 2016.
 - [92] Elizabeth R. Chen and Miranda Holmes-Cerfon. Random Sequential Adsorption of Discs on Surfaces of Constant Curvature: Plane, Sphere, Hyperboloid, and Projective Plane. *Journal of Nonlinear Science*, 27(6):1743–1787, December 2017.

-
- [93] Marta Sadowska, Zbigniew Adamczyk, and Małgorzata Nattich-Rak. Mechanism of Nanoparticle Deposition on Polystyrene Latex Particles. *Langmuir*, 30(3):692–699, January 2014.
 - [94] Ho-Kei Chan. Densest columnar structures of hard spheres from sequential deposition. *Physical Review E*, 84(5):050302, November 2011.
 - [95] Einar L. Hinrichsen, Jens Feder, and Torstein Jøssang. Geometry of random sequential adsorption. *Journal of Statistical Physics*, 44(5):793–827, September 1986.
 - [96] Adrian Baule. Shape Universality Classes in the Random Sequential Adsorption of Nonspherical Particles. *Physical Review Letters*, 119(2):028003, July 2017.
 - [97] Lin Fu, William Steinhardt, Hao Zhao, Joshua E. S. Socolar, and Patrick Charbonneau. Hard sphere packings within cylinders. *Soft Matter*, 12(9):2505–2514, February 2016.
 - [98] R. Dennis Vigil and Robert M. Ziff. Kinetics of random sequential adsorption of rectangles and line segments. *The Journal of Chemical Physics*, 93(11):8270–8272, December 1990.
 - [99] Lin Fu, Ce Bian, C. Wyatt Shields, Daniela F. Cruz, Gabriel P. López, and Patrick Charbonneau. Assembly of hard spheres in a cylinder: a computational and experimental study. *Soft Matter*, 13(18):3296–3306, May 2017.
 - [100] Stanley D. Chandradoss, Anna C. Haagsma, Young Kwang Lee, Jae-Ho Hwang, Jwa-Min Nam, and Chirlmin Joo. Surface Passivation for Single-molecule Protein Studies. *Journal of Visualized Experiments*, (86):50549, April 2014.
 - [101] Joon Suk Oh, Yufeng Wang, David J. Pine, and Gi-Ra Yi. High-Density PEO-*b*-DNA Brushes on Polymer Particles for Colloidal Superstructures. *Chemistry of Materials*, 27(24):8337–8344, December 2015.
 - [102] Costas M. Soukoulis and Martin Wegener. Past achievements and future challenges in the development of three-dimensional photonic metamaterials. *Nature Photonics*, 5(9):523–530, September 2011.
 - [103] Vladimir M. Shalaev, Wenshan Cai, Uday K. Chettiar, Hsiao-Kuan Yuan, Andrey K. Sarychev, Vladimir P. Drachev, and Alexander V. Kildishev. Negative index of refraction in optical metamaterials. *Optics Letters*, 30(24):3356–3358, December 2005.
 - [104] Na Liu, Hongcang Guo, Liwei Fu, Stefan Kaiser, Heinz Schweizer, and Harald Giessen. Three-dimensional photonic metamaterials at optical frequencies. *Nature Materials*, 7(1):31–37, January 2008.

-
- [105] M. Decker, R. Zhao, C. M. Soukoulis, S. Linden, and M. Wegener. Twisted split-ring-resonator photonic metamaterial with huge optical activity. *Optics Letters*, 35(10):1593–1595, May 2010.
 - [106] Jason Valentine, Shuang Zhang, Thomas Zentgraf, Erick Ulin-Avila, Dentcho A. Genov, Guy Bartal, and Xiang Zhang. Three-dimensional optical metamaterial with a negative refractive index. *Nature*, 455(7211):376–379, September 2008.
 - [107] Michael S. Rill, Christine Plet, Michael Thiel, Isabelle Staude, Georg von Freymann, Stefan Linden, and Martin Wegener. Photonic metamaterials by direct laser writing and silver chemical vapour deposition. *Nature Materials*, 7(7):543–546, July 2008.
 - [108] D. Bruce Burckel, Joel R. Wendt, Gregory A. Ten Eyck, James C. Ginn, A. Robert Ellis, Igal Brener, and Michael B. Sinclair. Micrometer-Scale Cubic Unit Cell 3d Metamaterial Layers. *Advanced Materials*, 22(44):5053–5057, 2010.
 - [109] Eva-Maria Roller, Larousse Khosravi Khorashad, Michael Fedoruk, Robert Schreiber, Alexander O. Govorov, and Tim Liedl. DNA-Assembled Nanoparticle Rings Exhibit Electric and Magnetic Resonances at Visible Frequencies. *Nano Letters*, 15(2):1368–1373, February 2015.
 - [110] Jaewon Lee, Ji-Hyeok Huh, Kwangjin Kim, and Seungwoo Lee. DNA Origami-Guided Assembly of the Roundest 60-100 nm Gold Nanospheres into Plasmonic Metamolecules. *Advanced Functional Materials*, 28(15):1707309, April 2018.
 - [111] Jonathan A. Fan, Chihhui Wu, Kui Bao, Jiming Bao, Rizia Bardhan, Naomi J. Halas, Vinothan N. Manoharan, Peter Nordlander, Gennady Shvets, and Federico Capasso. Self-Assembled Plasmonic Nanoparticle Clusters. *Science*, 328(5982):1135–1138, May 2010.
 - [112] Jonathan A. Fan, Kui Bao, Li Sun, Jiming Bao, Vinothan N. Manoharan, Peter Nordlander, and Federico Capasso. Plasmonic Mode Engineering with Templated Self-Assembled Nanoclusters. *Nano Letters*, 12(10):5318–5324, October 2012.
 - [113] Yaroslav A. Urzhumov, Gennady Shvets, Jonathan Fan, Federico Capasso, Daniel Brandl, and Peter Nordlander. Plasmonic nanoclusters: a path towards negative-index metafluids. *Optics Express*, 15(21):14129–14145, October 2007.
 - [114] Kwangjin Kim, SeokJae Yoo, Ji-Hyeok Huh, Q-Han Park, and Seungwoo Lee. Limitations and Opportunities for Optical Metafluids To Achieve an Unnatural Refractive Index. *ACS Photonics*, 4(9):2298–2311, September 2017.
 - [115] Anthony Désert, Céline Hubert, Zheng Fu, Lucie Moulet, Jérôme Majimel, Philippe Barboteau, Antoine Thill, Muriel Lansalot, Elodie Bourgeat-Lami,

-
- Etienne Duguet, and Serge Ravaine. Synthesis and Site-Specific Functionalization of Tetravalent, Hexavalent, and Dodecavalent Silica Particles. *Angewandte Chemie International Edition*, 52(42):11068–11072, 2013.
- [116] Céline Hubert, Cyril Chomette, Anthony Désert, Ming Sun, Mona Treguer-Delapierre, Stéphane Mornet, Adeline Perro, Etienne Duguet, and Serge Ravaine. Synthesis of multivalent silica nanoparticles combining both enthalpic and entropic patchiness. *Faraday Discussions*, 181(0):139–146, July 2015.
- [117] Anthony Désert, Isabelle Chaduc, Sarah Fouilloux, Jean-Christophe Taveau, Olivier Lambert, Muriel Lansalot, Elodie Bourgeat-Lami, Antoine Thill, Olivier Spalla, Serge Ravaine, and Etienne Duguet. High-yield preparation of polystyrene/silica clusters of controlled morphology. *Polymer Chemistry*, 3(5):1130–1132, April 2012.
- [118] Adeline Perro, Etienne Duguet, Olivier Lambert, Jean-Christophe Taveau, Elodie Bourgeat-Lami, and Serge Ravaine. A Chemical Synthetic Route towards “Colloidal Molecules”. *Angewandte Chemie International Edition*, 48(2):361–365, 2009.
- [119] Anthony Désert, Jérémy Morele, Jean-Christophe Taveau, Olivier Lambert, Muriel Lansalot, Elodie Bourgeat-Lami, Antoine Thill, Olivier Spalla, Luc Belloni, Serge Ravaine, and Etienne Duguet. Multipod-like silica/polystyrene clusters. *Nanoscale*, 8(10):5454–5469, March 2016.
- [120] Cyril Chomette, Mona Tréguer-Delapierre, Nicholas B. Schade, Vinodhan N. Manoharan, Olivier Lambert, Jean-Christophe Taveau, Serge Ravaine, and Etienne Duguet. Colloidal Alchemy: Conversion of Polystyrene Nanoclusters into Gold. *ChemNanoMat*, 3(3):160–163, 2017.
- [121] You-Jin Lee, Nicholas B. Schade, Li Sun, Jonathan A. Fan, Doo Ri Bae, Marcelo M. Mariscal, Gaehang Lee, Federico Capasso, Stefano Sacanna, Vinodhan N. Manoharan, and Gi-Ra Yi. Ultrasoft, Highly Spherical Monocrystalline Gold Particles for Precision Plasmonics. *ACS Nano*, 7(12):11064–11070, December 2013.
- [122] Pierre-Etienne Rouet, Cyril Chomette, Etienne Duguet, and Serge Ravaine. Colloidal Molecules from Valence-Endowed Nanoparticles by Covalent Chemistry. *Angewandte Chemie International Edition*, 57(48):15754–15757, 2018.
- [123] S. J Oldenburg, R. D Averitt, S. L Westcott, and N. J Halas. Nanoengineering of optical resonances. *Chemical Physics Letters*, 288(2):243–247, May 1998.
- [124] Kurtis D. Hartlen, Aristidis P. T. Athanasopoulos, and Vladimir Kitaev. Facile Preparation of Highly Monodisperse Small Silica Spheres (15 to >200 nm)

-
- Suitable for Colloidal Templating and Formation of Ordered Arrays. *Langmuir*, 24(5):1714–1720, March 2008.
- [125] Prashant K. Jain and Mostafa A. El-Sayed. Surface Plasmon Resonance Sensitivity of Metal Nanostructures: Physical Basis and Universal Scaling in Metal Nanoshells. *The Journal of Physical Chemistry C*, 111(47):17451–17454, November 2007.
 - [126] Alexander S. Urban, Xiaoshuang Shen, Yumin Wang, Nicolas Large, Hong Wang, Mark W. Knight, Peter Nordlander, Hongyu Chen, and Naomi J. Halas. Three-Dimensional Plasmonic Nanoclusters. *Nano Letters*, 13(9):4399–4403, September 2013.
 - [127] Kyung Jin Park, Ji-Hyeok Huh, Dae-Woong Jung, Jin-Sung Park, Gwan H. Choi, Gaehang Lee, Pil J. Yoo, Hong-Gyu Park, Gi-Ra Yi, and Seungwoo Lee. Assembly of “3d” plasmonic clusters by “2d” AFM nanomanipulation of highly uniform and smooth gold nanospheres. *Scientific Reports*, 7(1):1–10, July 2017.
 - [128] Sassan N. Sheikholeslami, Hadiseh Alaeian, Ai Leen Koh, and Jennifer A. Dionne. A Metafluid Exhibiting Strong Optical Magnetism. *Nano Letters*, 13(9):4137–4141, September 2013.
 - [129] Zhaoxia Qian, Simon P. Hastings, Chen Li, Brian Edward, Christine K McGinn, Nader Engheta, Zahra Fakhraai, and So-Jung Park. Raspberry-like Metamolecules Exhibiting Strong Magnetic Resonances. *ACS Nano*, 9(2):1263–1270, February 2015.
 - [130] Véronique Many, Romain D  zert, Etienne Duguet, Alexandre Baron, Vikas Jangid, Virginie Ponsinet, Serge Ravaine, Philippe Richetti, Philippe Barois, and Mona Tr  guer-Delapierre. High optical magnetism of dodecahedral plasmonic meta-atoms. *Nanophotonics*, 8(4):549–558, March 2019.
 - [131] Antoine Thill, Anthony D  sert, Sarah Fouilloux, Jean-Christophe Taveau, Olivier Lambert, Muriel Lansalot, Elodie Bourgeat-Lami, Olivier Spalla, Luc Belloni, Serge Ravaine, and Etienne Duguet. Spheres Growing on a Sphere: A Model to Predict the Morphology Yields of Colloidal Molecules Obtained through a Heterogeneous Nucleation Route. *Langmuir*, 28(31):11575–11583, August 2012.
 - [132] Zhe Gong, Theodore Hueckel, Gi-Ra Yi, and Stefano Sacanna. Patchy particles made by colloidal fusion. *Nature*, 550(7675):234–238, October 2017.
 - [133] Nora Reinhardt, Laurent Adumeau, Olivier Lambert, Serge Ravaine, and St  phane Mornet. Quaternary Ammonium Groups Exposed at the Surface of Silica Nanoparticles Suitable for DNA Complexation in the Presence of

-
- Cationic Lipids. *The Journal of Physical Chemistry B*, 119(21):6401–6411, May 2015.
- [134] Daniel G. Duff, Alfons Baiker, and Peter P. Edwards. A new hydrosol of gold clusters. 1. Formation and particle size variation. *Langmuir*, 9(9):2301–2309, September 1993.
- [135] Ichiro Sunagawa. Growth and Morphology of Crystals. *Forma*, 14:147–166, 1999.
- [136] J. R. Savage, D. W. Blair, A. J. Levine, R. A. Guyer, and A. D. Dinsmore. Imaging the Sublimation Dynamics of Colloidal Crystallites. *Science*, 314(5800):795–798, November 2006.
- [137] A. M. Alsayed, M. F. Islam, J. Zhang, P. J. Collings, and A. G. Yodh. Premelting at Defects Within Bulk Colloidal Crystals. *Science*, 309(5738):1207–1210, August 2005.
- [138] Daniel A. Beller and David R. Nelson. Plastic deformation of tubular crystals by dislocation glide. *Physical Review E*, 94(3), September 2016.
- [139] Anton Kuzyk, Robert Schreiber, Zhiyuan Fan, Günther Pardatscher, Eva-Maria Roller, Alexander Högele, Friedrich C. Simmel, Alexander O. Govorov, and Tim Liedl. DNA-based self-assembly of chiral plasmonic nanostructures with tailored optical response. *Nature*, 483(7389):311–314, March 2012.